Department of Physics and Astronomy
University of Heidelberg

Bachelor Thesis in Physics
submitted by

Jan Jakob

born in Stuttgart (Germany)

2022

A new inversion algorithm for weak lensing using quasi-conformal geometry

This Bachelor Thesis has been carried out by
Jan Jakob
at the
Institut für Theoretische Astrophysik in Heidelberg
under the supervision of
Prof. Dr. Björn Malte Schäfer
with second assessor
Prof. Dr. Matthias Bartelmann

Abstract

One of the challenges in weak gravitational lensing by galaxies and clusters is to infer the projected mass density distribution from the observable image ellipticities, which is known as inversion problem. In this thesis we derive a new inversion algorithm for weak gravitational lensing to reconstruct the deflection field out of the reduced shear, which is in principle observable from the image ellipticities. We propose both an algorithm for the planar case, i.e. for fields for which the flat sky approximation can be assumed, and an algorithm for the general (curved) case, i.e. for fields, where the curvature cannot be neglected and the flat-sky approximation loses its validity. Using a complex formalism we show that for the planar case the lens mapping is a quasi-conformal mapping with Beltrami coefficient given by the negative of the reduced shear. Our proposed algorithm then computes this quasi-conformal mapping with a finite element approach via a reduction to two elliptic PDEs. By introducing notions from quasi-conformal geometry like the Beltrami differential we generalize our inversion algorithm to curved fields by trying to describe the lens mapping as quasi-conformal mapping between appropriate Riemann surfaces. The lens mapping can then be computed with methods from computational quasi-conformal geometry. To the best of our knowledge, this is the first work which combines methods from quasi-conformal geometry with weak lensing in order to construct new inversion algorithms. We implemented and tested our proposed algorithm for planar fields with different source and lens configurations and compared it to the well-known KS 93 algorithm and its extension to the non-linear regime. However, the implementation of the algorithm for curved fields could not be done and will be the subject of further work.

Zusammenfassung

Eine der Herausforderungen beim schwachen Gravitationslinseneffekt durch Galaxien und Galaxienhaufen besteht darin, die projizierte Massendichteverteilung aus den beobachtbaren Bildelliptizitäten abzuleiten, was als Inversionsproblem bekannt ist. In dieser Arbeit leiten wir einen neuen Inversionsalgorithmus für den schwachen Gravitationslinseneffekt her, um das Ablenkwinkelfeld aus der reduzierten Scherung zu rekonstruieren, die man aus den Bildelliptizitäten erhält. Wir schlagen sowohl einen Algorithmus für den ebenen Fall vor, d.h. für Felder, für die die flache Himmelsapproximation angenommen werden kann, als auch einen Algorithmus für den allgemeinen (gekrümmten) Fall, d.h. für Felder, bei denen die Krümmung nicht vernachlässigt werden kann und die flache Himmelsapproximation ihre Gültigkeit verliert. Mit Hilfe eines komplexen Formalismus zeigen wir, dass die Linsengleichung im ebenen Fall eine quasi-konforme Abbildung ist, deren Beltrami-Koeffizient der negativen reduzierten Scherung entspricht. Der von uns vorgeschlagene Algorithmus berechnet dann diese quasi-konforme Abbildung durch eine Reduktion auf elliptische PDEs mit einem Finite-Elemente-Ansatz. Durch die Einführung von Begriffen aus der quasi-konformen Geometrie wie dem Beltrami-Differential verallgemeinern wir den Inversionsalgorithmus auf den gekrümmten Fall, indem wir versuchen, die Linsengleichung als quasi-konforme Abbildung zwischen geeigneten Riemannschen Flächen zu beschreiben. Das Ablenkwinkelfeld kann dann mit Methoden der rechnergestützten quasi-konformen Geometrie berechnet werden. Soweit wir wissen, ist dies die erste Arbeit, die Methoden aus der quasi-konformen Geometrie mit dem schwachen Gravitationslinseneffekt kombiniert, um neue Inversionsalgorithmen zu konstruieren. Wir haben den von uns vorgeschlagenen Algorithmus für planare Felder implementiert, ihn mit verschiedenen Quellen- und Linsenkonfigurationen getestet und mit dem bekannten KS 93 Algorithmus und seiner Erweiterung für den nichtlinearen Bereich verglichen. Die Implementierung des Algorithmus für gekrümmte Felder konnte jedoch nicht durchgeführt werden und wird Gegenstand weiterer Arbeiten sein.

.

Contents

1 Introduction

Einstein's theory of relativity predicts that matter (energy density) bends space time. Since light rays follow zero geodesics in space-time, any electromagnetic radiation sent out by a source is deflected. This process is known as gravitational lensing, and many important results for cosmology have come from exploiting this effect. In many cases gravitational lensing can be described analogously to the deflection of light by optical lenses. Thus, one speaks of sources, lenses, and images in analogy to ray optics. Gravitational lensing can be divided into three regimes: strong lensing, weak lensing and microlensing. The distinction between these regimes depends on the positions of the source, the lens and the observer as well as on the mass and the mass distribution of the lens. In this work we will deal with weak lensing.

1.1 Basics of Weak Lensing

In the case of weak lensing, light rays are only weakly deflected. Each point in the image plane corresponds to exactly one point in the source plane. There are no multiple images. Nevertheless, the source can be distorted: It can be both stretched (shear) and magnified (convergence). If the size and shape of all sources are known, one can use shear and convergence to infer the properties of the lens. However, one usually does not know these intrinsic properties, but has information about the average properties of the source. These statistics can then be used to obtain information about the lens. Weak lensing can thus be viewed as a statistical measurement that allows one to measure the mass distribution of the lens without making assumptions about its composition or dynamical state. That is the reason why weak lensing has become extremly important recently, in order to make statements about the distribution of dark matter in the universe. Following Umetsu [2020] and Meneghetti [2021] we give a short introduction into the basic concepts of weak lensing.

1.1.1 Lens Equation

We consider the following situation illustrated in figure 1.
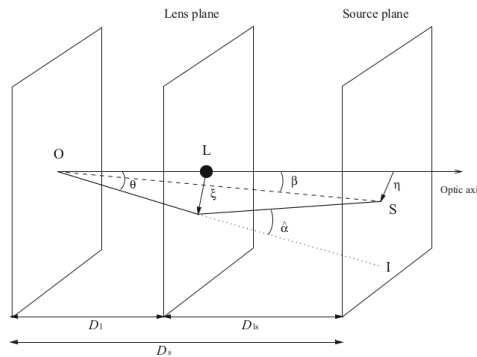
Figure 1: Illustration of a typical lens system, figure from Umetsu [2020]

A far-distant source (S) is located at the position η in the source plane. It sends out a light ray, which propagates to an observer (O). On its way to (O) it passes the position ξ in the lens plane (L), in which the light is deflected by a beding angle $\hat{\alpha}$. The source and lens planes are defined as planes perpendicular to the optical axis at the distance of the source and the lens, respectively. With D_L, D_S and D_{LS} we denote the angular diameter distances between (O) and (L), (O) and (S), and (L) and (S), respectively. Furthermore, β denotes the angle between the optical axis and the unlensed source (S), and θ the angle between optical axis and image (I). With that we can derive the following geometrical relation from figure 1:

$$\eta = \frac{D_S}{D_L}\xi + D_{LS}\,\hat{\alpha}(\xi). \tag{1.1.1}$$

Using $\beta = \eta/D_S$ and $\theta = \xi/D_L$ we can translate this equation into

$$\beta = \theta + \frac{D_{LS}}{D_S}\hat{\alpha} = \theta + \alpha(\theta), \tag{1.1.2}$$

with the *reduced bending angle*, or *deflection field*

$$\alpha(\theta) = (D_{LS}/D_S)\hat{\alpha}. \tag{1.1.3}$$

Equation 1.1.2 is referred to as the *lens equation*, or the *ray-tracing equation*.

1.1.2   Deflection Field and Lensing Potential

The lensing equation 1.1.2 describes a simple relation between the true position β of an object and the apparent position θ as perceived by an observer due to lensing. Knowledge of the deflection angle α is therefore sufficient to determine the true position of an object. The exact expression for α depends on the physical framework in which the lensing is considered. For instance, in a Schwartzschild metric for the Newtonian limit case, the deflection field is given by the gravitational potential Φ:

$$\alpha = \nabla_\theta \frac{2}{c^2} \int_{-\infty}^{\infty} \frac{D_L D_{LS}}{D_S} \Phi(D_L\theta, z)\mathrm{d}z = \nabla_\theta \Psi. \tag{1.1.4}$$

Ψ denotes the *lensing potential* given by

$$\Psi = \frac{2}{c^2} \int_{-\infty}^{\infty} \frac{D_L D_{LS}}{D_S} \Phi(D_L\theta, z)\mathrm{d}z. \tag{1.1.5}$$

The deflection field can therefore be expressed as gradient of a potential in the direction of the vector θ. It is also possible to derive the cosmological versions of equations 1.1.4 and 1.1.5, e.g. for lensing by large scale structures.

1.1.3   Convergence and Shear

We introduce local Cartesian coordinates $\theta = (\theta_1, \theta_2)$ centered on a certain reference point in the image plane. The Jacobian matrix of the lens mapping,

$$\mathcal{A}(\theta) := \frac{\partial\beta}{\partial\theta} = \begin{pmatrix} 1 - \Psi_{11} & -\Psi_{12} \\ -\Psi_{12} & 1 - \Psi_{22} \end{pmatrix} \tag{1.1.6}$$

describes the local properties of lensing. We have used the notation $\Psi_{i,j} := \partial^2\Psi/\partial\theta_i\partial\theta_j$ $(i, j = 1, 2)$. Alternatively, the components of the Jacobian matrix can be written as $\mathcal{A}_{ij} = \delta_{ij} - \Psi_{ij}$, where δ_{ij} denotes the Kronecker delta in two dimensions. It is convenient to decompose $\mathcal{A}$ by means of the Pauli matrices σ_a $(a = 1, 2, 3)$ as

$$\mathcal{A} = (1 - \kappa)\mathcal{I} - \gamma_1\sigma_3 - \gamma_2\sigma_1. \tag{1.1.7}$$

κ is called *convergence* and defined as one half of the Laplacian of Ψ:

$$\kappa := \frac{1}{2}(\Psi_{11} + \Psi_{22}) = \frac{1}{2}\Delta\Psi, \tag{1.1.8}$$

with $\Delta = \nabla_\theta^2$. γ_1 and γ_2 are the two components of the *shear γ*, which can be considered as a complex quantity $\gamma(\theta) := \gamma_1(\theta) + \mathrm{i}\gamma_2(\theta)$. Like κ, γ_1 and γ_2 are linear combinations of the second order derivatives of Ψ:

$$\gamma_1 := \frac{1}{2}(\Psi_{11} - \Psi_{22}), \tag{1.1.9}$$

$$\gamma_2 := \frac{1}{2}(\Psi_{12} + \Psi_{21}) = \Psi_{12}. \tag{1.1.10}$$

2

Equation 1.1.8 can be regared as a two-dimensional Poisson equation,

$$\Delta\Psi(\theta) = 2\kappa(\theta) \tag{1.1.11}$$

with inhomogeneity equals 2κ. Often one assumes that the field size is (hypothetical) infinite, i.e. it is sufficiently larger than the characteristic angular scale of the lensing cluster, but small enough for the flat-sky assumption to be valid. Then, the Green function becomes $\Delta^{-1}(\theta, \theta') = \ln|\theta, \theta'|/(2\pi)$, which yields Ψ as convolution of Δ^{-1} with 2κ:

$$\Psi(\theta) = \frac{1}{\pi} \int \ln(\theta - \theta')\kappa(\theta')\mathrm{d}^2\theta'. \tag{1.1.12}$$

Using these new quantities, we can express $\mathcal{A}$ as:

$$\mathcal{A}(\theta) = \begin{pmatrix} 1 - \kappa - \gamma_1 & -\gamma_2 \\ -\gamma_2 & 1 - \kappa + \gamma_1 \end{pmatrix}. \tag{1.1.13}$$

This gives us the expression $\det(\mathcal{A}) = (1 - \kappa)^2 - |\gamma|^2$, which becomes important when defining the magnficiation in subsection 1.1.4. We want to understand the physical interpretation of κ and γ: With $\mathcal{A}^{-1}$ we can describe the deformation of an infinitesimal circular source ($\mathrm{d}\beta \to 0$). In the weak lensing limit ($|\kappa|, |\gamma| \ll 1$) we obtain

$$(\mathcal{A}^{-1})_{ij} \simeq (1 + \kappa)\delta_{ij} + \Gamma_{ij} \quad (i, j = 1, 2). \tag{1.1.14}$$

Γ_{ij} is the matrix defined by (Bartelmann and Schneider [2001], Crittenden et al. [2002]):

$$\Gamma_{ij} = \left(\partial_i\partial_j - \delta_{ij}\frac{1}{2}\Delta\right)\Psi(\theta) = (\sigma_3\gamma_1 + \sigma_1\gamma_2)_{ij}, \tag{1.1.15}$$

with $\partial_i := \partial/\partial\theta_i$. Equation 1.1.14 allows now an interpretation of convergence and shear: The first term describes the isotropic light focussing or area distortion in the weak lensing limit, while the second term induces an asymmetry in the lens mapping. The shear γ thus is responsible for the image distortions. In the weak lensing limit it is directly observable from the image ellipticities of background galaxies. The effects of κ and γ are illustrated in figure 2.
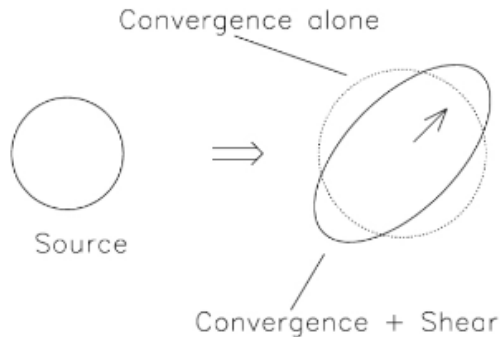
Figure 2: Illustration of the effects of κ and γ on the angular shape and size of a hypotetical circular source, figure from Meneghetti [2021]

1.1.4 Magnification

Gravitational lensing preserves the surface brightness of a background source, since photons are only deflected by gravitational lensing and are neither created nor destroyed by this effect. This is a consequence of Liouville's theorem. As the size of the source is not conserved, gravitational lensing either

magnifies or demagnifies the source. The magnification ν is given through the ratio between the lensed to the unlensed image solid angle as

$$\nu(\theta) = \frac{\delta\Omega^I}{\partial\Omega^S} = 1/\det(\mathcal{A}) = \frac{1}{[1 - \kappa(\theta)]^2 - |\gamma(\theta))|^2}. \tag{1.1.16}$$

We have used ν here for the magnifiaction instead of μ, which is common in the literature, because we will use μ later to denote a quantity called Beltrami-coefficient that is essential for quasi-conformal mappings. In the weak lensing limit ($|\kappa|, |\gamma| \ll 1$), $\det(\mathcal{A}) \simeq 1 - 2\kappa$ and ν can be approximated to the first order by

$$\nu(\theta) \simeq 1 + 2\kappa(\theta). \tag{1.1.17}$$

Thus, for an example value of $\kappa(\theta) = 0.1$ the magnitude change is $\Delta m = -(5/2)\log_{10}(\nu) \sim -0.2$.

1.1.5 Strong- and Weak Lensing Regimes

The matrix $\mathcal{A}(\theta)$ is symmetric. Thus, it can be diagonalized with eigenvalues $\Lambda_{\pm}(\theta)$ at each image position θ:

$$\Lambda_{\pm} = 1 - \kappa \pm |\gamma|. \tag{1.1.18}$$

Images with $\det\mathcal{A}(\theta) > 0$ have the same parity as the source, while those with $\det\mathcal{A}(\theta) < 0$ have the opposite parity of the source. A closed curve in the image plane defined by $\det\mathcal{A}(\theta) = 0$ is called *critical curve*, since on it the lensing magnification formally diverges. The preimage of a critical curve under the lens mapping is referred to as *caustic*. Thus, the image plane is seperated into even- and odd-parity regions by the critical curves.

The eigenvalues allow us to distinguish between strong and weak lensing regimes: As already seen above, the lens mapping transforms an infinitesimal circular source to an ellipse. For $\kappa < 1$ this ellipse has a minor-to-major axis ratio of $|\Lambda_-/\Lambda_+| \leq 1$ and of $|\Lambda_+/\Lambda_-| \geq 1$ for $\kappa > 1$. If a lens system has a region with $\kappa(\theta) > 1$, it is called *supercritical* and can produce multiple images for certain source positions β. However, being supercritical is a sufficient but not a necessary condition for a general lens to produce multiple images, because the shear can also contribute. Nevertheless, this provides us with a simple criterion to broadly distinguish the regimes of multiple and single imaging. Keeping this in mind, we refer to the region where $\kappa(\theta) \gtrsim 1$ as the strong-lensing regime and the region where $\kappa(\theta) \ll 1$ as the weak-lensing regime.

1.1.6 Mass-Sheet Degeneracy

The shear γ is in general not observable. Instead, we can observe a quantity called *reduced shear*:

$$g(\theta) := \frac{\gamma(\theta)}{1 - \kappa(\theta)} = \frac{\gamma_1(\theta)}{1 - \kappa(\theta)} + i\frac{\gamma_2(\theta)}{1 - \kappa(\theta)}. \tag{1.1.19}$$

For the subcritical regime where $\det\mathcal{A} > 0$ we can observe g directly, whereas for negative-parity regions with $\det\mathcal{A} < 0$ the quantity $1/g^*$ is observable. From the definition we see that g remains invariant under the transformation

$$\kappa(\theta) \rightarrow \lambda\kappa(\theta) + 1 - \lambda, \quad \gamma(\theta) \rightarrow \lambda\gamma(\theta). \tag{1.1.20}$$

Substantially, the mass-sheet degeneracy is based on the fact that the size and ellipticity of an image are independent of each other. Thus, the Jacobian matrix $\mathcal{A}$ can be multiplied by the factor λ ($\lambda \neq 0$) leaving the ellipticity invariant.

1.1.7 Breaking the mass-sheet degeneracy:

Simplified, the mass-sheet degeneracy results from having only measured the two quantities $g_1 := \text{Re}(g)$ and $g_2 := \text{Im}(g)$, but trying to infer three quantities κ, γ_1 and γ_2. Another independently measured quantity is therefore required. Often one chooses the magnification, since μ has a different behaviour under the transformation 1.1.20: It scales with λ^{-2}. This was first recognized by Broadhurst et al. [1995]. The magnification can be obtained by comparing the sizes of galaxies in cluster fields with those of galaxies of equal surface brightness in empty fields. Alternatively, ν can be obtained from the changes in the number density of galaxies.

1.2 Weak Lensing by Galaxies and Clusters

Weak gravitational lensing of background galaxies provides a direct probe of the projected matter distribution in and around galaxy clusters. Although it is an intrinsically statistical measurement, it provides a way to measure the distribution without requiring assumptions about the composition or dynamical state of the galaxies. Again we follow Umetsu [2020] and Meneghetti [2021] to introduce the most important concepts.

1.2.1 Basic Principle

The basic idea of weak lensing is to measure the ellipticities of the lensed images and to infer the mass distribution of the lenses. This is possible for two reasons: First, because the mass distribution can be related to the convergence κ and accordingly the shear γ to the ellipticities. And second, because both κ and γ are linear combinations of second derivatives of the lensing potential Ψ.

1.2.2 Ellipticity Measurements

By determining the surface brightness distribution of the image, the ellipticities of the images can be infered. If we consider an elliptical image, the first moment θ_0 of the surface brightness $I(\theta)$

$$\theta_0 = \frac{\int I(\theta)\theta \mathrm{d}^2\theta}{\int I(\theta)\mathrm{d}^2\theta} \tag{1.2.1}$$

defines the image centroid. By computing the second moments for $(i, j) \in \{1, 2\}$

$$Q_{ij} = \frac{\int I(\theta)(\theta_i - \theta_{0,i})(\theta_j - \theta_{0,j})\mathrm{d}^2\theta}{\int I(\theta)\mathrm{d}^2\theta}, \tag{1.2.2}$$

we obtain the 2×2 quadrupole tensor Q of the distribution $I(\theta)$. Since Q is a symmetric tensor, it can be diagonalized with eigenvectors λ_+ and λ_- given by

$$\lambda_+ = \frac{1}{2}\left(Q_{11} + Q_{22} + \sqrt{(Q_{11} - Q_{22})^2 + 4Q_{12}^2}\right), \tag{1.2.3}$$

$$\lambda_- = \frac{1}{2}\left(Q_{11} + Q_{22} - \sqrt{(Q_{11} - Q_{22})^2 + 4Q_{12}^2}\right). \tag{1.2.4}$$

These eigenvectors define the principle axes of $I(\theta)$ and the major and minor axes a and b of the ellipse, which describes the image, are just oriented as the principle axes of Q. In particular, it holds:

$$\lambda_+ = 1/a^2, \tag{1.2.5}$$

$$\lambda_- = 1/b^2. \tag{1.2.6}$$

This allows us to express the absolute value of the ellipticity

$$|\epsilon| = \frac{\sqrt{(Q_{11} - Q_{22})^2 + 4Q_{12}^2}}{Q_{11} + Q_{22} + 2\sqrt{Q_{11}Q_{22} - Q_{12}}}, \tag{1.2.7}$$

and the components of the ellipticity

$$\epsilon_1 = \frac{Q_{11} - Q_{22}}{Q_{11} + Q_{22} + 2\sqrt{Q_{11}Q_{22} - Q_{12}}}, \tag{1.2.8}$$

$$\epsilon_2 = \frac{2Q_{12}}{Q_{11} + Q_{22} + 2\sqrt{Q_{11}Q_{22} - Q_{12}}}, \tag{1.2.9}$$

in terms of the elements of Q. From the position angle, i.e. the angle between the x-axis and the major axis a, we obtain the shear direction $\phi = \arg(\gamma)$ as

$$\tan(2\phi) = \frac{\epsilon_2}{\epsilon_1} = \frac{2Q_{12}}{Q_{11} - Q_{22}}. \tag{1.2.10}$$

So we see that we get all the relevant quantities from the elements of the tensor Q. In practice, the integrals for the Q_{ij} in equation 1.2.2 must be replaced by finite sums over the individual image pixels. In addition, noise in real astronomical images affects shape measurements at a low surface brightness. By defining a brightness level I_{th}, one can counteract this problem by considering only pixels with a brightness above I_{th} in the summation.

Under the assumption of a random orientation of the source galaxies, i.e. $\langle\epsilon_S\rangle = 0$, we can establish a correspondence between the measured ellipticities and the reduced shear field:

$$\langle\epsilon\rangle = \begin{cases} g & \text{for } |g| \le 1 \\ 1/g^* & \text{for } |g| > 1 \end{cases}. \tag{1.2.11}$$

In this case the reduced shear g corresponds to the expectation value of the observed complex ellipticity. In particular, g is an observable!

1.2.3 KS 93 Algorithm

We finally want to give a short summary of the Kaiser & Squires inversion algorithm, which belongs to the class of free-form methods. In 1993, Kaiser & Squires developed a algorithm for reconstruction convergence maps or mass maps, respecively, from the observed weak lensing shear. This algorithm is today widely known as the KS 93 algorithm. Since the shear and convergence are both linear combinations of the second-order derivatives of the lensing potential, we obtain in Fourier space

$$\tilde{\kappa} = -\frac{1}{2}(k_1^2 + k_2^2)\,\tilde{\Psi} \tag{1.2.12}$$

$$\tilde{\gamma}_1 = -\frac{1}{2}(k_1^2 - k_2^2)\,\tilde{\Psi} \tag{1.2.13}$$

$$\tilde{\gamma}_2 = -k_1 k_2 \tilde{\Psi}, \tag{1.2.14}$$

where $\tilde{\ }$ denotes the Fourier transform of the corresponding quantity and k_1, k_2 the elements of the wave vector k with norm square $k^2 = k_1^2 + k_2^2$. With the three independent equations, we can now eliminate Ψ and express γ as a function of κ:

$$\begin{pmatrix} \tilde{\gamma}_1 \\ \tilde{\gamma}_2 \end{pmatrix} = k^{-2}\begin{pmatrix} k_1^2 - k_2^2 \\ 2k_1 k_2 \end{pmatrix}\tilde{\kappa}. = A\tilde{\kappa}. \tag{1.2.15}$$

Here we introduced the operator

$$A := k^{-2} \begin{pmatrix} k_1^2 - k_2^2 \\ 2k_1k_2 \end{pmatrix}, \tag{1.2.16}$$

which transforms the convergence to the shear vector in Fourier space. Using that A is idempotent

$$AA^T = 0, \tag{1.2.17}$$

we can invert equation 1.2.15 and obtain κ in dependence of γ:

$$\tilde{\kappa} = A^T \begin{pmatrix} \tilde{\gamma}_1 \\ \tilde{\gamma}_2 \end{pmatrix}. \tag{1.2.18}$$

We transform this relation back to real space by taking the inverse Fourier transform

$$\kappa(\theta) - \kappa_0 = \frac{1}{\pi} \int_{\mathbb{R}^2} \left[D_1(\theta - \theta')\gamma_1(\theta') + D_2(\theta - \theta')\gamma_2(\theta') \right] d^2\theta' \tag{1.2.19}$$

where κ_0 is an additive constant and D_1 and D_2 are appropriate kernel functions given by

$$D_1(\theta_1, \theta_2) = \frac{\theta_2^2 - \theta_1^2}{\theta^4}, \tag{1.2.20}$$

$$D_2(\theta_1, \theta_2) = \frac{2\theta_1\theta_2}{\theta^4}. \tag{1.2.21}$$

Note that equation 1.2.19 is a convolution integral, since equation 1.2.18 is a product in Fourier space. By defining the complex kernel function

$$D(\theta) = D_1(\theta) + iD_2(\theta), \tag{1.2.22}$$

we can write equation 1.2.19 as

$$\kappa(\theta) - \kappa_0 = \frac{1}{\pi} \int_{\mathbb{R}^2} \text{Re}[D^*(\theta - \theta')\gamma(\theta')] d^2\theta'. \tag{1.2.23}$$

As mentioned by Seitz and Schneider [1995], under the assumption of vanishing shear at infinity partial integration yields

$$\kappa(\theta) = \frac{1}{\pi} \int_{\mathbb{R}^2} H^{KS}(\theta', \theta) \cdot \begin{pmatrix} \gamma_{1,1}(\theta') + \gamma_{2,2}(\theta') \\ \gamma_{2,1}(\theta') - \gamma_{1,2}(\theta') \end{pmatrix} d^2\theta', \tag{1.2.24}$$

with

$$H^{KS}(\theta', \theta) = \frac{1}{2\pi} \frac{\theta - \theta'}{|\theta - \theta'|^2} = \nabla_{\theta'} \left(-\frac{1}{2\pi} \ln |\theta - \theta'| \right). \tag{1.2.25}$$

This means that in this limit the surface mass density is obtained by convolving the deflection angle field of a point mass with the first derivatives of the shear field.

In chapter 3 we will compare the KS 93 algoithm with our proposed inversion algorithm theoretically and in chapter 4 also numerically.

2 Theoretical Formalism

Here, following Straumann [1997] we first use Wirtinger calculus to transform the basic lensing equations into a complex formulation. In particular, we will see that weak lensing corresponds to quasi-conformal mappings. To illustrate the usefulness of this complex formalism, we give some applications again following Straumann [1997]. We then review the foundations of quasi-conformal geometry, especially existence and uniquess results of planar quasi-conformal mappings as well as quasi-conformal mappings between Riemann surfaces. Advanced topics of quasi-conformal geometry like Teichmüller theory Hubbard [2016] or the connection between quasi-conformal and hyperbolic geometry Bourdon and Pajot [2002] are not treated, because they are not relevant for our study of weak lensing. Last in this chapter we deal with the question of how to compute quasi-conformal mappings between general Riemann surfaces numerically.

2.1 Complex Formalism of Weak Lensing

Wirtinger Calculus: By identifying $\mathbb{C}$ with $\mathbb{R}^2$, we can write $z \in \mathbb{C}$ as $z = x + \mathrm{i}y$ for $x, y \in \mathbb{R}$. Let U be an open subset of $\mathbb{C}$. The two 1-forms $\mathrm{d}z = \mathrm{d}x + \mathrm{i}\mathrm{d}y$ and $\mathrm{d}\bar{z} = \mathrm{d}x - \mathrm{i}\mathrm{d}y$ form a corresponding basis of the cotangent space of all points in U ($T_z U \cong \mathbb{C}$ for all $z \in U$). By defining the so called Wirtinger derivatives

$$\partial_z = \frac{\partial}{\partial z} := \frac{1}{2}\left(\frac{\partial}{\partial x} - \mathrm{i}\frac{\partial}{\partial y}\right), \quad \partial_{\bar{z}} = \frac{\partial}{\partial \bar{z}} := \frac{1}{2}\left(\frac{\partial}{\partial x} + \mathrm{i}\frac{\partial}{\partial y}\right), \tag{2.1.1}$$

we are able to represent the differential of any smooth complex function f on U as

$$\mathrm{d}f = \frac{\partial f}{\partial z}\mathrm{d}z + \frac{\partial f}{\partial \bar{z}}\mathrm{d}\bar{z}. \tag{2.1.2}$$

Let us write shortly f_z and $f_{\bar{z}}$ for $\partial_z f$ and $\partial_{\bar{z}} f$, respectively, and denote with $\mathcal{D}(U)$ the $\mathbb{C}$-algebra of all functions $f : U \to \mathbb{C}$, which are infinitely often differentiable according to the real coordinates x and y. Then, according to the Cauchy-Riemann differential equations the vector space $O(U)$ of holomorphic functions on U is equal to the kernel of the mapping $\partial_{\bar{z}} : \mathcal{D}(U) \to \mathcal{D}(U)$ (cf. Forster [2012]). With the Wirtinger derivatives the Laplacian can be expressed as

$$\Delta = 4\partial_z \partial_{\bar{z}}. \tag{2.1.3}$$

Differential of the Lens Mapping: By applying this formalism to our basic lens equation $\beta : \mathbb{R}^2 \to \mathbb{R}^2$, $\theta \mapsto \beta(\theta)$ in equation 1.1.2, β can be written as the complex function

$$f : \mathbb{C} \to \mathbb{C}, \ z \mapsto f(z) = z - 2\partial_{\bar{z}}\Psi = \partial_{\bar{z}}(z\bar{z} - 2\Psi). \tag{2.1.4}$$

Using 2.1.3 and 2.1.4 the Poisson equation 1.1.11 becomes

$$2\partial_z \partial_{\bar{z}}\Psi = \kappa, \tag{2.1.5}$$

and similar for the shear, if we take into account the definition of the complex shear vector:

$$\partial_{\bar{z}}^2 \Psi = \frac{1}{4}(\partial_1^2 - \partial_2^2)\Psi + \frac{\mathrm{i}}{2}\partial_1\partial_2\Psi = \frac{1}{2}(\gamma_1 + \mathrm{i}\gamma_2) = \frac{1}{2}\gamma. \tag{2.1.6}$$

With 2.1.4, 2.1.5 and 2.1.6 we can now determine the differential 2.1.2 of f:

$$\mathrm{d}f = \partial_z f \mathrm{d}z + \partial_{\bar{z}} f \mathrm{d}\bar{z} = (1 - \kappa)\mathrm{d}z - 2\partial_{\bar{z}}^2\Psi \mathrm{d}\bar{z} = (1 - \kappa)\mathrm{d}z - \gamma\mathrm{d}\bar{z}. \tag{2.1.7}$$

Beltrami Equation and Quasi-Conformal Mappings: We say that a function $f : \Omega_1 \to \Omega_2$, which we assume to be at least continuously partial differentiable, between two domains Ω_1 and Ω_2 of the complex plane fullfills the *Beltrami equation*, if

$$f_{\bar{z}} = \mu f_z \tag{2.1.8}$$

holds on Ω_1, where μ is a complex-valued function on Ω_1 and Lebesgue measurable. μ is called the *dilatation* or *Beltrami coefficient* of f and contains all information about the conformality of f. The Beltrami equation plays a crucial role in the theory of quasi-conformal mappings: f is said to be *quasi-conformal* (*q.c.*) if it fullfills the Beltrami equation 2.1.8 and

$$\|\mu\|_\infty = \operatorname*{esssup}_{x \in U} |\mu(x)| \le k < 1 \tag{2.1.9}$$

holds for some $k \in \mathbb{R}$. Considering the Jacobian J_f of f given by

$$J_f = |f_z|^2 - |f_{\bar{z}}|^2 = |f_z|^2 (1 - |\mu|^2). \tag{2.1.10}$$

It is clear that f is q.c. if it fullfills the Beltrami equation and preserves orientation ($J_f > 0$). Furthermore, $\mu \equiv 0$ if and only if f is conformal. Thus, q.c. mappings are a generalization of conformal mapppings. As we see in the following subsection about geometric interpretation, q.c. mappings are essential the homeomorphisms, which map infinitesimal circles to ellipses of bounded eccentricity (cf. Lui et al. [2013a]).

Lens Mapping is Quasi-Conformal: We have already computed the differential of the complexified lens mapping f in 2.1.7. By comparing 2.1.2 with 2.1.7, we easily obtain the Beltrami coefficient of the lens mapping

$$\mu = \frac{f_{\bar{z}}}{f_z} = -\frac{\gamma}{1 - \kappa} = -g \tag{2.1.11}$$

as the negative of the reduced shear. For weak lensing, the lens mapping does not only fullfill the Beltrami equation, but also condition is satisfied due to $\|g\| \le k < 1$ for some $k \in \mathbb{R}$. Otherwise, the Jacobian J_f would become singular and we would find ourselves in the case of multiple images and strong lensing. In particular, in many use cases of weak lensing even $\|\kappa\|, \|\gamma\| \ll 1$, which gives us $\|g\| \approx \|\gamma\| \ll 1$. Thus, in case of weak lensing the lens mapping f is q.c.. As we in section 2.3 about analytic properties of planar q.c. mappings the lens mapping f is uniquely determined by the negative of the reduced shear as Beltrami coefficient and some appropriate boundary conditions.

As examples for lens mappings and its corresponding Beltrami coefficients we consider two important examples of lenses as proposed by Straumann [1997]: The Schwarzschild and the singular isothermal lens. For the first lens we obtain

$$f(z) = z - \frac{1}{\bar{z}}, \quad \mu = \frac{1}{\bar{z}^2}; \tag{2.1.12}$$

and for the latter

$$f(z) = z - \frac{z}{|\bar{z}|}, \quad \mu = \frac{z^2}{2|\bar{z}|^3 - |\bar{z}|^2}. \tag{2.1.13}$$

In chapter 4 these two examples for $|z|$ large enough are also treated numerically to show the validity of our proposed algorithm.

Geometric Interpretation: Let us have a look on the geometric interpretation of being q.c. by considering an infinitesimal ellipse field that is constructed in the following way: As shown in figure 3, we assign each point $z \in U$ an infinitesimal circle that is mapped by f to a infinitesimal ellipse of bounded eccentricity

$$K_f(z) := \frac{|f_z| + |f_{\bar{z}}|}{|f_z| - |f_{\bar{z}}|} = \frac{1 + |\mu(z)|}{1 - |\mu(z)|}. \tag{2.1.14}$$

$K_f(z)$ is called *dilatation of f at z*. By taking the (essential) supremum over all points in U we obtain the notion of the *dilatation of f*

$$K_f := \operatorname*{esssup}_{z \in U} K(f, z) = \frac{1 + \|\mu\|_\infty}{1 - \|\mu\|_\infty}, \tag{2.1.15}$$
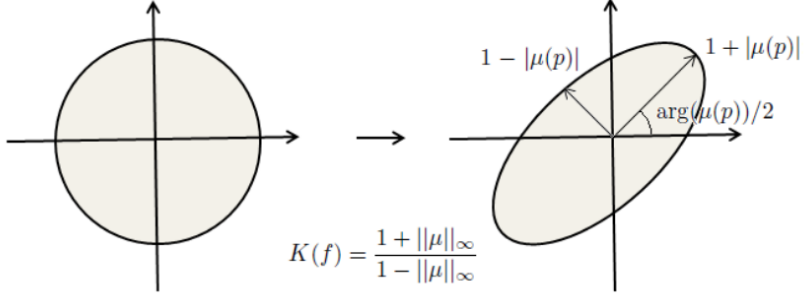
Figure 3: Geometric interpretation of quasi-conformal mappings, figure from Lui et al. [2013a]

which is well-defined for a q.c. mapping since $1 - \|\mu\|_\infty \geq 1 - k > 0$. The argument of the major axis $a = 1 + |\mu(z)|$ of this infinitesimal ellipse can also expressed in terms of the Beltrami coefficient by

$$\arg(1 + |\mu(z)|) = \arg(\mu(z))/2. \tag{2.1.16}$$

A derivation of the equations 2.1.14 - 2.1.16 is provided in chapter 2.4.2. Geometrically this means that there is a fixed bound in the stretching for f in any given direction compared to any other direction. Solving the Beltrami equation 2.1.8 is then equivalent to find a function f whose associated ellipse field (with bounded eccentricity) coincides with the prescribed Beltrami coefficient field μ. We shall see that this is just the inversion problem in gravitational lensing, where the negative of the reduced shear g plays the role of μ.

2.2 Analytical Applications of Complex Formalism

Following Straumann [1997], we want to show that this complex formalism is useful to derive some well-known results from gravitational lensing in a simpler and more natural way. The numerical advantages of considering the lens mapping f as q.c. mapping have not yet been investigated by other authors and are treated later in chapter 3 and 4.

2.2.1 Integral Expression for the Deflection Field

From the previous section we know that f is not holomorphic unless $g \equiv 0$. In particular, Cauchy's integral formula for holomorphic functions does not hold. Instead, we obtain a weaker statement called *Cauchy-Pompeiu's formula*: Let $\Omega \subset \mathbb{C}$ be a compact subset with smooth boundary $\partial\Omega$. Due to Stokes' theorem applied to the complex plane it holds for every complex differential form ω

$$\int_\Omega \mathrm{d}\omega = \int_{\partial\Omega} \omega. \tag{2.2.1}$$

If we consider the differential form

$$\omega = f \frac{\mathrm{d}z}{z - \zeta}, \tag{2.2.2}$$

we can apply equation 2.2.1 for Ω minus an ϵ-disk centered around ξ. $\epsilon \to 0$ then yields the so-called Cauchy-Pompeiu's formula

$$f(\xi) = \frac{1}{2\pi\mathrm{i}} \int_{\partial\Omega} \frac{f(z)}{z - \zeta} \mathrm{d}z + \frac{1}{2\pi\mathrm{i}} \int_\Omega \frac{f_{\bar{z}}(z)}{z - \zeta} \mathrm{d}z \wedge \mathrm{d}\bar{z}. \tag{2.2.3}$$

The $\wedge$-product can be expressed as $\mathrm{d}z \wedge \mathrm{d}\bar{z} = -2\mathrm{i}\mathrm{d}x \wedge \mathrm{d}y$. In case f is holomorphic the last integral vanishes and one just obtains Cauchy's formula.

2.2.2 Number of Images of a Regular Lens

Under the assumption, that the source does not lie on a caustic, the *odd number theorem* of strong lensing states that for a regular lens the number of images must always be odd. It is a well-known theorem lying on the intersection between gravitational lensing and differential topology, i.e. the standard proof uses Morse theory. As Straumann [1997] has shown, the result can also be obtained by means of elementary complex analysis using the above formalism. We briefly sketch the proof here.

The winding number (or index) of a closed curve γ with respect to a point $z_0 \in \mathbb{C}$; $a \notin \gamma$ is defined by

$$\text{ind}_\gamma(z_0) = N(\gamma, z_0) := \frac{1}{2\pi i} \int_\gamma \frac{dz}{z - z_0}. \tag{2.2.4}$$

It is invariant under homotopies and always an integer. We consider a point w_0 in the source plane that is multiple lensed. Denote with $f^{-1}(w_0) = \{z_1, \ldots, z_N\}$ the multiple images of w_0 in the lens plane and define the complex 1-form ω by

$$\omega = \frac{1}{2\pi i} \frac{df}{f - w_0}. \tag{2.2.5}$$

Then ω is regular on $\mathbb{C} \setminus \bigcup_{j=1}^{N} D_\epsilon(z_j)$, where $D_\epsilon(z_j)$ denotes a closed disk of radius ϵ centered around z_j. Since $d\omega = 0$, i.e. ω is closed, it follows

$$\frac{1}{2\pi i} \int_{\partial D_R(0)} \frac{df}{f - \omega_0} = \sum_{j=1}^{N} \frac{1}{2\pi i} \int_{\partial D_\epsilon(z_j)} \frac{df}{f - w_0}. \tag{2.2.6}$$

Here, R was chosen so large that all circular disks $D_\epsilon(z_j)$ are contained in $D_R(0)$. In the limit $|z| \to \infty$ the lens mapping becomes the identity and we obtain

$$\frac{1}{2\pi i} \int_{\partial D_R(0)} \frac{df}{f - w_0} = 1 \tag{2.2.7}$$

for R sufficiently large. Due to the transformation formula of integration we have for a closed curve γ

$$\frac{1}{2\pi i} \int_\gamma \frac{df}{f - w_0} = \frac{1}{2\pi i} \int_{f \circ \gamma} \frac{dw}{w - w_0} = \text{ind}_{f \circ \gamma}(w_0). \tag{2.2.8}$$

Together with 2.2.6 and 2.2.7 this yields

$$1 = \sum_{j=1}^{N} \text{ind}_{f \circ \partial D_\epsilon(z_j)}(w_0) = n_1 - n_{-1} + 2(n_2 - n_{-2}) + \ldots. \tag{2.2.9}$$

n_i denotes the number of the z_j with index equal to i. Consider now the case when w_0 does not lie on a caustic. Then, $J_f(z_j) \neq 0$ and $n_i = \pm 1$, depending on whether f is orientation preserving or reversing at z_j. This gives us

$$N = n_1 + n_{-1}, \quad 1 = n_1 - n_{-1} \quad \Rightarrow N = 1 + 2n_{-1}. \tag{2.2.10}$$

Since N is always odd, equation 2.2.10 is just the statement of the odd number theorem.

2.2.3 Relations between Mean Convergence and Reduced Shear

The complex formulation of the lens mapping allows us also to derive the common relations between reduced shear, which is in principle observable, and the convergence κ, from which we can infer the surface mass density. The idea is to apply the operators ∂_z and $\partial_{\bar{z}}$ to the coefficients of the differential in 2.1.7. As we have seen for the KS 93 algorithm, it is natural to first establish a relation between convergence and shear. We start with

$$\gamma = -\partial_{\bar{z}} f = 2\partial_{\bar{z}}^2 \Psi. \tag{2.2.11}$$

Following our idea we apply the ∂_z-operator to this equation and obtain

$$\partial_z \gamma = 2\partial_{\bar{z}}(\partial_z \partial_{\bar{z}} \Psi) = \partial_{\bar{z}} \kappa. \tag{2.2.12}$$

If one takes $\partial \gamma$ as inhomengenity, this is just an inhomogeneous Cauchy-Riemann equation for κ. In case $\partial_z \gamma$ is smooth and has compact support, Cauchy-Pompeiu's formula 2.2.3 provides the solution

$$\kappa(z_0) = \frac{1}{2\pi i} \int_{\mathbb{C}} \frac{\partial_z \gamma(z)}{z - z_0} dz \wedge d\bar{z}. \tag{2.2.13}$$

The solution is not unique, since κ is only determined up to an additive holomorphic function and unique up to an additive constant if κ is bounded (Liouville's theorem). We state that $(\pi z)^{-1}$ is the fundamental solution of the Cauchy-Riemann differential operator $\partial_{\bar{z}}$, i.e.

$$\frac{1}{\pi} \partial_{\bar{z}} \left(\frac{1}{z} \right) = \delta_D, \tag{2.2.14}$$

where δ_D denotes the Dirac delta distribution: For the proof of this statement let $\phi \in C_c^\infty(\mathbb{C})$ be a smooth test function with compact support. Then it holds:

$$\left\langle \frac{\partial}{\partial \bar{z}} \frac{1}{\pi z}, \phi \right\rangle = -\frac{1}{2\pi i} \int_{\mathbb{C}} \frac{1}{z} \frac{\partial}{\partial \bar{z}} \phi(z) d\bar{z} \wedge dz = -\lim_{\epsilon \to 0} \frac{1}{2\pi i} \int_{\mathbb{C} \backslash B_\epsilon} \left(\frac{1}{z} \frac{\partial}{\partial \bar{z}} \phi(z) + \phi(z) \frac{\partial}{\partial \bar{z}} \frac{1}{z} \right) d\bar{z} \wedge dz$$

$$= -\lim_{\epsilon \to 0} \frac{1}{2\pi i} \int_{\mathbb{C} \backslash B_\epsilon} \frac{\partial}{\partial \bar{z}} \frac{\phi(z)}{z} d\bar{z} \wedge dz = \lim_{\epsilon \to 0} \frac{1}{2\pi i} \int_{\mathbb{R}^2 \backslash B_\epsilon} \left(i \frac{\partial}{\partial x} \frac{\phi(x+iy)}{x+iy} - \frac{\partial}{\partial y} \frac{\phi(x+iy)}{x+iy} \right) dxdy$$

$$= \lim_{\epsilon \to 0} \frac{1}{2\pi i} \int_{\partial B_\epsilon} \left(\frac{\phi(x+iy)}{x+iy} dx + i \frac{\phi(x+iy)}{x+iy} dy \right) = \lim_{\epsilon \to 0} \frac{1}{2\pi i} \int_{\partial B_\epsilon} \frac{\phi(z)}{z} dz$$

$$= \phi(0). \tag{2.2.15}$$

This is just the defining property of the Dirac delta distribution. Using the fundamental solution of $\partial_{\bar{z}}$, we can express κ as convolution of the fundamental solution with the inhomogeneous part $\partial_z \gamma$:

$$\kappa(z) = \frac{1}{\pi} \left(\frac{1}{z} \right) * \partial_z \gamma + \kappa_0 = \frac{1}{\pi} \partial_z \left(\frac{1}{z} \right) * \gamma + \kappa_0 = -\frac{1}{\pi} \frac{1}{z^2} * \gamma + \kappa_0 = -\frac{1}{\pi} \int_{\mathbb{C}} \frac{1}{w^2} \gamma(z-w) dw + \kappa_0. \tag{2.2.16}$$

As mentioned by Straumann [1997] and proven by Forster [2012] a special case of the Dolbeault lemma implies that we can drop the assumption of the compact support of $\partial_z \gamma$ for the validity of this relation. The constant term κ_0 has also a physical interpretation, namely the mass sheet degeneracy. Since a homogenous mass sheet does not produce any shear, we have to add this constant term to κ. Equation 2.2.16 is just the standard KS 93 inversion algorithm (cf. equation 1.2.19). We can replace γ by g and obtain

$$\kappa = -\frac{1}{\pi} \frac{1}{z^2} * (g(1-\kappa)) + \kappa_0, \tag{2.2.17}$$

which is the extension of the KS 93 algorithm to the non-linear regime (cf. equation 3.1.71). In the same way we can derive the well-known relation of γ in dependence of κ. By using the fundamental solution G of the two dimensional Laplace operator given by

$$G = \frac{1}{2\pi} \ln|z| = \frac{1}{4\pi} \ln(z\bar{z}), \tag{2.2.18}$$

we obtain from equation 2.1.5 and 2.1.6

$$\gamma = -\frac{1}{\pi} \frac{1}{z^2} * \kappa. \tag{2.2.19}$$

We apply the differential operator ∂_z a second time to γ and obtain

$$\partial_z \partial_{\bar{z}} \kappa = \partial_z^2 \gamma. \tag{2.2.20}$$

12

This gives us using the complex representation of the Laplace operator in equation 2.1.3

$$\Delta \kappa = 4 \partial_z^2 (g(1 - \kappa)).\qquad(2.2.21)$$

Again, we could use this result to derive the KS 93 relation between convergence and shear in equation 1.2.19. However, we still want to look at the mass sheet degeneracy in this formalism. Therefore, we write equation 2.2.12 in the following manner:

$$\partial_{\bar{z}} \kappa = \partial_z(g(1 - \kappa)) = (1 - \kappa)\partial g - g\partial \kappa.\qquad(2.2.22)$$

By defining $K := \ln(1 - \kappa)$ this simplifies to

$$\partial_{\bar{z}} K - g\partial K = \partial g.\qquad(2.2.23)$$

We add to this its complex conjugate, which yields

$$\partial_{\bar{z}} K = h(g),\qquad(2.2.24)$$

where

$$h(g) = (1 - |g|)^{-1}(\partial g + \overline{g\partial g}).\qquad(2.2.25)$$

Equation 2.2.24 is again an inhomogeneous Cauchy-Riemann differential equation with inhomogeneity $h(g)$, which is in principle observable. The real-valued form of equation 2.2.23 was first derived by Kaiser [1995].

2.2.4   Other Useful Relations

Integral Expression for Reduced Shear on Bounded Domains: In the previous subsection we always assumed that the corresponding quantities are defined on the whole complex plane and we can integrate over all of $\mathbb{C}$. However, lensing measurements are always confined to a finite field of the sky. We therefore need to adapt our derived formulas to the finite case, where only integration over bounded domains occurs. To arrive at the adapted formulas, we need to have a closer look at complex differential 1-forms on open subsets U of $\mathbb{C}$.

With $T^{1,0} := \mathbb{C}dz$ and $T^{0,1} := \mathbb{C}d\bar{z}$ we denote the one-dimensional sub-vector spaces of the cotangential space $T^{(1)}$ at an arbitrary point in U. By construction, $T^{(1)} = T^{1,0} \oplus T^{0,1}$ holds. Since we are still working in the complex plane in this chapter (and will deal with Riemann surfaces only in the next chapter), the spaces considered are independent of the choice of the concrete base point. For this reason, the base point does not appear in the notation of the corresponding spaces.

A complex 1-form ω is called of type $(1, 0)$ or $(0, 1)$, if $\omega(z) \in T^{1,0}$ or $\omega(z) \in T^{0,1}$ for all $z \in U$, respectively. $\mathcal{E}^{(1)}(U)$ denotes the vector space of all differentiable 1-forms, $\mathcal{E}^{(1,0)}(U)$ the sub-space of 1-forms of type $(1, 0)$ and $\mathcal{E}^{(0,1)}(U)$ the sub-space of 1-forms of type $(0, 1)$. Due to $T^{(1)} = T^{1,0} \oplus T^{0,1}$, a complex 1-form $\omega \in \mathcal{E}^{(1)}(U)$ can always be decomposed as $\omega = \omega_1 + \omega_2$ with $\omega_1 \in \mathcal{E}^{(1,0)}(U)$ and $\omega_2 \in \mathcal{E}^{(0,1)}(U)$. Let h be a differentiable function on U. Additionally to the differential dh in equation 2.1.2 we can define the 1-forms $d'h$ and $d''h$ by

$$(d'f)(z_0) := d'_{z_0}f = (\partial_z f)(z_0)dz, \quad (d''f)(z_0) := d''_{z_0}f = (\partial_{\bar{z}} f)(z_0)d\bar{z}.\qquad(2.2.26)$$

h is holomorphic if and only if $d''h = 0$. Despite the usual relations $d = d' + d''$ and $d' \circ d' = d'' \circ d'' = 0$, it holds $d' \circ d'' + d'' \circ d' = 0$. We also need in the following the Hodge star operator $*$ applied to 1-forms. For a 1-form $\omega = \omega_1 + \omega_2$ it holds

$$* \omega = i(\overline{\omega_1} - \overline{\omega_2}).\qquad(2.2.27)$$

More about complex differential forms can be found in Forster [2012].

Let us come back to gravitational lensing by considering a bounded domain $\Omega \subset \mathbb{C}$ with smooth boundary $\partial\Omega$ and $A = |\Omega|$. The average of the reduced shear g over Ω can be calculated as

$$\overline{g} = \frac{1}{A} \int_\Omega g \mathrm{d}x \wedge \mathrm{d}y. \tag{2.2.28}$$

Our goal is to derive an integral expression for the difference $g - \overline{g}$ in terms of the differential 1-forms $\omega := \mathrm{d}''g$ and $\alpha := 2\mathrm{d}''H$, where H denotes the real Green's function of the Laplace operator with Neumann boundary conditions on $\partial\Omega$. Let us consider the 2-form $*\alpha \wedge \omega$. By a simple calculation using the relation $\mathrm{d}(f * \omega) = f\mathrm{d} * \omega - *\omega \wedge \mathrm{d}f$ for a zero-form (or function) f and a 1-form ω, we obtain

$$* \alpha \wedge \omega = *2\mathrm{d}''H \wedge \mathrm{d}''g = -\mathrm{d}''(g * 2\mathrm{d}''H) + 2g\mathrm{d}''(*\mathrm{d}''H). \tag{2.2.29}$$

For the last term we obtain

$$2g\mathrm{d}''(*\mathrm{d}''H) = -2\mathrm{i}g\mathrm{d}''\mathrm{d}'H = -g\Delta H \mathrm{d}x \wedge \mathrm{d}y, \tag{2.2.30}$$

while the first term can be expressed as

$$-\mathrm{d}''(g * 2\mathrm{d}''H) = -\mathrm{d}(g * \mathrm{d}''H). \tag{2.2.31}$$

Hence,

$$\int_\Omega *\alpha \wedge \omega = - \int_\Omega g * \mathrm{d}''H + g - \overline{g}, \tag{2.2.32}$$

where we have used Stokes' theorem and

$$\Delta H - \frac{1}{A} = -\delta. \tag{2.2.33}$$

Complex Derivation of the ζ-Statistics: Using the complex formalism, we are able to derive the so called *aperture mass densitometry* or *ζ-statistics* which establishes a connection between the projected mass density within an annulus and the tangential shear γ_t. We start with the differential of the lens equation in the form

$$\mathrm{d}(f - z) = -\kappa\, \mathrm{d}z - \gamma\mathrm{d}\overline{z}. \tag{2.2.34}$$

We wedge this with $\mathrm{d}\overline{z}$ and add the complex conjugate of the resulting equation, which gives us

$$\kappa\mathrm{d}z \wedge \mathrm{d}\overline{z} = \frac{1}{2}\mathrm{d}(\kappa(z\mathrm{d}\overline{z} - \overline{z}\mathrm{d}z) + \gamma\overline{z}\mathrm{d}\overline{z} - \overline{\gamma}z\mathrm{d}z). \tag{2.2.35}$$

By taking the average along the boundary $\partial\Omega$ according to equation 2.2.28 we obtain

$$\overline{\kappa} = \frac{\oint \kappa(z\mathrm{d}\overline{z} - \overline{z}\mathrm{d}z)}{\oint(z\mathrm{d}\overline{z} - \overline{z}\mathrm{d}z)} + \frac{\oint(\gamma\overline{z}\mathrm{d}\overline{z} - \overline{\gamma}z\mathrm{d}z)}{\oint(z\mathrm{d}\overline{z} - \overline{z}\mathrm{d}z)}, \tag{2.2.36}$$

where we used Stokes theorem to reduce the integration of the differential of the 1-form in equation 2.2.35 to a path integral over it. If Ω corresponds to a circular disk D_r of radius r, we have $z = re^{\mathrm{i}\varphi}$, $z\mathrm{d}\overline{z} - \overline{z}\mathrm{d}z = -2\mathrm{i}r^2\mathrm{d}\varphi$ along ∂D_r, which simplifies equation 2.2.36 to

$$\overline{\kappa} = \langle\kappa\rangle + \langle\gamma_t\rangle. \tag{2.2.37}$$

γ_t denotes the tangential component of the shear, given by

$$\gamma_t = \gamma_1\cos(2\varphi) + \gamma_2\sin(2\varphi). \tag{2.2.38}$$

Using polar coordinates, we obtain

$$\overline{\kappa} = \frac{1}{\pi r^2} \int_0^r \kappa(r', \varphi)r'\mathrm{d}r'\mathrm{d}\varphi, \tag{2.2.39}$$

and thus

$$\frac{d\overline{\kappa}}{d\ln(r)} = 2\langle\kappa\rangle - 2\overline{\kappa}. \tag{2.2.40}$$

Combining equation 2.2.37 with 2.2.40 yields

$$\frac{d\overline{\kappa}}{d\ln(r)} = -2\langle\gamma_t\rangle. \tag{2.2.41}$$

Solving this ordinary differential equation gives us the ζ-statistics:

$$\zeta(r_1, r_2) = \overline{\kappa}(r_1) - \overline{\kappa}(r_1 < r < r_2) = 2\left(1 - \frac{r_1^2}{r_2^2}\right)^{-1} \int_{r_1}^{r_2} \langle\gamma_t\rangle\frac{dr}{r}. \tag{2.2.42}$$

Complex Derivation of Expressions for Image Ellipticities: As we have seen in the introduction, the second moments Q_{ij} of the brightness distribution $I(\boldsymbol{\theta})$ can be used to determine the image ellipticities ϵ (or χ, depending on the definition), from which we obtain the reduced shear. We now want to use the complex formalism to derive an expression for χ as a function of the Q_{ij}. If we regard $Q = (Q_{ij})$ as representation matrix of a linear map of $\mathbb{R}^2$, we can interpret it as complex-valued map w

$$w : \mathbb{C} \to \mathbb{C}, z \mapsto w(z) := (Q_{11} + Q_{22})\mathrm{Re}(z) + \mathrm{i}(Q_{22} + Q_{21})\mathrm{Im}(z) \tag{2.2.43}$$

$$= \frac{1}{2}(Q_{11} + Q_{22})z + \frac{1}{2}(Q_{11} - Q_{22} + 2\mathrm{i}Q_{12})\overline{z} \tag{2.2.44}$$

$$= \frac{1}{2}\mathrm{tr}(Q)(z + \chi\overline{z}), \tag{2.2.45}$$

where we have identified the complex ellipticity

$$\chi = \frac{Q_{11} - Q_{22} + 2\mathrm{i}Q_{12}}{\mathrm{tr}(Q)} \tag{2.2.46}$$

with the Beltrami coefficient of w. We finally want to derive an expression for the intrinsic complex ellipticity χ^s of the source. As just seen for χ, we therefore need the intrinsic brightness moments Q_{ij}^s of the galaxy to compute χ^s as Beltrami coefficient of the complex map w^s defined by $Q^s = (Q_{ij}^s)$. Due to $Q^s = Df \cdot Q \cdot Df$, where Df denotes the differential of the lens map, we only need to compose the map w with the linearized lens map

$$w_f = (1 - \kappa)z - \gamma\overline{z} \tag{2.2.47}$$

on the right and on the left to obtain

$$w^s = (1 + |g|^2 + 2\mathrm{Re}(g\overline{\chi}))z + (2g + \chi + g^2\overline{\chi})\overline{z}. \tag{2.2.48}$$

χ^s is then given by the Beltrami coefficient of w^s:

$$\chi^s = \frac{2g + \chi + g^2\overline{\chi}}{1 + |g|^2 + 2\mathrm{Re}(g\overline{\chi})}. \tag{2.2.49}$$

Equivalently, one can express χ in terms of χ^s as

$$\chi = \frac{-2g + \chi^s + g^2\overline{\chi}^s}{1 + |g|^2 - 2\mathrm{Re}(g\overline{\chi}^s)}. \tag{2.2.50}$$

As we see, the complex formalism simplifies the derivation of expressions for the image ellipticities significantly by assigning them the role of Beltrami coefficients of some appropriate complex mappings.

2.3 Analytic Properties of Planar Quasi-Conformal Mappings

The theory of q.c. mappings is over 90 years old and has been first studied by Grötzsch [1928], Morrey [1938], Lawrentjew [1935] and Ahlfors [1955]. As already mentioned, q.c. mappings can be considered as a generalization of conformal mappings. Conformal mappings are angle preserving: They map infinitesimal circles on the domain to infinitesimal circles on the image. In contrast, q.c. mappings map infinitesimal ellipses on the domain to infinitesimal circles on the image (cf. Zeng et al. [2012]).

Since the deflection field in the planar case is a q.c. mapping, we need to deal with existence and uniqueness results of q.c. mappings between domains of $\mathbb{C}$. These results will become especially important when for the well-posedness of our proposed algorithm in the planar case in chapter 3. However, we only want to give the most important statements here and do not want to go further into the concrete theory behind. For detailed proofs we refer to relevant literature like Lehto [1973], Gmira [2016] or Zakeri.

2.3.1 Basics Facts About Quasi-Conformal Mappings

Generalized Definition of a Quasi-Conformal Mapping: As already seen, q.c. mappings are (almost everywhere) differentiable homeomorphisms with bounded small-scale geometry. In the following, let Ω_1, Ω_2 and Ω_3 be domains in $\mathbb{C}$. A q.c. mapping $f : \Omega_1 \to \Omega_2$ has three essential features:

 (i) It is an orientation-preserving homeomorphism.

 (ii) It is differentiable at almost every $p \in U$ and the derivative $Df(p) : \mathbb{R}^2 \to \mathbb{R}^2$ is non-singular.

 (iii) The differential $Df(p)$ at p pulls back round circles to ellipses with bounded eccentricity, which is independent of p.

These three properties essentially describe what it means to be q.c., except that the existence of the derivative almost everywhere should be replaced by a stronger condition called *absolutely continuity on lines* (ACL): This means that for every closed rectangle $[a, b] \times [c, d] \subset \Omega_1$, the restriction $x \mapsto f(x + iy)$ is absolutely continuous on $[a, b]$ for almost everywhere $y \in [c, d]$, and the restriction $y \mapsto f(x + iy)$ is absolutely continuous on $[c, d]$ for almost everywhere $x \in [a, b]$. Equivalently it can be replaced by f having locally integrable partial derivatives in the sense of distributions. We give a new definition of a q.c. mapping: $f : \Omega_1 \to \Omega_2$ is called q.c. if

 (i) it is an orientation-preserving homeomorphism.

 (ii) it is ACL.

 (iii) the partial derivates of f (which by (ii) exist almost everywhere) satisfy $|f_{\bar{z}}| \leq k|f_z|$ almost everywhere in Ω_1, for some constant $0 \leq k < 1$.

This definition from Zakeri is often found in the literature and presents a generalization of the one above, where we required that f should be at least continuously partial differentiable. To make the attribute more quantitative, we say that f is *K-q.c.*, where $K := (1 + k)/(1 - k) \leq 1$.

We consider two examples. First, let $K \geq 1$ and define $f : \mathbb{C} \to \mathbb{C}$ by

$$f(x + iy) := \begin{cases} x + iKy & \text{if } y \geq 0 \\ x + iy & \text{if } y < 0 \end{cases}. \tag{2.3.1}$$

f is ACL, with derivatives

$$f_z(x + iy) := \begin{cases} (1 + K)/2 & \text{if } y > 0 \\ 1 & \text{if } y < 0 \end{cases} \quad \text{and} \quad f_{\bar{z}}(x + iy) := \begin{cases} (1 + K)/2 & \text{if } y > 0 \\ 0 & \text{if } y < 0 \end{cases}. \tag{2.3.2}$$

The partial derivatives do not exist along the real axis unless $K = 1$. Due to $K \geq 1$, $|\mu| = |f_{\bar{z}}/f_z| \leq k := (K - 1)/(K + 1) < 1$. Thus, f is K-q.c..

As a second example let $0 \leq k < 1$ and define $f : \mathbb{C} \to \mathbb{C}$ by

$$f(z) := \begin{cases} z + k\bar{z} & \text{if } |z| \leq 1 \\ z + k/z & \text{if } |z| > 1 \end{cases}. \tag{2.3.3}$$

Again, f is ACL, with

$$f_z(z) := \begin{cases} 1 & \text{if } |z| < 1 \\ 1 - k/z^2 & \text{if } |z| > 1 \end{cases} \quad \text{and} \quad f_{\bar{z}}(z) := \begin{cases} k & \text{if } |z| < 1 \\ 0 & \text{if } |z| > 1 \end{cases}. \tag{2.3.4}$$

Here, the partial derivatives do not exist along the unit circle unless $k = 0$. Thus, f is K-q.c. with $K = (1 + k)/(1 - k)$.

Basic Properties of Quasi-Conformal Mappings: Using the generalized definition, we want to give some basic but important properties of q.c. mappings. Let $f : \Omega_1 \to \Omega_2$ be a K_f q.c. mapping. Then the following regularity statements hold:

1. f is differentiable almost everywhere in Ω_1, i.e.

$$f(p + z) = f(p) + f_z(p)z + f_{\bar{z}}(p)\bar{z} + \epsilon(z), \tag{2.3.5}$$

   for $p \in \Omega_1$ almost everywhere and $\epsilon(z)/z \to 0$ for $z \to 0$.

2. The Jacobian $J_f = |f_z|^2 - |f_{\bar{z}}|^2$ is positive almost everywhere and locally integrable in Ω_1. Furthermore,

$$\int_E J_f \mathrm{d}x\mathrm{d}y = \int_{f(E)} \mathrm{d}x\mathrm{d}y = \text{area}(f(E)) \tag{2.3.6}$$

   holds for every measurable set $E \subset \Omega_1$. As a corollary, it follows that f maps sets of area zero to sets of area zero.

3. f_z and $f_{\bar{z}}$ are locally square-integrable in Ω_1. In fact, it holds

$$|f_z|^2 \leq \frac{1}{1 - k^2} J_f \quad \text{and} \quad |f_{\bar{z}}|^2 \leq \frac{k^2}{1 - k^2} J_f. \tag{2.3.7}$$

4. The partial derivatives f_z and $f_{\bar{z}}$ are the distributional derivatives also, i.e.

$$\int_{\Omega_1} f_z \phi = -\int_{\Omega_1} f\phi_z \quad \text{and} \quad \int_{\Omega_1} f_{\bar{z}} \phi = -\int_{\Omega_1} f\phi_{\bar{z}} \tag{2.3.8}$$

   for every compactly supported smooth test function $\phi : \Omega_1 \to \mathbb{C}$.

Since the lens mapping can be assumed to be smooth, the above regularity statements are automatically true for f. Let us consider statements about f that go beyond regularity statements:

1. The inverse f^{-1} is also K_f-q.c.

2. $f_z \neq 0$ almost everywhere on Ω_1. This is in accordance with the condition $\|\mu\|_\infty = \|f_{\bar{z}}/f_z\|_\infty < 1$.

3. Weyl's lemma: If $K_f = 1$, then f is conformal.

If we consider concatenations of q.c. mappings, we obtain:

1. For every K_g-q.c. mapping g of $f(\Omega_1)$, the composed mapping $g \circ f$ is $K_f K_g$-q.c.

2. Being K-q.c. is conformally invariant: Namely for conformal mappings h_1 and h_2 of domains Ω_1 and Ω_2 respectively, the composed mapping $h_2 \circ f \circ h_1 : \Omega_1 \to \Omega_2$ is also K-q.c.

3. Let μ be a measurable function on Ω_1 such that $\|\mu\|_\infty \leq k < 1$ for some $k \in \mathbb{R}$. If there exists a q.c. mapping f with Beltrami coefficient $= \mu$, then for every conformal mapping h of $f(\Omega_1)$, the mapping $h \circ f$ has the same Beltrami coefficient μ. Conversely, for every quasi-conformal mapping g with $\mu_g = \mu$, the map $g \circ f^{-1}$ is a conformal mapping of $f(\Omega_1)$. As we see in the following subsection such a mapping f always exists.

The last proposition follows therby directly from 2. and Weyl's lemma. Let us now derive the chain rule for q.c. mappings: Suppose $f : \Omega_1 \to \Omega_2$ and $g : \Omega_2 \to \Omega_3$ are q.c.. As we just stated, $g \circ f : \Omega_1 \to \Omega_3$ is q.c.. Since f and g are differentiable almost everywhere in Ω_1 or Ω_2 respectively, there are sets of measure zero $A \subset \Omega_1$ and $B \subset \Omega_2$ away from which f and g are differentiable. Furthermore, $f^{-1}(B)$ has measure zero. This follows from the fact, that f^{-1} is also q.c. and thus maps sets of measure zero to sets of measure zero. As consequence, $g \circ f$ is differentiable outside the set $A \cup f^{-1}(B)$ and the following chain rule formulas hold:

$$(g \circ f)_z = (g_z \circ f)f_z + (g_{\bar{z}} \circ f)\overline{f_z}, \tag{2.3.9}$$

$$(g \circ f)_{\bar{z}} = (g_z \circ f)f_{\bar{z}} + (g_{\bar{z}} \circ f)\overline{f_{\bar{z}}}. \tag{2.3.10}$$

These two equations yield the following formula for the Beltrami coefficient of the composition of two q.c. mappings f and g:

$$\mu_{g \circ f} = \frac{(g \circ f)_{\bar{z}}}{(g \circ f)_z} = \frac{(g_z \circ f)f_{\bar{z}} + (g_{\bar{z}} \circ f)\overline{f_{\bar{z}}}}{(g_z \circ f)f_z + (g_{\bar{z}} \circ f)\overline{f_z}} = \frac{f_{\bar{z}} + (\mu_g \circ f)\overline{f_z}}{f_z + (\mu_g \circ f)\overline{f_{\bar{z}}}} = \frac{\mu_f + (\mu_g \circ f)\frac{\overline{f_{\bar{z}}}}{f_z}}{1 + \overline{\mu_f}(\mu_f \circ g)\frac{\overline{f_{\bar{z}}}}{f_z}}. \tag{2.3.11}$$

Finally, we want to give a few deeper properties of q.c. mappings, which may be relevant for weak lensing. Proofs for all of these statements can be found in Ahlfors [2006], Astala et al. [2009] or Gilbarg and Trudinger [2015].

1. (Mori) Suppose $\Omega_1 = \Omega_2 = \mathbb{D}$, where $\mathbb{D}$ denotes the unit disk. If f is K-q.c. with $f(0) = 0$, then

$$|f(z) - f(w)| \leq 16|z - w|^{1/K}, \tag{2.3.12}$$

where $z, w \in \mathbb{D}$. As a corollary, it follows that q.c. mappings are locally Hölder: If $f : \Omega_1 \to \Omega_2$ is K-q.c., then for every compact set $E \subset \Omega_1$ there exists a constant $C = C(E, K) > 0$, such that

$$|f(z) - f(w)| \leq C|z - w|^{1/K} \tag{2.3.13}$$

for $z, w \in E$.

2. (Astala) If $f : \mathbb{D} \to \mathbb{D}$ is K-q.c. with $f(0) = 0$, then

$$\text{area}(f(E)) \leq \text{area}(E) \tag{2.3.14}$$

for every measurable set $E \subset \mathbb{D}$ and $C = C(K) > 0$. As a corollary, if $f : \Omega_1 \to \Omega_2$ is K-q.c., then $J_f \in L^p_{\text{loc}}(\Omega_1)$ for every $1 < p < K/(K-1)$.

3. (Astala) Q.c. mappings distort the Hausdorff dimension by a bounded factor: Let $f : \Omega_1 \to \Omega_2$ be K-q.c., $E \subset \Omega_1$, $\dim(E) = \delta$ and $\dim(f(E)) = \delta'$, then

$$\frac{1}{K} \leq \frac{\frac{1}{\delta'} - \frac{1}{2}}{\frac{1}{\delta} - \frac{1}{2}} \leq K. \tag{2.3.15}$$

In particular, f preserves sets of dimension 0 and 2.

Application to Weak Lensing: Using the analytical properties for planar q.c. mappings, it is now simple to make statements about the analytical properties of the deflection field . For this purpose, we grasp the lens mapping f as q.c. mapping on a bounded domain Ω. Then, the following holds:

1. Since $f_z \neq 0$ almost everywhere on Ω, the set of fix points of the deflection field has measure zero.

2. Using equation 2.3.7 and $J_f = 1/\nu$ we can give an upper bound for the absolute value of the shear and an lower bound for the convergence:

$$|f_z|^2 = |1 - \kappa|^2 \leq \frac{1}{\nu} \frac{1}{1 - \|g\|_\infty^2} \quad \text{and} \quad |f_{\bar{z}}|^2 = |\gamma|^2 \leq \frac{1}{\nu} \frac{\|g\|_\infty^2}{1 - \|g\|_\infty^2}, \tag{2.3.16}$$

which gives us

$$\kappa \geq 1 - \sqrt{\frac{1}{\nu} \frac{1}{1 - \|g\|_\infty^2}} \quad \text{and} \quad |\gamma| \leq \sqrt{\frac{1}{\nu} \frac{\|g\|_\infty^2}{1 - \|g\|_\infty^2}}. \tag{2.3.17}$$

Both magnification ν and maximal value $\|g\|_\infty$ of the reduced shear are in principle observable. Moreover, one can assume physical limits for $\|g\|_\infty$, e.g. the largest shear that can reasonably be expected from a physical object. However, note, that both quantities depend on κ and γ, e.g. $\nu = [(1 - \kappa)^2 - |\gamma|^2]^{-1}$.

3. From equation 2.3.6 we obtain a relation between the measure of $f(E)$ of each measurable set $E \subset \Omega$ and the magnification ν integrated over E:

$$\int_E \frac{1}{\nu} \mathrm{d}x\mathrm{d}y = \text{area}(f(E)). \tag{2.3.18}$$

Remark: This is the first work, which uses analytical properties of planar q.c. mappings to infer statements about weak lensing quantities. Note that this goes beyond Straumann's complex formalism introduced above, since we make explicit use of $\|g\|_\infty \leq k < 1$ in the case of weak lensing. However, the question remains whether even more far-reaching statements about the deflection field can be made using this approach and have practical relevance.

2.3.2 Existence and Uniqueness Results of Quasi-Conformal Mappings

As already seen, a q.c. mapping $f : \Omega_1 \to \Omega_2$ between two domains Ω_1 and Ω_2 of $\mathbb{C}$ induces by

$$\mu_f := f_{\bar{z}}/f_z \tag{2.3.19}$$

a bounded measurable function μ_f on Ω_1, with the additional property that $\|\mu_f\|_\infty \leq k < 1$ for some $k \in \mathbb{R}$. Since f_z is non-zero almost everywhere, μ_f is well-defined. μ_f is called the Beltrami coefficient of f, which in turn can be used to define the dilatation of f. Both notions were already introduced in section 2.1.

We can ask the converse question. Namely, whether we can find for every bounded measurable function $\mu : \Omega_1 \to \mathbb{C}$ with $\|\mu\|_\infty \leq k < 1$ a q.c. mapping f, whose Beltrami coefficient μ_f is equal to μ almost everywhere. The answer to this question is yes, which we call the existence theorem for planar q.c. mappings. Note, that the problem can always be transformed to the case when Ω_1 is the whole complex plane: For an arbitrary domain Ω_1, we only need to extend each measurable function μ to $\mathbb{C}$ by setting $\mu^*(z) = \mu(z)$ for $z \in \Omega_1$ and $\mu^*(z) = 0$ for $z \notin \Omega_1$. The function μ^* is then measurable in the whole complex plane. If the problem is solvable for μ^* on $\mathbb{C}$, then the restriction of the solution to Ω_1 solves the original problem.

Existence Theorem for Planar Quasi-Conformal Mappings: For a domain $\Omega_1 \subset \mathbb{C}$ and an arbitrary measurable function μ in Ω_1 with $\|\mu\|_\infty = \operatorname*{esssup}_{x \in U} |\mu(x)| \le k < 1$ for some $k \in \mathbb{R}$, there always exists a q.c. mapping f of Ω_1 whose Beltrami coefficient μ_f coincides with μ almost everywhere in Ω_1.

A proof of this statement can be found in Lehto [1973, p. 190 ff.]. We remark that such a f is not unique: The set of all q.c. mappings of Ω_1 having Beltrami coefficient μ almost everywhere coincides with the family $\{g \circ f\}$, where g runs through all conformal mappings of $f(\Omega_1)$. This follows from the uniqueness theorem stated in Lehto [1973, p. 183]:

Uniqueness Theorem for Planar Quasi-Conformal Mappings: Let $f : \Omega_1 \to \Omega_2$ be a q.c. mapping of Ω_1 with Beltrami coefficient μ_f. Then every q.c. mapping of Ω_1 whose Beltrami coefficient equals μ_f almost everywhere in Ω_1 is of the form $g \circ f$, where g is a conformal mapping of Ω_2.

This is based on the fact that the conformal mappings g do not change the q.c. equivalence class of f. By a remark in Lehto [1973, p. 41 f.] the conformal and q.c. equivalence classes coincide for simply connected domains. In view of the Riemann mapping theorem, which is stated in the following subsection, we deduce from the existence theorem for planar q.c. mappings the following

Mapping Theorem: Let $\Omega_1, \Omega_2 \subset \mathbb{C}$ be conformally equivalent simply connected domains and μ be a measurable function in Ω_1 with $\|\mu\|_\infty = \operatorname*{esssup}_{x \in U} |\mu(x)| \le k < 1$ for some $k \in \mathbb{R}$. Then there exists a q.c. mapping $f : \Omega_1 \to \Omega_2$ whose Beltrami coefficient coincides with μ almost everywhere. This mapping is uniquely determined up to a conformal mapping of Ω_2 onto itself.

It is astonishing that for weak lensing the uniqueness conditions for the lens mapping (and thus the deflection field) do not depend on g itself, but instead on the topology of the domain! On the other hand, this is unsatisfactory for a concrete algorithm: Even for simply connected domains, the question arises how to specify the conformal mapping to make the solution unique, e.g. how to relate it to well-known boundary conditions of the lens mapping. We solved this problem by reducing the Beltrami equation to two elliptic PDEs, once for the real and once for the imaginary part of f. For these two PDEs, we can then specify Dirichlet, Neumann, or mixed boundary conditions and thus obtain a unique solution for the real and imaginary part of f. The exact procedure is considered in chapter 3. Anyway, for certain domains (such as rectangles and circular disks), specifying only the images of certain points and curves is also sufficient.

However, for weak lensing the assumption of simply connected domains often cannot be made. Foreground galaxies in the survey can create holes in the domain, e.g. one can not observe the whole sky, because the milky way is in the way. Therefore, the observation area is not simply connected, but has a north and south dome.

2.4 Foundations of Quasi-Conformal Geometry

In chapter 3 we propose an inversion algorithm for general curved fields, where the flat sky approximation can no longer be assumed. Therefore, we need to generalize the definition of q.c. mappings from domains in the complex plane to Riemann surfaces. Follwing Zeng et al. [2012] and Zakeri, we give a short summary about the major concepts from (quasi-)conformal geometry, which are necessary to understand our proposed inversion algorithm for curved fields.

2.4.1 Riemann Surfaces and Conformal Mappings

Let $n \in \mathbb{N}$ and X be a Hausdorff space, i.e. a space in which two distinct points can be disjointly separated by two open environments. We define a
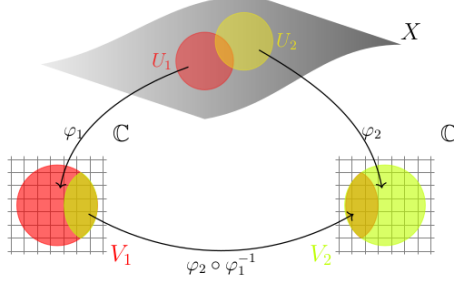
Figure 4: Transition function on a complex one-dimensional manifold, figure from Kasten [2016]

(i) *complex chart of X* as a homeomorphism $\phi : U \to V$, where U is an arbitrary open subset of X and V an open subset of $\mathbb{C}^n$.

(ii) *complex atlas on X* as a system $\mathcal{A} = \{\phi_i : U_i \to V_i, n\text{-dimensional complex chart on } X \mid i \in I \text{ index set }\}$ such that $\bigcup_{i \in I} U_i = X$.

Using these two notions we are able to define a *n*-dimensional *topological complex manifold* as Hausdorff space X together with a *n*-dimensional complex atlas, where X has to be second-countable.

Now let X be a one-dimensional complex manifold. We define:

(i) Two complex charts $\phi_1 : U_1 \to V_1$ and $\phi_2 : U_2 \to V_2$ are called *conformally compatible* if the transition function $\phi_2 \circ \phi_1^{-1} : \phi_1(U_1 \cap U_2) \to \phi_2(U_1 \cap U_2)$ is biholomorphic (i.e. a bijective holomorphic mapping whose inverse is also holomorphic). Alternatively, for $n = 1$, one can assume that the transition function should be conformal. A visualization of a transition function can be found in figure 4.

(ii) If the complex charts of a complex atlas $\mathcal{A}$ on X are pairwise conformal compatible, then we call $\mathcal{A}$ a *conformal atlas* on X.

(iii) Two conformal atlases $\mathcal{A}_1, \mathcal{A}_2$ of X are said to be *conformally compatible* if each complex chart from $\mathcal{A}_1$ is conformally compatible with every complex chart from $\mathcal{A}_2$.

(iv) The conformal compatibility of conformal atlases of X is an equivalence relation. We call an equivalence class under this relation a *complex structure* on X.

This leads us directly to the definition of a *Riemann surface*, which is a pair (X, S) consisting of a connected one-dimensional complex manifold X together with a complex structure S on X.

Let S_1 and S_2 be Riemann surfaces. A continuous map $f : S_1 \to S_2$ is called *holomorphic*, if for each pair of charts $\phi_\alpha : U_\alpha \to \phi_\alpha(U_\alpha)$ of S_1 and $\psi_\beta : V_\beta \to \psi_\beta(V_\beta)$ of S_2 with $\phi_\alpha(U_\alpha) \subset \psi_\beta(V_\beta)$ the function

$$f_{\alpha\beta} = \psi_\beta \circ f \circ \phi_\alpha^{-1} : \phi_\alpha(U_\alpha) \to \psi_\beta(V_\beta) \tag{2.4.1}$$

is holomorphic. Thus, as illustrated in figure 5, using the conformal structure we trace the property of a mapping to be holomorphic back to the properties of the corresponding mappings between open sets in $\mathbb{C}$. f is said to be *conformal* if it is bijective, and both f and its inverse mapping f^{-1} are holomorphic. Two Riemann surfaces are called *conformally equivalent* if there is a conformal mapping between them.
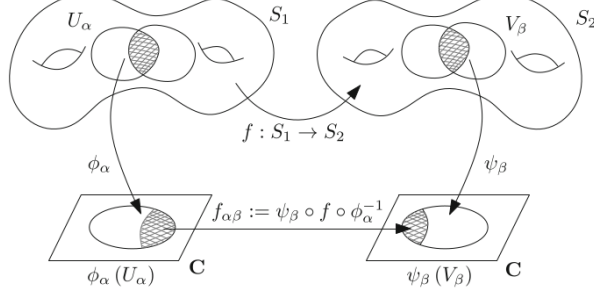
Figure 5: Mapping between Riemann surfaces, figure from Zeng et al. [2012]

Most algorithms that compute q.c. mappings between Riemann surfaces use a different, equivalent definition of a Riemann surface: Let S be a surface embedded in $\mathbb{R}^3$. The metric g on S is given by the induced Euclidean metric. An *isothermal coordinate chart* is a tuple (U_α, ϕ_α), consisting of an open set $U_\alpha \subset S$ and a local parametrization $\phi_\alpha : U_\alpha \to \mathbb{C}$, such that g can be locally written as

$$g = e^{2\lambda(z)}|\mathrm{d}z|^2 = e^{2\lambda(z)}\mathrm{d}z\mathrm{d}\bar{z}, \tag{2.4.2}$$

where the conformal factor $\lambda(z)$ denotes the area distortion under ϕ_α. The collection of all isothermal coordinate charts forms a *conformal atlas* and the maximal conformal atlas is a *conformal structure*. If S admits a conformal structure, we call S a *Riemann surface*. Isothermal coordinates are considered in more detail in subsection 2.4.4.

2.4.2 Beltrami Differential

Next, we consider q.c. maps between two Riemann surfaces. Therefore, we need to generalize the (local) Beltrami coefficient to a global quantity on the entire surface X, which we call *Beltrami differential*. In particular, the Beltrami differential should be independent of the choice of the concrete local coordinates. According to Hubbard [2016], a Beltrami differential form on X is a bundle map $\mu : TX \to TX$, which is fiberwise antilinear and measurable with $\|\mu\|_\infty = \operatorname*{esssup}_{x \in X} |\mu(x)| < 1$. Fiberwise antilinear means that for each $p \in X$, $\mu_p : T_pX \to T_pX$ is an antilinear map, i.e. $\mu_p(v + w) = \mu_p(v) + \mu_p(w)$ (additivity) and $\mu_p(zv) = \bar{z}\mu_p(v)$ (conjugate homogeneity) for $v, w \in T_pX \cong \mathbb{C}$, $z \in \mathbb{C}$. This definition is too abstract for our purposes, so we give a concrete construction:

The Beltrami differential is the differential $\mu(z)\frac{\mathrm{d}\bar{z}}{\mathrm{d}z}$ constructed in the follwing way: Each chart (U_α, ϕ_α) is assigned a function $\mu_\alpha : \phi_\alpha(U_\alpha) \to \mathbb{C}, z_\alpha \mapsto \mu_\alpha(z_\alpha)$ with $\mu_\alpha \in L^\infty(\phi_\alpha(U_\alpha))$, such that

$$\mu_\alpha \frac{\mathrm{d}\bar{z}_\alpha}{\mathrm{d}\bar{z}_\beta} = \mu_\beta \frac{\mathrm{d}z_\alpha}{\mathrm{d}z_\beta} \tag{2.4.3}$$

holds on the part of the domain U_α, which is also covered by another chart (U_β, ϕ_β). z_α denotes the local coordinates on U_α, $\frac{\mathrm{d}z_\alpha}{\mathrm{d}z_\beta} = \frac{\mathrm{d}\phi_{\beta\alpha}}{\mathrm{d}z_\beta}$ and $\frac{\mathrm{d}\bar{z}_\alpha}{\mathrm{d}\bar{z}_\beta} = \frac{\mathrm{d}\bar{\phi}_{\beta\alpha}}{\mathrm{d}\bar{z}_\beta}$, where $\phi_{\beta\alpha}$ is the transition map from the chart (U_β, ϕ_β) to (U_α, ϕ_α). The set of all such functions μ_α forms the Beltrami differential. Equation 2.4.3 can be considered as a consistency condition on the overlapping regions of different charts, so that the definition of the Beltrami differential is well-defined. When the surface is covered by one single chart, the two notions coincide and we speak of a Beltrami coefficient instead of a Beltrami differential. A visualization can be found in figure 6.

We want to motivate the consistency condition in equation 2.4.3 following Zakeri: Let $z = x + iy$ be a holomorphic local coordinate on X. (x, y) can be interpreted as coordinates for the underlying smooth surface, in which the Riemannian metric g on X can be expressed locally as

$$g = E\mathrm{d}x^2 + 2F\mathrm{d}x\mathrm{d}y + G\mathrm{d}y^2, \tag{2.4.4}$$
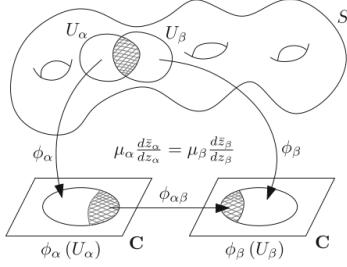
Figure 6: Beltrami differential, figure from Zeng et al. [2012]

where E, F, G are smooth functions of (x, y) with $E > 0, G > 0$ and $EG - F^2 > 0$. With this, the inner product on each tangent space can be expressed as

$$\left\langle a\frac{\partial}{\partial x} + b\frac{\partial}{\partial y}, c\frac{\partial}{\partial x} + d\frac{\partial}{\partial y} \right\rangle_g = Eac + F(ad + bc) + Gbd = \begin{bmatrix} a & b \end{bmatrix} L \begin{bmatrix} c \\ d \end{bmatrix} \tag{2.4.5}$$

with L as the matrix

$$\begin{bmatrix} E & F \\ F & G \end{bmatrix} \tag{2.4.6}$$

of g in the standard basis $\{\frac{\partial}{\partial x}, \frac{\partial}{\partial y}\}$. Similiar to open subsets of $\mathbb{C}$ in chapter 2.1, we can generalize the complex differential 1-forms $\mathrm{d}z$ and $\mathrm{d}\bar{z}$ to Riemann surfaces: $\mathrm{d}z$ and $\mathrm{d}\bar{z}$ on X can be defined as two local sections of the complexified cotangent bundle $T^*X \otimes \mathbb{C}$ by

$$\mathrm{d}z = \mathrm{d}x + \mathrm{i}\mathrm{d}y, \tag{2.4.7}$$

$$\mathrm{d}\bar{z} = \mathrm{d}x - \mathrm{i}\mathrm{d}y. \tag{2.4.8}$$

As for open subsets of $\mathbb{C}$, $\mathrm{d}z$ and $\mathrm{d}\bar{z}$ form a basis for each complexified cotangent space. The local sections of the complexified tangent bundle $TX \otimes \mathbb{C}$,

$$\frac{\partial}{\partial z} = \frac{1}{2}\left(\frac{\partial}{\partial x} - \mathrm{i}\frac{\partial}{\partial y}\right) \tag{2.4.9}$$

and

$$\frac{\partial}{\partial \bar{z}} = \frac{1}{2}\left(\frac{\partial}{\partial x} + \mathrm{i}\frac{\partial}{\partial y}\right), \tag{2.4.10}$$

form the corresponding dual basis at each point. The inner product defined by g can be uniquely extended to a Hermitian product on $TX \otimes \mathbb{C}$, which representation matrix in the basis $\{\frac{\partial}{\partial x}, \frac{\partial}{\partial y}\}$ is given by $L' = D^*LD$, with

$$D = \frac{1}{2}\begin{bmatrix} 1 & 1 \\ \mathrm{i} & -\mathrm{i} \end{bmatrix}. \tag{2.4.11}$$

The components of the matrix L' are then

$$L' = \frac{1}{4}\begin{bmatrix} E + G & E - G - 2\mathrm{i}F \\ E - G + 2\mathrm{i}F & E + G \end{bmatrix}. \tag{2.4.12}$$

If we introduce the quantities

$$\gamma^2 = \frac{1}{4}\left(E + G + \sqrt{EG - F^2}\right) \tag{2.4.13}$$

and

$$\mu = \frac{1}{4\gamma^2}(E - G + 2\mathrm{i}F) = \frac{E - G + 2\mathrm{i}F}{E + G + \sqrt{EG - F^2}}, \tag{2.4.14}$$

23

substituting these into L' gives

$$L' = \gamma^2 \begin{bmatrix} \frac{1+|\mu|^2}{2} & \overline{\mu} \\ \mu & \frac{1+|\mu|^2}{2} \end{bmatrix}. \tag{2.4.15}$$

Due to the properties of the functions E, F and G, e.g. $EG - F^2 > 0$, it holds

$$\gamma^2 > 0 \quad \text{and} \quad |\mu|^2 = \frac{E + G - 2\sqrt{EG - F^2}}{E + G + 2\sqrt{EG - F^2}} < 1. \tag{2.4.16}$$

Using L', the Hermitian product on $TX \otimes \mathbb{C}$ can be written as

$$\left\langle \alpha \frac{\partial}{\partial z} + \beta \frac{\partial}{\partial \overline{z}}, \omega \frac{\partial}{\partial z} + v \frac{\partial}{\partial \overline{z}} \right\rangle = \begin{bmatrix} \alpha & \beta \end{bmatrix} L' \begin{bmatrix} \overline{\omega} \\ \overline{v} \end{bmatrix}, \tag{2.4.17}$$

from which we obtain

$$\left\| \alpha \frac{\partial}{\partial z} + \beta \frac{\partial}{\partial \overline{z}} \right\|^2 = \gamma^2 \left(\frac{1 + |\mu|^2}{2} (|\alpha|^2 + |\beta|^2) + \mu \overline{\alpha} \beta + \overline{\mu} \alpha \overline{\beta} \right). \tag{2.4.18}$$

Since real tangent vectors have the special form $\alpha \frac{\partial}{\partial z} + \overline{\alpha} \frac{\partial}{\partial \overline{z}}$ (due to $a \frac{\partial}{\partial x} + b \frac{\partial}{\partial y} = (a + ib) \frac{\partial}{\partial z} + (a - ib) \frac{\partial}{\partial \overline{z}}$), the above formula reduces to

$$\left\| \alpha \frac{\partial}{\partial z} + \overline{\alpha} \frac{\partial}{\partial \overline{z}} \right\|^2 = \gamma^2 |\alpha + \mu \overline{\alpha}|^2. \tag{2.4.19}$$

Thus, as long as we care about lengths of real tangent vectors, g in the basis $\{\frac{\partial}{\partial z}, \frac{\partial}{\partial \overline{z}}\}$ can be represented as

$$g = \gamma(z)|dz + \mu(z)d\overline{z}|. \tag{2.4.20}$$

We want to understand the transformation behaviour of γ and μ under a holomorphic change of coordinates $z \mapsto w(z)$ on X:

$$\gamma(z) |dz + \mu(z)d\overline{z}| = w^*(\gamma(w) |dw + \mu(w)d\overline{w}|) \tag{2.4.21}$$

$$= \gamma(w(z)) |w'(z)dz + \mu(w(z))\overline{w'(z)}d\overline{z}| \tag{2.4.22}$$

$$= \gamma(w(z))|w'(z)| \left| dz + \mu(w(z))\frac{\overline{w'(z)}}{w'(z)}d\overline{z} \right|. \tag{2.4.23}$$

By comparison we finally obtain the consistency condition in equation 2.4.3:

$$\gamma(z) = \gamma(w(z))|w'(z)| \quad \Leftrightarrow \quad \gamma(z)|dz| = \gamma(w)|dw|, \tag{2.4.24}$$

$$\mu(z) = \mu(w(z))\frac{\overline{w'(z)}}{w'(z)} \quad \Leftrightarrow \quad \mu(z)\frac{d\overline{z}}{dz} = \mu(w)\frac{d\overline{w}}{dw}. \tag{2.4.25}$$

Equation 2.4.24 tells us that $\gamma(z)|dz|$ is a well-defined $(1, 1)$-differential, namely a conformal metric, on X. In the same way, the Beltrami differential $\mu(z)\frac{d\overline{z}}{dz}$ is a well-defined $(-1, 1)$-differential on X, as stated above. μ depends only on the conformal class $[g]$ and $z \mapsto |\mu(z)|$ is a well-defined function on X. As a corollary we obtain a one-to-one correspondence between conformal structures on X and Beltrami differentials $\mu = \mu(z)\frac{d\overline{z}}{dz}$ which satisfy $|\mu(z)| < 1$ in every local coordinate z on X. If the Beltrami differential vanishes, one obtains just the standard conformal structure $[g] = [dz]$.

The above derivation allows us to make the geometric interpretation of q.c. mappings more concrete than in chapter 2.1 We consider a conformal structure $[g]$ on X (or $U \subset \mathbb{C}$ in the planar case) and its associated Beltrami differential by equation 2.4.14. We consider a point $p \in X$, fix a local coordinate $z = x + iy$ around it and define the family of "circles" around p as

$$E(p) := \{v \in T_p X : \|v\| = \text{const.}\}. \tag{2.4.26}$$
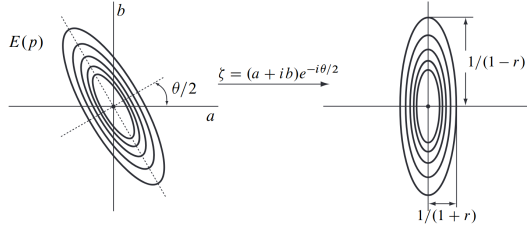
Figure 7: Geometric interpretation of the Beltrami differential as a field of ellipses on the tangent bundle TX, figure from Zakeri

$E(p)$ depends only on $[g]$. If we consider a real tangent vector $\boldsymbol{v} = a\frac{\partial}{\partial x} + b\frac{\partial}{\partial y} = (a+ib)\frac{\partial}{\partial z} + (a-ib)\frac{\partial}{\partial \bar{z}}$, then the "circles" $\|\boldsymbol{v}\| = $ const. correspond to loci $|(a+ib) + \mu(a-ib)| = $ const. in the real (a,b)-plane. By setting $\mu = re^{i\theta}$ and $\zeta = (a+ib)e^{-i\frac{\theta}{2}}$, we obtain the loci $|\zeta + r\bar{\zeta}| = $ const. in the ζ-plane, which is the family of concentric ellipses with minor axis along the real direction and major axis along the imaginary direction of the ζ-plane. The ratio of the major to minor axis is equal to $\frac{1+r}{1-r}$. If we transfer this family back to the (a,b)-plane, we see that $E(p)$ is a family of concentric ellipses in T_pX with

$$\varphi = \arg(\mu)/2 \tag{2.4.27}$$

as angle of elevation of the minor axis and

$$K = \frac{1+|\mu|}{1-|\mu|} \tag{2.4.28}$$

as ratio of the major to minor axis. A visualization can be found in figure 7. For the zero Beltrami differential, the cocentric ellipses become round cricles with $|\zeta|^2 = a^2 + b^2 = $ const. in the (a,b)-plane. Equation 2.4.28 coincides with the dilatation 2.1.14 introduced in chapter 2.1, if we assign a complex valued function f on X its Beltrami differential and derive the corresponding metric g from it. This will becomes clear in the following remark.

Remark: In the above derivation, μ was constructed from the local representation of the metric g. Conversely, one can also specify μ and assign a metric g to this μ in such a way that $[g] = [|dz + \mu(z)d\bar{z}|]$ then realizes μ. This is more natural for our use case, since $\mu = -g$ is in principle observable.

Summary: As seen in this subsection, we have at least four different ways to think of a Beltrami differential μ on a Riemann surface X:

1. As an abstract fiberwise antilinear bundle map $\mu : TX \to TX$, which is measurable with $\|\mu\|_\infty = \operatorname*{esssup}_{x \in X} |\mu(x)| < 1$.

2. As a $(-1, 1)$-differential 1-form on X obeying the transformation rule in equation 2.4.3.

3. As a conformal structure $[g] = [|dz + \mu(z)d\bar{z}|]$ on X.

4. As a field of cocentric ellipses on the real tangent bundle TX.

2.4.3 Quasi-Conformal Mappings

With the notion of a Beltrami differential a q.c. mapping between two Riemann surfaces S_1 and S_2 can be defined as follows (see figure 5 for the geometric illustration): A homeomorphism $f : S_1 \to S_2$ is called q.c. associated with the Beltrami differential $\mu\frac{d\bar{z}}{dz}$ if it is orientation preserving and the mapping $f_{\alpha\beta} := \psi_\beta \circ f \circ \phi_\alpha^{-1}$ is q.c. associated with $\mu_\alpha\frac{d\bar{z}_\alpha}{dz_\alpha}$. The process of finding the q.c. mapping corresponding to a given Beltrami differential is called solving Beltrami's equation.

We want to show that this definition is well-defined. Consider a region of S_1, which is covered by two different charts z_α and $z_{\alpha'}$. $\frac{dz_\alpha}{dz_{\alpha'}} = 0$ then yields

$$\mu_{\alpha'}(z_{\alpha'}) = \frac{\partial f_{\alpha'\beta}}{\partial \bar{z}_{\alpha'}} \bigg/ \frac{\partial f_{\alpha'\beta}}{\partial \bar{z}_{\alpha'}} = \left(\frac{\partial f_{\alpha\beta}}{\partial \bar{z}_\alpha} \frac{d\bar{z}_\alpha}{d\bar{z}_{\alpha'}} \right) \bigg/ \left(\frac{\partial f_{\alpha\beta}}{\partial z_\alpha} \frac{dz_\alpha}{dz_{\alpha'}} \right) = \mu_\alpha(z_\alpha) \frac{d\bar{z}_\alpha}{d\bar{z}_{\alpha'}} \bigg/ \frac{dz_\alpha}{dz_{\alpha'}}. \tag{2.4.29}$$

This is guaranteed by the consisteny condition of the Beltrami differential in equation 2.4.3. We also need to check that the definition is independent of the chosen chart in the range of f. Therefore, consider two different charts w_β and $w_{\beta'}$ on the range of f and let μ_β and $\mu_{\beta'}$ be the Beltrami coefficients computed under $f_{\alpha\beta}$ and $f_{\alpha\beta'}$, respectively. Due to the holomorphy of $w_{\beta'}$ we have $\frac{\partial w_{\beta'}}{\partial \overline{w}_\beta} = 0$, and thus

$$\mu_{\beta'}(z_\alpha) = \frac{\partial f_{\alpha\beta'}}{\partial \bar{z}_\alpha} \bigg/ \frac{\partial f_{\alpha\beta'}}{\partial \alpha} = \left(\frac{\partial w_{\beta'}}{\partial w_\beta} \frac{\partial f_{\alpha\beta}}{\partial \bar{z}_\alpha} + \frac{\partial w_{\beta'}}{\partial \overline{w}_\beta} \frac{\partial \overline{f}_{\alpha\beta}}{\partial \bar{z}_\alpha} \right) \bigg/ \left(\frac{\partial w_{\beta'}}{\partial w_\beta} \frac{\partial f_{\alpha\beta}}{\partial z_\alpha} + \frac{\partial w_{\beta'}}{\partial \overline{w}_\beta} \frac{\partial \overline{f}_{\alpha\beta}}{\partial z_\alpha} \right) = \frac{\partial f_{\alpha\beta}}{\partial \bar{z}_\alpha} \bigg/ \frac{\partial f_{\alpha\beta}}{\partial z_\alpha} = \mu_\beta(z_\alpha). \tag{2.4.30}$$

Analogous to the planar case, many properties of q.c. mappings between domains in $\mathbb{C}$ can also be shown for q.c. mappings between Riemann surfaces, such as the chain rule. We do not want to go into this further and instead refer to Zeng et al. [2012] and Zakeri.

2.4.4 Isothermal Coordinates

Definition: Isothermal coordinates on an arbitrary Riemannian manifold are local coordinates where the metric is conformal to the standard Euclidean metric, i.e.

$$ds^2 = \lambda(u_1, \ldots, u_n)(du_1^2 + \ldots + du_n^2), \tag{2.4.31}$$

for some smooth function $\lambda > 0$. For weak lensing only (curved) surfaces S embedded in $\mathbb{R}^3$ are relevant. In this case equation 2.4.31 takes the form

$$ds^2 = \lambda(u_1, u_2)(du_1^2 + du_2^2) \tag{2.4.32}$$

with isothermal coordinates (u_1, u_2). Being conformal to the standard Euclidean metric means that the curves of constant u_1 intersect the curves of constant u_2 transversely and form infinitesimal perfect squares. In isothermal coordinates, the Gauss curvature can be simply derived from the function λ as

$$K(u_1, u_2) = -\frac{1}{\lambda(u_1, u_2)} \Delta \ln(\lambda), \tag{2.4.33}$$

with the Laplace operator

$$\Delta = \frac{\partial^2}{\partial u_1^2} + \frac{\partial^2}{\partial u_2^2}. \tag{2.4.34}$$

As pointed out by Hofmann-Wellenhof [1995] the concept of isothermal coordinates originates from thermodynamics: If there is a stationary heat flow on a surface of homogeneous material, the lines of equal temperature (isotherms) together with the corresponding orthogonal trajectories (streamlines) form an isothermal grid.

Existence: As proven first by Korn [1914] and Lichtenstein [1916] isothermal coordinates exist around any point on a two dimensional Riemannian manifold S, in particular on every Riemann surface. The existence of isothermal coordinates is strongly related to the existence of solutions of the Beltrami equation: We know from subsection 2.4.2 about the Beltrami differential, that if the Riemannian metric g on S is locally given by the first fundamental form

$$ds^2 = E dx^2 + 2F dx dy + G dy^2, \tag{2.4.35}$$

using complex coordinates it can be written as

$$\mathrm{d}s^2 = \gamma^2|\mathrm{d}z + \mu\mathrm{d}\bar{z}|^2, \tag{2.4.36}$$

with γ and μ defined in equation 2.4.24 and 2.4.25 respectively. In isothermal coordinates (u_1, u_2) the line element can be expressed as

$$\mathrm{d}s^2 = \lambda(\mathrm{d}u_1^2 + \mathrm{d}u_2^2). \tag{2.4.37}$$

Introducing the complex coordinate $w := u_1 + iu_2$ yields

$$\mathrm{d}s^2 = \lambda|\mathrm{d}w|^2 = \lambda|w_z|^2\left|\mathrm{d}z + \frac{w_{\bar{z}}}{w_z}\mathrm{d}\bar{z}\right|^2. \tag{2.4.38}$$

By comparing equation 2.4.36 with 2.4.38 we see that (u_1, u_2) will be isothermal if the Beltrami equation

$$w_{\bar{z}} = \mu w_z \tag{2.4.39}$$

has a diffeomorphic solution. This is always the case, as shown in Ahlfors [2006]. Alternatively, the existence of isothermal coordinates can be shown by direct elementary methods, as in Chern [1955] and Jost [2006].

Example: We want to give a prominent example of isothermal coordinates: The stereograpic mapping (projection). It is constructed in the following way: Let the unit sphere $\mathbb{S}^2$ be centered at the origin as shown in figure 8.
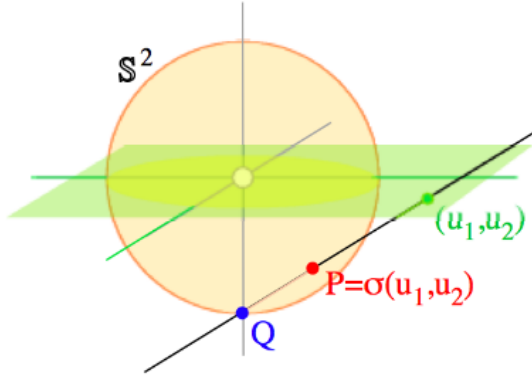

Figure 8: Stereographic mapping (projection): A point $P = \sigma(u_1, u_2)$ is parametrized by the two coordinates $(u_1, u_2) \in \mathbb{R}^2$, figure from Treibergs [2010]

Imagine a straight line through the south pole Q and some other point $P \in \mathbb{S}^2$. The line crosses the $z = 0$ plane at the point $(u_1 \quad u_2 \quad 0)$. Thus, we are able to express P in terms of the two coordinates (u_1, u_2). The mapping $\sigma : U = \mathbb{R}^2 \to \mathbb{S}^2 \setminus \{Q\}$ is the inverse of a coordinate chart for $\mathbb{S}^2$ called stereographic coordinates. It is defined by

$$\sigma(u_1, u_2) = \left(\frac{2u_1}{1+u_1^2+u_2^2}, \quad \frac{2u_2}{1+u_1^2+u_2^2}, \quad \frac{1-u_1^1-u_2^2}{1+u_1^1+u_2^2}\right). \tag{2.4.40}$$

To show that stereographic coordinates are isothermal, we calculate the tangent vectors for the stereographic mapping:

$$X_1 = \left(\frac{2-2u_1^2}{(1+u_1^2+u_2^2)^2}, \quad -\frac{4u_1u_2}{(1+u_1^1+u_2^2)^2}, \quad -\frac{4u_1}{(1+u_1^2+u_2^2)^2}\right), \tag{2.4.41}$$

$$X_2 = \left(-\frac{4u_1u_2}{(1+u_1^2+u_2^2)^2}, \quad \frac{2+2u_1^2-2u_2^2}{(1+u_1^1+u_2^2)^2}, \quad -\frac{4u_2}{(1+u_1^2+u_2^2)^2}\right). \tag{2.4.42}$$

27

Since
$$X_1 \cdot X_2 = 0, \tag{2.4.43}$$
(u_1, u_2) are isothermal coordinates. As a direct consequence we can compute the Gauss curvature K of $\mathbb{S}^2$. Due to
$$\lambda(u_1, u_2) = \sqrt{X_1 \cdot X_1} = \sqrt{X_2 \cdot X_2} = \frac{2}{1 + u_1^2 + u_2^2} \tag{2.4.44}$$
we obtain
$$K = -\frac{1}{\lambda^2} \Delta \ln(\lambda) = 1, \tag{2.4.45}$$
as expected.

2.4.5 Measurable Riemann Mapping Theorem

The measurable Riemann mapping theorem is crucial for the whole theory of q.c. mappings. Therefore, it is often considered as fundamental theorem of q.c. geometry. Rougly speaking it states that on the Riemann number sphere the solutions of the Beltrami equation are exactly the q.c. mappings. It should not be confused with the Riemann mapping theorem, which gives a characterization of simply connected domains of $\mathbb{C}$:

Riemann Mapping Theorem: Every simply connected open subset U of $\mathbb{C}$ ($U \notin \{\emptyset, \mathbb{C}\}$) is conformally equivalent to the open unit disk $\mathbb{D}$. That means, there exists a biholomorphic mapping between U and $\mathbb{D}$.

The (Poincaré) uniformization theorem generalizes the Riemann mapping theorem from simply connected open subsets of the complex plane to arbitrary simply connected Riemann surfaces:

Uniformization Theorem: Every simply connected Riemann surface is conformally equivalent to the open unit disk, the complex plane, or the Riemann sphere. The importance of this statement comes from the fact that every Riemann surface has an universal cover that is simply connected. Riemann surfaces can therefore be divided into three types: Elliptic surfaces, which have the Riemann number sphere as universal covering space, hyperbolic surfaces, which have the unit disk as universal covering space, and parabolic surfaces, which have the complex plane as universal covering space. Furthermore, the uniformization theorem allows us to establish a connection between Riemann surfaces and Riemannian geometry: As a corollary of it one can show that every Riemann surface admits a Riemannian metric of constant curvature, which is equals 1 in the elliptic, 0 in the parabolic and -1 in the hyperbolic case. In particular, let (S, g) be a compact 2-dimensional Riemannian manifold. Then there exists a metric $\tilde{g} = e^{2\lambda} g$ conformal to g, which has constant Gauss curvature.

Measurable Riemann Mapping Theorem (MRMT): Let μ be a measurable Beltrami form on the Riemann sphere $\hat{\mathbb{C}}$ with $\|\mu\|_\infty = k < 1$. Then

1. there exists a unique q.c. homeomorphism $f : \hat{\mathbb{C}} \to \hat{\mathbb{C}}$ which fixes $0, 1, \infty$ and solves the Beltrami equation $f_{\bar{z}} = \mu f_z$.

2. f is a C^∞ diffeomorphism if μ is C^∞.

As corollary of the MRMT we obtain the mapping theorem, which was stated already in subsection 2.3.2 as a consequence of the uniqueness theorem for planar q.c. mappings:

Mapping Theorem or MRMT, Disk Case: Let μ be a measurable complex-valued function on the unit disk $\mathbb{D}$ with $\|\mu\|_\infty = k < 1$. Then there exists a q.c. homeomorphism $f : \mathbb{D} \to \mathbb{D}$ which satisfies the Beltrami equation $f_{\bar{z}} = \mu f_z$ almost everywhere. f is unique up to compositions with conformal automorphisms of $\mathbb{D}$.

Using the MRMT we will proof this statement: First, we extend μ to $\hat{\mathbb{C}}$ by setting $\mu(z) = 0$ for $|z| > 1$. With that we are able to apply the MRMT, and the restriction to $\mathbb{D}$ of the normalized solution given by the MRMT will provide a q.c. solution $h : \mathbb{D} \to h(\mathbb{D})$ of the Beltrami equation. Since $\mathbb{C}$ and $\mathbb{D}$ are not quasi-conformally homeomorphic, $h(\mathbb{D}) \neq \mathbb{C}$. Thus, by the Riemann mapping theorem there exists a conformal map $g : h(\mathbb{D}) \to \mathbb{D}$. The composition $f = g \circ h$ will then be the required map. It is also possible to formulate the MRMT for Riemann surfaces:

MRMT, Riemann Surface Case: Let μ be a measurable Beltrami form with bounded dilatation on a Riemann surface X. Then there exists a Riemann surface Y and a q.c. homeomorphism $f : X \to Y$ such that $f_{\bar{z}} = \mu f_z$. If $g : X \to Z$ is another such homeomorphism, the map $g \circ f^{-1} : Y \to Z$ is biholomorphic.

2.5 Computational Quasi-Conformal Mappings between Riemann Surfaces

The field of computational q.c. geometry is quite young, but has gained increasing popularity in recent years, in particular from applied mathematics, computer vision and medical imaging. That may be the reason why this is the first work considering its applications to weak lensing.

The field extends the q.c. theory into a discrete setting and develops algorithms for computing q.c. mappings associated with a given Beltrami differential between Riemann surfaces. In general, the chosen algorithm depends mainly on the topology of the surfaces. However, they all have in common that in order to solve the Beltrami equation on Riemann surfaces, we simply need to define a new auxiliary metric associated with the prescribed Beltrami differential. With the auxiliary metric, the q.c. mapping is equivalent to a conformal mapping associated with the newly defined metric. Thus, solving the Beltrami equation can be reduced via an auxiliary metric to the computation of a conformal mapping, for which well-known algorithms exist. This is the main theorem of Zeng et al. [2012], which we want to reproduce here together with its proof.

Auxiliary Metric Associated with a Beltrami Differential: Let (S_1, g_1), (S_2, g_2) be two Riemann surfaces and $f : S_1 \to S_2$ be a q.c. mapping associated with the Beltrami differential $\mu \frac{\mathrm{d}\bar{z}}{\mathrm{d}z}$. We denote with z and w the local isothermal coordinates of S_1 and S_2 respectively. As seen in subsection 2.4.4, such coordinates exists around any point of S_1 and S_2 respectively. Motivated by $g_1 = e^{2\lambda_1(z)}\mathrm{d}z\mathrm{d}\bar{z}$ and $g_2 = e^{2\lambda_2(w)}\mathrm{d}w\mathrm{d}\overline{w}$ we define an auxiliary Riemannian metric on S_1 by

$$\tilde{g}_1 = e^{2\lambda_1(z)}|\mathrm{d}z + \mu\mathrm{d}\bar{z}|^2. \tag{2.5.1}$$

Then, the auxiliary metric is well-defined and the mapping $f : (S_1, \tilde{g}_1) \to (S_2, g_2)$ is conformal.

We start with the proof of the first part of the statement by considering a region which is covered by two different charts z_α and z_β. As seen, g_1 can be local represented under z_α as $e^{2\lambda_\alpha(z)}\mathrm{d}z_\alpha\mathrm{d}\bar{z}_\alpha$ and under z_β as $e^{2\lambda_\beta(z)}\mathrm{d}z_\beta\mathrm{d}\bar{z}_\beta$. Due to $\frac{\mathrm{d}z_\alpha}{\mathrm{d}\bar{z}_\beta} = 0$, we have

$$\mathrm{d}z_\alpha = \frac{\mathrm{d}z_\alpha}{\mathrm{d}z_\beta}\mathrm{d}z_\beta + \frac{\mathrm{d}z_\alpha}{\mathrm{d}\bar{z}_\beta}\mathrm{d}\bar{z}_\beta = \frac{\mathrm{d}z_\alpha}{\mathrm{d}z_\beta}\mathrm{d}z_\beta, \tag{2.5.2}$$

and

$$e^{2\lambda_\alpha(z_\alpha)}\mathrm{d}z_\alpha\mathrm{d}\bar{z}_\alpha = e^{2\lambda_\alpha(z_\alpha)}|\mathrm{d}z_\alpha|^2 = e^{2\lambda_\alpha(z_\alpha)}\left|\frac{\mathrm{d}z_\alpha}{\mathrm{d}z_\beta}\right|^2|\mathrm{d}z_\beta|^2 = e^{2\lambda_\beta(z_\beta)}\mathrm{d}z_\beta\mathrm{d}\bar{z}_\beta. \tag{2.5.3}$$

This gives us the relation

$$e^{2\lambda_\beta(z_\beta)} = e^{2\lambda_\alpha(z_\alpha)}\left|\frac{\mathrm{d}z_\alpha}{\mathrm{d}z_\beta}\right|^2. \tag{2.5.4}$$

Together with the consisteny condition of the Beltrami differential we obtain

$$e^{2\lambda_\alpha(z_\alpha)}|\mathrm{d}z_\alpha + \mu_\alpha\mathrm{d}\bar{z}_\alpha|^2 = e^{2\lambda_\alpha(z_\alpha)}\left|\frac{\mathrm{d}z_\alpha}{\mathrm{d}z_\beta}\mathrm{d}z_\beta + \mu_\alpha\frac{\mathrm{d}\bar{z}_\alpha}{\mathrm{d}\bar{z}_\beta}\mathrm{d}\bar{z}_\beta\right|^2$$

$$= e^{2\lambda_\alpha(z_\alpha)} \left| \frac{\mathrm{d}z_\alpha}{\mathrm{d}z_\beta} \right|^2 \left| \mathrm{d}z_\beta + \mu_\alpha \frac{\mathrm{d}\overline{z}_\alpha}{\mathrm{d}\overline{z}_\beta} \middle/ \frac{\mathrm{d}z_\alpha}{\mathrm{d}z_\beta} \mathrm{d}\overline{z}_\beta \right|^2$$

$$= e^{2\lambda_\beta(z_\beta)} |\mathrm{d}z_\beta + \mu_\beta \mathrm{d}\overline{z}_\beta|^2. \tag{2.5.5}$$

To show that the mapping $f : (S_1, g_1) \to (S_2, g_2)$ is conformal, let f^*g_2 denote the pullback metric defined by

$$f^*g_2 = e^{2\lambda_2(f(z))} |\mathrm{d}f(z)|^2. \tag{2.5.6}$$

Due to

$$\mathrm{d}f(z) = \frac{\partial f(z)}{\partial z} \mathrm{d}z + \frac{\partial f(z)}{\partial \overline{z}} = \frac{\partial f(z)}{\partial z}(\mathrm{d}z + \mu \mathrm{d}\overline{z}) \tag{2.5.7}$$

it holds

$$f^*g_2 = e^{2\lambda_2(f(z))} \left| \frac{\partial f(z)}{\partial z} \right|^2 |\mathrm{d}z + \mu \mathrm{d}\overline{z}|^2. \tag{2.5.8}$$

Using the definition of $\tilde{g}_1$ we can express f^*g_2 as

$$f^*g_2 = e^{2\lambda_2(f(z))-2\lambda_1(z)} \left| \frac{\partial f(z)}{\partial z} \right|^2 \tilde{g}_1. \tag{2.5.9}$$

This means that f^*g_2 is conformal to $\tilde{g}_1$. Since $f : (S_1, f^*g_2) \to (S_2, g_2)$ is isometric, $f : (S_1, \tilde{g}_1) \to (S_2, g_2)$ is conformal.

Since the focus of this work lies on planar fields, we do not want to go into further detail about computational quasi-conformal geometry. For an overview of the most important notions of the field like the discrete Beltrami differential we refer to Zeng et al. [2012], and for concrete algorithms for the computation of conformal mappings to Gu and Yau [2008].

3 Methodology

Using our results from chapter 2 we first derive a new algorithm for delensing of planar fields by solving the Beltrami equation via a finite element approach. After that we shortly discuss further approaches for a delensing algorithm for the planar case, coming from image registration tasks and q.c. mappings for medical imaging. In the second part of this chapter we want to give an outlook to the general (curved) case, i.e. where the plane sky approximation for weak lensing is no longer valid, and we need more elaborate algorithms for delensing. After a short review of such an algorithm developed by the DES Collaboration et al. [2018] using spin-weighted spherical harmonics, we give some ideas how we could generalize our algorithm for the planar case to areas of the celestical sphere modelled as Riemann surfaces. This is especially relevant for weak lensing of the CMB. For that, we use the notion of a Beltrami differential as introduced in chapter 2.4.2.

3.1 Proposed Inversion Algorithm for Planar Fields

We have seen in chapter 2 that for planar domains the complexified lens mapping f can be considered as q.c. mapping with Beltrami coefficient μ given by the negative of the reduced shear g. The Beltrami equation is reduced to two elliptic PDEs for the real and imaginary part of the complexified lens mapping, which are then solved via a finite element approach. From the deflection field one can obtain the convergence and shear by a simple derivation. Algorithm 1 sketches our proposed algorithm. The individual steps of the algorithm along with derivations of the used formulas are explained in more detail below. In this context also a review of the finite element method (FEM) and the concrete implementation of our algorithm is provided.

Algorithm 1 Proposed inversion algorithm for planar fields

    Input: planar domain Ω; map of the reduced shear g (in principle observable); boundary conditions for real and imaginary part of the lens mapping f (Dirichlet, Neumann or mixed)

    Output: lens mapping f (or deflection field α); map of convergence κ and shear γ

1: $\mu(z) = -g(z) \quad \forall z \in \Omega$

2: Compute $\alpha_1 = \frac{(\rho-1)^2+\tau^2}{1-\rho^2-\tau^2}$; $\alpha_2 = -\frac{2\tau}{1-\rho^2-\tau^2}$; $\alpha_3 = \frac{(1+\rho)^2+\tau^2}{1-\rho^2-\tau^2}$ $\forall z \in \Omega$ where $\mu(z) = \rho(z) + \mathrm{i}\tau(z)$

3: Define the positive definite matrices $A(z) := \begin{pmatrix} \alpha_1(z) & \alpha_2(z) \\ \alpha_2(z) & \alpha_3(z) \end{pmatrix}$ $\forall z \in \Omega$

4: **for** $w \in \{u = \mathrm{Re}(f), v = \mathrm{Im}(f)\}$ **do**

5:      Solve the elliptic PDE $-\mathrm{div}(A\nabla w) = 0$ on Ω using a finite element approach (see below)

6: **end for**

7: $\kappa = \frac{1}{2}(u_x + v_y)$; $\gamma_1 = \frac{1}{2}(u_x - v_y)$ and $\gamma_2 = \frac{1}{2}u_y$

3.1.1 Solving the Beltrami Equation by Reduction to Elliptic PDEs

Following Lui et al. [2013b], the Beltrami equation in 2.1.8 can be reduced to two elliptic PDEs for the real and imaginary part of f with coefficients determined by the Beltrami coefficient field μ, which is just the negative of the reduced shear for our algorithm. By decomposing $\mu = \mathrm{Re}(\mu) + \mathrm{iIm}(\mu) = \rho + \mathrm{i}\tau$ and $f = \mathrm{Re}(f) + \mathrm{iIm}(f) = u + \mathrm{i}v$ we can rewrite the Beltrami coefficient in terms of x and y derivatives of u and v:

$$\mu = \rho + \mathrm{i}\tau = \frac{(v_x - v_y) + \mathrm{i}(v_x + u_y)}{(u_x + v_y) + \mathrm{i}(v_x - u_y)}. \tag{3.1.1}$$

After some simple calculations one finds out that v_x and v_y can be expressed as linear combinations of u_x and u_y:

$$-v_x = \alpha_1 u_x + \alpha_2 u_y \tag{3.1.2}$$

$$v_y = \alpha_2 u_x + \alpha_3 u_y \tag{3.1.3}$$

with

$$\alpha_1 = \frac{(\rho - 1)^2 + \tau^2}{1 - \rho^2 - \tau^2}; \quad \alpha_2 = -\frac{2\tau}{1 - \rho^2 - \tau^2}; \quad \alpha_3 = \frac{(1 + \rho)^2 + \tau^2}{1 - \rho^2 - \tau^2}. \tag{3.1.4}$$

On the other hand:

$$u_y = \alpha_1 v_x + \alpha_2 v_y \tag{3.1.5}$$

$$-u_x = \alpha_2 v_x + \alpha_3 v_y. \tag{3.1.6}$$

Due to the symmetry of the second derivatives it holds

$$\nabla \cdot \begin{pmatrix} -v_y \\ v_x \end{pmatrix} = 0 \quad \text{and} \quad \nabla \cdot \begin{pmatrix} u_y \\ -u_x \end{pmatrix} = 0. \tag{3.1.7}$$

By substituting equation 3.1.2 and 3.1.3 into 3.1.7 we obtain two elliptic PDEs for u and v

$$\nabla \cdot \left(A \begin{pmatrix} u_x \\ u_y \end{pmatrix} \right) = 0 \text{ and } \nabla \cdot \left(A \begin{pmatrix} v_x \\ v_y \end{pmatrix} \right) = 0, \tag{3.1.8}$$

where the symmetric, positive definite matrix A is given by

$$A = \begin{pmatrix} \alpha_1 & \alpha_2 \\ \alpha_2 & \alpha_3 \end{pmatrix}. \tag{3.1.9}$$

The positive definitness can be shown by calculating the two eigenvalues λ_1 and λ_2 of A:

$$\lambda_1 = (1 - |\mu|)^2 \tag{3.1.10}$$

$$\lambda_2 = (1 + |\mu|)^2, \tag{3.1.11}$$

which are strictly greater than 0, since $|\mu| \leq k < 1$. Here we have not considered the prefactor $1/(1 - |\mu|^2)$ of A, since it is always strictly greater than 0 due to the same reasoning. We keep in mind that equation 3.1.8 is written out as follows

$$-\text{div}(A\nabla u) = -\sum_{i=1}^{2} \partial_i (A\nabla u)_i = -\sum_{i,k=1}^{2} a_{ik} \partial_{ik} u - \sum_{k=1}^{2} \left(\sum_{i=1}^{2} \partial_i a_{ik} \right) \partial_k u = -\sum_{i,k=1}^{2} a_{ik} \partial_{ik} u, \tag{3.1.12}$$

since a_{ij} respectively α_1, α_2 and α_3 do not explicitly depend on x or y. With that we can define the follwing linear elliptic differential operators:

$$Lu := -\sum_{i,k=1}^{2} a_{ik} \partial_{i,k} u, \tag{3.1.13}$$

$$Lv := -\sum_{i,k=1}^{2} a_{ik} \partial_{i,k} v. \tag{3.1.14}$$

From here, several options come into question to continue: On the one hand, depending on μ respectively g, analytical properties of the two differential operators can be considered (e.g. maximum principle). Also depending on the regularity of g we can make statements about the regularity of the lens mapping (e.g. interior regularity). On the other hand, the second derivatives of u and v, respectively, can be related to the flexion fields $\mathcal{F}$ and $\mathcal{G}$ and thus also to the reduced shear g. This will be subject of future work.

In the following, we restrict ourselves instead to solving the two equations in 3.1.8 numerically by means of the Finite Element Method (FEM). It is assumed that the reader is familiar with the basic concepts of FEM and Sobolev spaces. However, the upcoming subsection is largely self-containing.

3.1.2 Solving the Arising Elliptic PDEs using Finite Elements

As we have seen in the previous subsection, finding the lens mapping f from the reduced shear g as Beltrami coefficient field results in two separate problems for the real part u and imaginary part v of f. In the following, we can therefore restrict ourselves to the numerical solution of u. The solution of v then results analogously, with the only exception of different boundary values as for u.

Variational Formulation: For the sake of completeness, we give the classical formulation of problem 3.1.12: Find $u \in C^2(\Omega) \cap C^1(\overline{\Omega})$ such that

$$-\nabla \cdot (A\nabla u(z)) = 0, \; z \in \Omega \tag{3.1.15}$$

$$u(z) = g(z), \; z \in \Gamma_D \tag{3.1.16}$$

$$\boldsymbol{n} \cdot A\nabla u(z) = h(z), \; z \in \Gamma_N, \tag{3.1.17}$$

where $\partial\Omega = \Gamma_D \cup \Gamma_N$ and $\Gamma_D \cap \Gamma_N = \emptyset$ (*mixed boundary problem*). When $g \equiv 0$, $A = I$ and we obtain $-\nabla \cdot (A\nabla u) = -\Delta u$ and $\boldsymbol{n} \cdot A\nabla u = \frac{\partial u}{\partial n}$. This is just the well-known result that real and imaginary part are harmonic functions if f is conformal. Alternatively, we could also specify *Robin boundary conditions*

$$au(z) + b\boldsymbol{n} \cdot A\nabla u(z) = r(z), \; z \in \partial\Omega \tag{3.1.18}$$

for some non-zero constants a and b and a given function r on $\partial\Omega$: Second order elliptic PDEs require exactly one boundary condition at each boundary point so that the boundary value problem is well-posed.

The regularity requirements for u are often too strong and on the other hand the classical formulation is unsuitable for many approximation methods. We therefore are going to derive the weak formulation of problem 3.1.15 - 3.1.17. Multiplication of equation 3.1.15 by a test function $w \in C^\infty(\overline{\Omega})$ with $w(z) = 0$ for $z \in \Gamma_D$ and integration over Ω gives us:

$$-\int_\Omega \left(\sum_{i=1}^2 \partial_i (A\nabla u)_i \right) w \mathrm{d}z = 0. \tag{3.1.19}$$

Integration by parts using the divergence theorem for $d = 2$ then yields

$$\int_\Omega \sum_{i=1}^2 (A\nabla u)_i \partial_i w \mathrm{d}z - \int_{\Gamma_D} \left(\sum_{i=1}^2 (A\nabla u)_i n_i \right) w \mathrm{d}\sigma - \int_{\Gamma_N} \left(\sum_{i=1}^2 (A\nabla u)_i n_i \right) w \mathrm{d}\sigma = 0. \tag{3.1.20}$$

Using $\boldsymbol{n} \cdot A\nabla u = h$ on Γ_N and $w = 0$ on Γ_D we finally obtain:

$$\int_\Omega A\nabla u \cdot \nabla w \, \mathrm{d}z = \int_{\Gamma_N} hw \, \mathrm{d}\sigma. \tag{3.1.21}$$

Final Variational Formulation: As usual for FEM we use the derived relation in equation 3.1.21 to assign to our differential operator Lu a bilinear form $a(u, w)$ and solve the variational problem in suitable Hilbert spaces, namely in $H^1(\Omega) = W^{1,2}(\Omega)$, instead of $C^2(\Omega)$ as needed for a classical solution. Find $u \in H^1(\Omega)$ with $u|_{\Gamma_D} = g$ such that

$$a(u, w) := \int_\Omega A\nabla u \cdot \nabla w \, \mathrm{d}z = \int_{\Gamma_N} hw \, \mathrm{d}\sigma. := I(w) \tag{3.1.22}$$

for all $w \in H_0^1(\Omega) = \{w \in H^1(\Omega) : w_{\Gamma_D} = 0\}$ defines then a continuous variational formulation for the classical problem formulated in 3.1.15 - 3.1.17. The reason why the variational formulation in 3.1.22 is well-defined lies in an existence theorem for the Dirichlet and a trace theorem for the Neumann boundary problem Braess [2013]. Put simply, well-definedness in variational problems follows in general always from Lax-Milgram's theorem.

Finite Element Space V_h**:** Since $H^1(\Omega)$ has infinite dimension, one has to determine the minimum of the functional corresponding to the variational formulation in 3.1.22

$$J(w) := \frac{1}{2}a(w, w) - \langle l, w \rangle \to \min_{V_h}! \qquad (3.1.23)$$

not in $H_1(\Omega)$ respectively $H_0^1(\Omega)$, but instead in a suitable finite-dimensional subspace V_h of $H^1(\Omega)$. Using V_h we can give the discrete variational formulation of 3.1.22: Find $u_h \in V_h \subset H^1(\Omega)$ with $u_h|_{\Gamma_D} = g$ such that

$$a(u_h, w_h) = I(w_h), \qquad (3.1.24)$$

for all $w_h \in V_h$. V_h is also called *finite element space*. Let $\mathcal{T}_h$ be a *triangulation* of the domain Ω, i.e. a decomposition of Ω into a finite number of simplices K (e.g. triangles in the planar case which we are interested in) such that

$$\overline{\Omega} = \bigcup_{K \in \mathcal{T}_k} \overline{K}, \qquad (3.1.25)$$

and

$$K \cap K^{'} = \emptyset \text{ for } K \neq K^{'}. \qquad (3.1.26)$$

The set $\{m_1, \ldots, m_N\}$ contains all vertices of the triangles. Furthermore, we denote with $h := \max\limits_{K \in \mathcal{T}_h} \text{diam}(K)$ the *fineness* or *mesh width* of the triangulation $\mathcal{T}_h$. Figure 9 shows a triangulation with $h = 1/\sqrt{8}$ for a unit square.
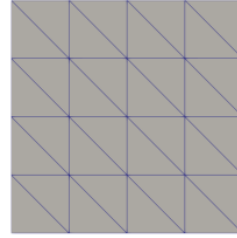
Figure 9: Triangulation of a unit square with $h = 1/\sqrt{8}$

For the new inversion algorithm we use the finite element space of piecewise linear functions

$$V_h := \{v : \overline{\Omega} \to \mathbb{R}, \ v|_K(x, y) = a_K + b_K x + c_K y \text{ for all } K \in \mathcal{T}_h\} = \text{span}[\phi_1, \ldots, \phi_N], \qquad (3.1.27)$$

where the basis functions ϕ_i have local support (cf. figure 10):

$$\phi_i : \Omega \to \mathbb{R}, \ \phi_i(m_j) = \delta_{ij}. \qquad (3.1.28)$$

The dimension of V_h is just the number of vertices in the current triangulation and is known as the number of degrees of freedom (DoFs, see Ciarlet [2002] for further details).
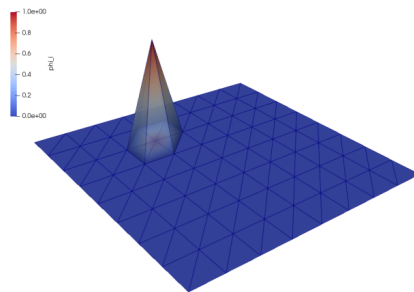

Figure 10: Example of a basis function with compact support on a square domain

Discrete Equations: Each function $u_h \in V_h$ can be represented in the ϕ_i-basis as:

$$u_h(z) = \sum_{i=1}^{N} u_i \phi_i(z); \quad U := (u_1, \ldots, u_N) \in \mathbb{R}^N. \tag{3.1.29}$$

By substituting this basis representation into the discrete variational formulation 3.1.24 we obtain the linear system

$$MU = b \tag{3.1.30}$$

with the so called *stiffness matrix* $M \in \mathbb{R}^{N \times N}$ and right hand side vector $b \in \mathbb{R}^N$:

$$M_{ij} = a(\phi_j, \phi_i); \quad b_i = I(\phi_i). \tag{3.1.31}$$

In our experiments we consider both Dirichlet and Neumann boundary problems. We first focus on the implementation of Dirichlet boundary values in the linear system in equation 3.1.30: Let

$$\mathcal{I}_D := \{i \in \{1, \ldots, N\} : m_i \in \Gamma_D\} \tag{3.1.32}$$

denote the Dirichlet boundary DoFs. For each $i \in \mathcal{I}_D$ set:

$$M_i = e_i = (0, \ldots, 0, 1, 0, \ldots, 0); \quad b_i = g(m_i). \tag{3.1.33}$$

For Neumann boundary conditions we do not need to change anything: They are imposed by the variational formulation automatically, which is the reason to call them natural boundary conditions.

Final Discrete Solution: Formally, by inverting M we obtain a solution of the linear system in 3.1.30:

$$\widetilde{U} \approx M^{-1} b. \tag{3.1.34}$$

Depending on the mesh size h, M can have many entries (up to $O(10^6)$). In general, one uses iterative solvers that compute a solution step by step and improve it as the number of iterations increases. Well-known iterative solvers are especially the Jacobi and Gauss-Seidel method. However, in practice one rather uses preconditioned Krylov subspace methods, such as CG or GMRES, and for parallel computing multigrid methods. In the implementation of our inversion algorithm we used CG. With $\widetilde{U}$ we finally get the solution of the real part of the lens mapping by a linear combination

$$\widetilde{u}_h(z) = \sum_{j=1}^{N} \widetilde{u}_j \phi_j(z), \tag{3.1.35}$$

and if we set

$$\widetilde{u}_i = g(m_i) \tag{3.1.36}$$

for each Dirichlet DoF $i \in \mathcal{I}_D$.

Basic Funtional Analytic Properties of the Form a**:** For the latter a priori error estimation, we need a brief resumee of the properties of the bilinear form a in equation 3.1.37:

$$a : H^1(\Omega) \times H^1(\Omega) \to \mathbb{R}, \; a(u, w) = \int_{\Omega} A \nabla u \cdot \nabla w \, \mathrm{d}z \tag{3.1.37}$$

a is *uniformly elliptic*, i.e. there exists $\alpha > 0$ such that

$$\xi^T A(z) \xi \geq \alpha \|\xi\|^2 \tag{3.1.38}$$

for all $\xi \in \mathbb{R}^2$, $z \in \Omega$, since the matrix A in equation 3.1.9 is symmetric positive definite: It holds $\langle A\xi, \xi \rangle = r(x) > 0$ for all $\xi \in \mathbb{R}^2$ and a continuous function r. If we restrict r on the compact set S^1 the

restriction has a mimimum which we denote with β ($\beta > 0$). Then it holds $\left\langle A\frac{\xi}{\|\xi\|}, \frac{\xi}{\|\xi\|}\right\rangle = r(\xi/\|\xi\|) \geq \beta$ for every $\xi \in \mathbb{R}^2$ and thus equation 3.1.38 is fullfilled.

Furthermore, a is *coercive* (or $H^1(\Omega)$-elliptic), i.e.

$$a(w, w) \geq c\|w\|^2 \tag{3.1.39}$$

for all $w \in H^1(\Omega)$ and a constant $c > 0$. This follows from the uniformly ellipticity using an idea of Braess (cf. Braess [2013]): The uniform ellipticity causes a point-by-point estimation (for C^1 functions):

$$A\nabla w \cdot \nabla w = \sum_{i,k} a_{ik}\partial_i w \partial_k w \geq \alpha \sum_i (\partial_i w)^2. \tag{3.1.40}$$

Integration yields (since $\alpha \geq 0$)

$$a(w, w) \geq \sum_i \int_\Omega (\partial_i w)^2 \mathrm{d}z = \alpha|w|_1^2 \tag{3.1.41}$$

for $w \in H^1(\Omega)$. Due to Friedrich's inequality (Rektorys [2012], Braess [2013]) the seminorm $|.|_1$ and the norm $\|.\|_1$ are equivalent on H_0^1, which gives us

$$\alpha|w|_1^2 \geq c\|w\|_1^2 \tag{3.1.42}$$

for some constant $c > 0$. So the form a coming from the variational formulation of the Beltrami equation is an H^1-elliptic bilinear form on $H_0^1(\Omega)$.

As a last property we show the *continuity* of a by showing boundedness, again using an idea of Braess (cf. Braess [2013]): Let us define the generic constant $c := \sup\{|a_{ik}(z)|; \ z \in \Omega, 1 \leq i, k \leq 2\}$. Using the Cauchy-Schwarz inequality we get

$$\left|\sum_{i,k} \int_\Omega a_{ik}\partial_i u \partial_k w \mathrm{d}z\right| \leq c \cdot \sum_{ik} \int_\Omega |\partial_i u \partial_k w| \mathrm{d}z \tag{3.1.43}$$

$$\leq c \cdot \sum_{ik} \left(\int_\Omega (\partial_i u)^2 \mathrm{d}z \int_\Omega (\partial_k w)^2 \mathrm{d}z\right)^2 \tag{3.1.44}$$

$$\leq C|u|_1 \cdot |w|_1 \tag{3.1.45}$$

with $C = cn^2$ as energy norm of a (cf. Braess [2013, chapter 2.4]. The equivalence of $|.|_1$ and $\|.\|_1$ used in the proof of coercivity then gives us the continuity of a on $H_0^1(\Omega)$.

A Priori Error Estimation: As we just proved a is bounded and coercive. Thus, we can apply Cea's lemma (cf. Cea [1964]) to our problem, which states that

$$\|\nabla(u - u_h)\| \leq C \inf_{w_h \in V_h} \|\nabla(u - w_h)\|. \tag{3.1.46}$$

Assuming that the exact solution u is in $H^2(\Omega)$, we can get a better estimate for the later implementation by introducing the nodal interpolation operator
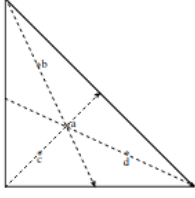
$$\Pi_h : H^2(\Omega) \to V_h \tag{3.1.47}$$

with

$$\|\nabla(u - \Pi_h u)\| \leq Ch\|u\|_{2,2} \tag{3.1.48}$$

for all $u \in H^2(\Omega)$. Combining 3.1.48 with the statement of Cea's lemma yields

$$\|\nabla(u - u_h)\| \leq Ch\|u\|_{2,2}. \tag{3.1.49}$$

(c) Cubic

$a = \left(\frac{1}{3}, \frac{1}{3}\right), \ w = -\frac{27}{48}$

$b = \left(\frac{1}{5}, \frac{3}{5}\right), \ w = \frac{25}{48}$

$c = \left(\frac{1}{5}, \frac{1}{5}\right), \ w = \frac{25}{48}$

$d = \left(\frac{3}{5}, \frac{1}{5}\right), \ w = \frac{25}{48}$

Figure 11: Cubic 2D quadrature formula on the reference cell $\hat{K}$ used in our implementation, figure from Deng [2017]

Assembly Process: As we have seen, the elements of the stiffness matrix M are obtained by integration over the whole domain Ω. This integral can be decomposed into the sum of integrals over the singular simplices of the triangulation:

$$M_{ij} = \int_\Omega \sum_{k,l} a_{kl} \partial_k \phi_j \partial_l \phi_i \mathrm{d}z = \sum_{K \in \mathcal{T}_h} \int_K \sum_{k,l} a_{kl} \partial_k \phi_j \partial_l \phi_i \mathrm{d}z. \tag{3.1.50}$$

We have the options to calculate the integrals directly on the cell K or to transform the integral to a reference cell $\hat{K}$ ($\hat{K} = \{(x,y) \in \mathbb{R}^2 \mid 0 \le x,y \le 1\}$ in our case). The second way is more favorable for the implementation of FEM. After an affine transformation to $\hat{K}$, one can apply a quadrature formula implemented for the reference element. However, one must look at how the terms in the integrals transform:

$$F_K : \ \hat{K} \to K, \ z \mapsto A_K z + b_K. \tag{3.1.51}$$

Using a two-dimensional quadrature formula we obtain for the integral over a cell K

$$\int_K \sum_{k,l} a_{kl} \partial_k \phi_j \partial_l \phi_i \mathrm{d}z = \int_K \sum_{k,l} a_{kl} \partial_k \phi_j(F_K(\hat{z})) \partial_l \phi_i(F_K(\hat{z})) |\det(A_K)| \mathrm{d}\hat{z} \tag{3.1.52}$$

$$\approx \sum_q w_q \sum_{k,l} a_{kl} \partial_k \phi_j(z_q) \partial_l \phi_i(z_q) |\det(A_K)| \mathrm{d}\hat{z} \tag{3.1.53}$$

with quadrature points $z_q = F_K(\hat{z}_q)$ and weights w_q. Here, we used the transformation theorem to shift the integration to the reference element. In our implementation, we use a cubic 2D quadrature formula as shown in figure 11.

3.1.3 Derivation of Shear and Convergence

In the following we use q^n to denote the approximated solution for a quantity q computed with a mesh width of $h(n)$. As only regular square meshes having 2^n boundary faces per coordinate direction are considered in chapter 4, we use $n \in \mathbb{N}$ to denote the resolution of our computation. From the computed lens mapping $f^n = u^n + iv^n$ with resolution n we can easily deduce the shear and convergence fields as discrete derivatives of f^n:

$$\kappa^n = 1 - f_z^n = 1 - \frac{1}{2}\left(\partial_{2x}^n - i\partial_{2y}^n\right)f^n = \left(1 - \frac{1}{2}\left(u_x^n + v_y^n\right)\right) + i\left(\frac{1}{2}\left(v_x^n - u_y^n\right)\right), \tag{3.1.54}$$

$$\gamma^n = \gamma_1^n + i\gamma_2^n = f_{\bar{z}}^n = \frac{1}{2}\left(\partial_{2x}^n + i\partial_{2y}^n\right)f^n = \frac{1}{2}\left(u_x^n - v_y^n\right) + i\left(\frac{1}{2}\left(v_x^n + u_y^n\right)\right). \tag{3.1.55}$$

Here, ∂_{2x}^n and ∂_{2y}^n denote the central difference operators in x- or y-direction, respectively. They are defined by

$$\delta_{2x}^n q(x_i, y_i) := \frac{q(x_{i+1}, y_i) - q(x_{i-1}, y_i)}{2h(n)} \tag{3.1.56}$$

and

$$\delta_{2y}^n q(x_i, y_i) := \frac{q(x_i, y_{i+1}) - q(x_i, y_{i-1})}{2h(n)} \tag{3.1.57}$$

for some quantity q defined on the mesh with fineness $h(n)$ and a point (x_i, y_i) on it. For the boundaries forward/backward approximations are used, which consider only the difference of the function values in positive or negative direction. Due to

$$\delta_{2x}^n q - q_x = O(h^2(n))), \tag{3.1.58}$$

$u^n \to u$ and $v^n \to v$ for $n \to \infty$ or $h \to 0$, respectively. Thus, in the limit we obtain

$$\kappa^n \to 1 - \frac{1}{2}\left(u_x + v_y\right) \text{ for } n \to \infty, \tag{3.1.59}$$

$$\gamma_1^n \to \frac{1}{2}\left(u_x - v_y\right) \text{ for } n \to \infty, \tag{3.1.60}$$

$$\gamma_2^n \to \frac{1}{2}\left(v_x + u_y\right) \text{ for } n \to \infty. \tag{3.1.61}$$

Since κ is a real quantity, apart from the difference

$$g - g^n = g - \gamma^n/(1 - \kappa^n), \tag{3.1.62}$$

the imaginary part of κ^n

$$\mathrm{Im}(\kappa^n) = \frac{1}{2}\left(v_x^n - u_y^n\right) \tag{3.1.63}$$

can be used to estimate the quality of our computed solution for a certain resolution n.

3.1.4 Derivation of the Lensing Potential

As usual, the lensing potential is determined by solving the Poisson equation with κ as inhomogeneity:

$$\Delta\Psi = 2\kappa. \tag{3.1.64}$$

However, this equation has only an unique solution if suitable boundary conditions for Ψ are specified. Since our algorithm computes the deflection field $\alpha = (\alpha_1, \alpha_2)$ and only afterwards κ, we know α on $\partial\Omega$. As the normal field $\boldsymbol{n} = (n_1, n_2)$ is given by $\partial\Omega$, we can specify Neumann boundary conditions for Ψ by

$$\frac{\partial\Psi}{\partial\boldsymbol{n}} = \boldsymbol{n} \cdot \nabla\Psi = n_1\Psi_x + n_2\Psi_y = n_1\alpha_1 + n_2\alpha_2 \tag{3.1.65}$$

and solve equation 3.1.64 with these boundary conditions, e.g. with a finite element approach again. Thus, we use the information obtained from the calculation of α to uniquely determine Ψ.

3.1.5 Comparison with the KS 93 Inversion Algorithm and its Extensions

The standard KS 93 inversion algorithm introduced in the introduction (with zero-padding) is as follows:

Algorithm 2 Standard KS 93 inversion algorithm (with zero-padding)

Input: maps of the shear components γ_1 and γ_2
Output: convergence map κ

1: $\gamma_{1,\text{pad}} := \text{PAD}(\gamma_1)$ $\quad$ $\gamma_{2,\text{pad}} := \text{PAD}(\gamma_2)$ $\hfill$ ▷ zero-padding of the shear maps
2: $\tilde{\gamma}_{1,\text{pad}} = \text{FFT}(\gamma_{1,\text{pad}})$ $\quad$ $\tilde{\gamma}_{2,\text{pad}} = \text{FFT}(\gamma_{2,\text{pad}})$ $\hfill$ ▷ Fast Fourier Transform (FFT) of shear components
3: $\tilde{D}_1(k_1, k_2) = \frac{k_1^2 - k_2^2}{k_1^2 + k_2^2}$ $\quad$ $\tilde{D}_2(k_1, k_2) = \frac{2k_1 k_2}{k_1^2 + k_2^2}$ $\hfill$ ▷ computation of the kernel on the zero-padded grid
4: $\tilde{\kappa}_{\text{pad}} = \tilde{D}_1 \cdot \tilde{\gamma}_{1,\text{pad}} + \tilde{D}_2 \cdot \tilde{\gamma}_{2,\text{pad}}$ $\hfill$ ▷ FFT of the convergence map
5: $\kappa_{\text{pad}} = \text{FFT}^{-1}(\tilde{\kappa}_{\text{pad}})$ $\hfill$ ▷ inverse FFT of the convergence map
6: $\kappa = \text{CROP}(\kappa_{\text{pad}})$ $\hfill$ ▷ cropping out the zero padded region

---

We now want to compare this algorithm with our proposed algorithm 1. To do this, we consider the following three points of comparison:

Boundary Conditions: As already mentioned in the introduction, the KS 93 algorithm has the disadvantage that the Fourier transform results as an integral over the entire $\mathbb{R}^2$ while observed fields are always finite. Extensions of the algorithm therefore always make assumptions about how the shear field γ behaves outside the observed field. Often one simply assumes that it disappears, e.g. in algorithm 2 we use zero-padding to limit the artifacts due to periodic boundary conditions. Furthermore, we have assumed $\kappa_0 = 0$ in equation 1.2.19, which gives us $\hat{\kappa}(0) = 0$ if the angular size of the observed shear field is sufficiently large, so that the mean convergence across the data field is approximated to zero. Otherwise, one must explicitly account for the boundary conditions imposed by the observed shear field to perform a mass reconstruction on a finite field (e.g. Kaiser et al. [1995], Seitz and Schneider [1995], Bartelmann et al. [1996], Seitz and Schneider [1996], Umetsu and Futamase [2000]).

However, if these assumptions cannot be made, algorithm 2 may not provide a suitable result. For our proposed algorithm, one does not need to make assumptions about the shear field γ outside the observed domain, but does need to make appropriate assumptions about the deflection field α at the boundary. Here one has to specify either Dirichlet or Neumann boundary conditions for each section of the boundary. These boundary conditions for α can then be translated into boundary conditions for f. Dirichlet boundary conditions must be physically motivated, since they cannot be measured directly. For instance, if we can assume that the deflection field vanishes on the boundary, one obtains

$$f(z) = z, \quad u(z) = x, \quad v(z) = y \tag{3.1.66}$$

for $z = x + iy \in \partial\Omega$. For Neumann boundary conditions one obtains for the real part u of f

$$\frac{\partial u}{\partial \boldsymbol{n}} = n_1 u_x + n_2 u_y = n_1(1 - \alpha_{1,x}) - n_2 \alpha_{1,y} = n_1(1 - \kappa - \gamma_1) - n_2 \gamma_2, \tag{3.1.67}$$

and for the imaginary part v

$$\frac{\partial v}{\partial \boldsymbol{n}} = n_1 v_x + n_2 v_y = -n_1 \alpha_{2,x} + n_2(1 - \alpha_{2,y}) = -n_1 \gamma_2 + n_2(1 + \kappa - \gamma_1). \tag{3.1.68}$$

In the weak lensing limit these conditions can be approximated as

$$\frac{\partial u}{\partial \boldsymbol{n}} = n_1 \tag{3.1.69}$$

and

$$\frac{\partial v}{\partial \boldsymbol{n}} = n_2. \tag{3.1.70}$$

39

As we will see in chapter 4 the computed lens mapping f^n assuming approximated Neumann boundary conditions still provides a good result for the actual f.

In summary, depending on the boundary conditions and assumptions that can be made about κ_0, κ, γ and α, one algorithm is more suitable than the other.

Non-Linear Regime: The standard KS 93 algorithm relates the convergence to the shear map, and in particular not to the reduced shear g, which is in principle observable from the image ellipticities. However, we can not measure γ_1 and γ_2 directly, apart from the weak lensing limit where $|\gamma| \ll 1$, $|\kappa| \ll 1$ and thus $g \approx \gamma$. As pointed out by Meneghetti [2021], Kaiser, Seitz and Schneider thus generalized the KS 93 algorithm to the non-linear but subcritical regime (outside the critical curves) by an iterative approach. By replacing γ with $(1 - \kappa)g$ we obtain from equation 1.2.15 an implicit integral equation

$$\kappa(\theta) - \kappa_0 = \frac{1}{\pi} \int_{\mathbb{R}^2} \Big[D_1(\theta - \theta')g_1(\theta')[1 - \kappa(\theta')] + D_2(\theta - \theta')g_2(\theta')[1 - \kappa(\theta')] \Big] \mathrm{d}^2\theta', \qquad (3.1.71)$$

which can be solved iteratively with initial value $\kappa \equiv 0$. The algorithm terminates when the result becomes stable and we obtain the final convergence map. This means that $\|\kappa_{\mathrm{pos}} - \kappa_{\mathrm{pre}}\| < \epsilon$ should be fullfilled after a finite number of iterations and ϵ chosen small enough. Due to norm equivalence, we have not explicitly specified any norm here. Additionally, we have assumed $\kappa_0 = 0$ in algorithm 3 as usual for practical applications.

Algorithm 3 KS 93 inversion algorithm for the non-linear regime

---

    Input: reduced shear map g (in principle observable)
    Output: convergence map κ and maps of the shear components γ_1 and γ_2
1: $\kappa_{\mathrm{pre}} \equiv 0$ ▷ initialisation
2: $\kappa_{\mathrm{pos}} = $ KS 93$((1 - \kappa_{\mathrm{pre}})g_1, (1 - \kappa_{\mathrm{pre}})g_2)$
3: **while** $(\|\kappa_{\mathrm{pre}}(\theta) - \kappa_{\mathrm{pos}}(\theta)\| \geq \epsilon)$ **do**   ▷ termination condition
4:     $\kappa_{\mathrm{pre}} = \kappa_{\mathrm{pos}}$
5:     $\kappa_{\mathrm{pos}} = $ KS 93$((1 - \kappa_{\mathrm{pre}})g_1, (1 - \kappa_{\mathrm{pre}})g_2)$
6: **end while**
7: $\kappa = \kappa_{\mathrm{pos}}$; $\gamma_1 = (1 - \kappa_{\mathrm{pos}})g_1$ and $\gamma_2 = (1 - \kappa_{\mathrm{pos}})g_2$

Unfortunately, we could not find any rigorous convergence statements for this method in the literature, unless the statement, that the method usually converges (cf. Meneghetti [2021]). Furthermore, an estimation using Banach's fixed point theorem was not successful.

Our algorithm avoids this difficulty by directly calculating the lens mapping f by means of g, from which one can infer κ and γ: We do not need to distinguish between the linear and non-linear regime. Moreover, given suitable boundary conditions, f^h always converges to f for $h \to 0$ and thus κ^h to κ. In comparison, each iteration step in algorithm 3 introduces an error by applying the KS 93 algorithm, which calculates the corresponding integral over a restricted subset of $\mathbb{R}^2$ instead of over the entire plane.

Mass-Sheet Degeneracy: According to Umetsu et al. [1999] equation 3.1.71 can be formally expressed as a power series expansion

$$\kappa(\theta) - \kappa_0 = (1 - \kappa_0)\left(\hat{\mathcal{G}} - \hat{\mathcal{G}} \circ \hat{\mathcal{G}} + \hat{\mathcal{G}} \circ \hat{\mathcal{G}} \circ \hat{\mathcal{G}} - \cdots \right)$$

$$= (1 - \kappa_0) \sum_{n=1}^{\infty} (-1)^{n-1} \hat{\mathcal{G}}^n, \qquad (3.1.72)$$

where $\hat{\mathcal{G}}$ denotes the convolution operator defined by

$$\hat{\mathcal{G}}(\theta, \theta') := \frac{1}{\pi} \int \mathrm{d}^2\theta' D^*(\theta - \theta')g(\theta') \times . \qquad (3.1.73)$$

This is the same idea on which the van Cittert deconvolution in image processing is based. The operator $\hat{\mathcal{G}}(\boldsymbol{\theta}, \boldsymbol{\theta}')$ acts on a function of the variable $\boldsymbol{\theta}'$. If one approximates this power series expansion to first order in the weak lensing limit, one just obtains the standard KS 93 algorithm. It can be seen explicitly from equation 3.1.72 that non-linear mass reconstructions suffer from the mass-sheet degeneracy: As κ in equation 3.1.72 depends only on g, it does not change under the transformation of κ in equation 1.1.20!

We avoid the mass-sheet degeneracy by determining κ (and γ) via the detour over α or f respectively. As linear combinations of the derivatives of the deflection field, κ (and γ) are uniquely determined by f. f again is uniquely determined from g by assuming suitable boundary conditions. Thus, we do not need an additional, independent measurement, e.g. the magnification, to break the mass-sheet degeneracy. However, we need to assume appropriate boundary conditions for the deflection field, which we can not measure directly. This is the main disadvantage of our method.

Note that we did not compared our proposed algorithms with the class of mass inversion algorithms that uses maximum-likelihood and Bayesian approaches to obtain κ and its error covariance matrix from weak lensing data (e.g Bartelmann et al. [1996], Bradač et al. [2006], Merten et al. [2009]).

3.1.6 Concrete Implementation

For the implementation of algorithm 1 we used *HiFlow³*. *HiFlow³* is a multi-purpose finite element software written in C++ providing powerful tools for efficient and accurate solution of a wide range of problems modeled by PDEs [1]. In particular, it provides routines for:

1. read and modify triangulations Γ_h

2. setup finite element space V_h

3. linear algebra objects

4. assembly routines for building the stiffness matrix M and right hand side vector b

5. linear solvers like CG and GMRES

6. post-processing routines

7. creation of visualization files for the computed solution

With these routines, all we essentially need to do for the implementation of algorithm 1 is the following:

1. provide an initial triangulation Γ_h of our domain Ω with mesh width h

2. calculate the matrix A at each node of our triangulation based on the Beltrami coefficient $\mu = -g$ at that node

3. code the variational formulation of our two elliptic PDEs for u and v

4. code the boundary conditions (Dirichlet, Neumann or mixed)

5. obtain κ and γ by a simple derivation of the lens mapping $f = u + \mathrm{i}v$

As solver for the resulting linear system we used CG with no preconditioning since the stiffness matrix M is symmetric, positive definite due to the ellipticity of the PDEs. The assembly process of M was done using a cubic 2D quadrature formula on each reference cell $\hat{K} = \{(x, y) \in \mathbb{R}^2 \mid 0 \leq x, y \leq 1\}$. The visualisation process was done using the VTU file format, ParaView and the Python library matplotlib. For the evaluation and comparison with algorithms 2 and 3 we made use of Python [2].

---

[1] The source code can be found under `https://emcl-gitlab.iwr.uni-heidelberg.de/hiflow3.org/hiflow3/`.

[2] The complete code base for algorithm 1 can be found at `https://github.com/JanJakob1/BSc_thesis`. It also contains instructions for setup and running the code.

3.1.7 Further Approaches

Instead of computing the planar q.c. mapping f by reducing it to two elliptic PDEs for real and imaginary part, f can also be obtained with all those algorithms from the literature that compute q.c. mappings between two domains in $\mathbb{C}$. Even by reduction of f to two elliptic PDEs, these do not have to be solved using FEM, e.g. Chun and Lui [2013] proposes a different approach using a so-called linear Beltrami solver. However, the author developed his own solution and implemented the algorithm himself, since source code of other projects was not publicly or only partially publicly available and authors left requests unanswered.

3.2 Proposed Inversion Algorithm for Curved Fields

To date weak gravitational lensing surveys have typically been restricted to small fields of view, such that the flat-sky approximation has been sufficiently satisfied (CFHTLenS Collaboration et al. [2013], Vikram et al. [2015], Chang et al. [2015]). In fact, as shown in Wallis et al. [2021], the gain in moving from flat-sky to curved-sky is very marginal in the case where the data is on the order of 100 deg^2. However, inversion methods for large areas of the sky, where the plane sky approximation can not be longer be assumed, have become highly relevant with Stage IV surveys (e.g. LSST and Euclid). Imminent, extending mass-mapping techniques to the sphere is a fundamental necessity for such surveys. Therefore, we assume in the following the field of view to be sufficiently large to warrant a curved-sky treatment.

It is natural to ask whether the results of the planar case can be generalized to the curved-sky treatment: If the plane sky approximation is considered as a coordinate chart around a given point on the curved surface, the Beltrami equation holds locally in this chart. Globally, however, a flat-sky treatment provides not an adequate description, since the field of view is too large. Therefore, from a differential geometric perspective, it makes sense to try to describe the lens mapping f as a q.c. mapping between curved surfaces. To do this, we use the notion of a Beltrami differential introduced above. In each chart then the flat-sky approximation holds and f should locally satisfy the Beltrami equation.

3.2.1 Review of DES Inversion Algorithm

We want to give a short summary of an inversion algorithm for the curved-sky treatment, which was used in the evaluation of the dark energy survey year 1 results (DES Collaboration et al. [2018]). The idea is to generalize the classical Helmholtz decomposition to spherical coordinates by decomposing the spin-2 field γ into a curl-free and divergence-free component. This is done using spin-weighted spherical harmonics. The curl-free component corresponds to the convergene, which is also referred to as the E-mode convergence field κ_E. The divergence-free component, which we refer to as κ_B, is expected to be negligible compared to κ_E for gravitational lensing. However, due to noise and systematics in the shear estimates κ_B does not necessarily vanish. We sketch below the formalism of converting between κ and γ as well as the deflection field α and the lensing potential Ψ. For detailed derivations, we refer to Castro et al. [2005], Bartelmann [2010] and Wallis et al. [2021].

We start with expanding the (spin-0) lensing potential Ψ at a given comoving distance χ in spherical harmonics:

$$\Psi(\chi) = \sum_{lm} \Psi_{lm}(\xi) {}_0Y_{lm}(\theta, \phi), \qquad (3.2.1)$$

with coefficients

$$\Psi_{lm}(\chi) = \int d\Omega \Psi(\chi) {}_0Y^*_{lm}(\theta, \phi). \qquad (3.2.2)$$

${}_0Y_{lm} = Y_{lm}$ is the spin-0 spherical harmonic basis set and $\Psi_{lm}(\chi)$ are the corresponding coefficients. For simplicity we will omit χ in our notation below. To derive the spherical harmonic representation of shear

and convergence, we use the raising and lowering operators ð and $\bar{\text{ð}}$. This gives us for the convergence

$$\kappa = \frac{1}{4}(\text{ð}\bar{\text{ð}} + \bar{\text{ð}}\text{ð})\Psi, \qquad (3.2.3)$$

and for the shear

$$\gamma = \gamma_1 + i\gamma_2 = \frac{1}{2}\text{ð}\bar{\text{ð}}\Psi. \qquad (3.2.4)$$

Here, ð and $\bar{\text{ð}}$ act on the spin-weighted spherical harmonics $_sY_{lm}$ following a certain set of rules (see e.g. Castro et al. [2005]). Since κ is a spin-0 and γ a spin-2 quantity, we obtain

$$\kappa = \kappa_E + i\kappa_B = \sum_{lm}(\hat{\kappa}_{E,lm} + i\hat{\kappa}_{B,lm})_0 Y_{lm},$$

$$\gamma = \gamma_1 + i\gamma_2 = \sum_{lm}\hat{\gamma}_{lm} \, _2Y_{lm}. \qquad (3.2.5)$$

Combining these equations with 3.2.3 and 3.2.4 yields

$$\hat{\kappa}_{E,lm} + i\hat{\kappa}_{B,lm} = -\frac{1}{2}l(l+1)\Psi_{lm}, \qquad (3.2.6)$$

$$\begin{aligned}
\hat{\gamma}_{lm} &= \hat{\gamma}_{E,lm} + i\hat{\gamma}_{B,lm} \\
&= \frac{1}{2}[l(l+1)(l-1)(l+2)]^{\frac{1}{2}}\Psi_{lm} \\
&= -\sqrt{\frac{(l+2)(l-1)}{l(l+1)}}(\hat{\kappa}_{E,lm} + i\hat{\kappa}_{B,lm}).
\end{aligned} \qquad (3.2.7)$$

We see: Analogously to the planar case we can convert between the three fields κ, γ and Ψ by manipulating their spherical harmonics decompositions. These expressions generalize the usual KS formalism: In the flat-sky limit, we have $\text{ð} \to \partial$ and the spin-weighted spherical harmonics are replaced by the Fourier transform:

$$\sum_{lm}\Psi_{lm}Y_{lm} \to \int \frac{d^2l}{(2\pi)^2}\Psi(l)e^{il\cdot\theta}. \qquad (3.2.8)$$

This gives just the well-known relation between κ and γ from the introduction. Additionally, one can derive the deflection field α in a similar fashion. Since α is the first derivative of Ψ,

$$\alpha = \alpha_1 + i\alpha_2 = \text{ð}\Psi \qquad (3.2.9)$$

is a spin-1 field. Thus is can be expressed as

$$\alpha = \sum_{lm}\hat{\alpha}_{lm}Y_{lm}. \qquad (3.2.10)$$

Carrying through the derivation yields for the coefficients

$$\hat{\alpha}_{lm} = [l(l+1)]^{\frac{1}{2}}\Psi_{lm}. \qquad (3.2.11)$$

Analogously to the other coefficients, $\hat{\alpha}_{lm}$ is again related to the other lensing quantities via a linear operation in the spin-harmonic space. So from the measurement of γ one can construct directly the other quantities using the above formalism, in particular κ.

3.2.2 Approach for a Inversion Algorithm for Curved Fields Using Quasi-Conformal Geometry

Our goal is to examine whether for curved fields the lens mapping f can be described as a q.c. mapping similiar to the planar case. Let therefore S be a connected subset of the celestical sphere. S should be large enough, such that the flat-sky approximation is not sufficiently satisfied. However, in a neighbourhood around an arbitrary point $p \in S$ the flat-sky approximation still provides an suitable description of the lensing mapping. To make this idea more concrete we first want to give a mathematically description of the flat-sky approximation:

Flat-Sky Approximation: Let the celestical sphere $\mathbb{S}^2$ be centered around the origin, i.e. the the center of the sphere should coincide with the origin. Since any arbitrary point $p \in \mathbb{S}^2$ can be identified with the north pole $(0, 0, 1)$ after rotation, we can assume $p = (0, 0, 1)$. Consider a point $p' \in \mathbb{S}^2$ lying in a neighbourhood of p. Using spherical coordinates p' can be parametrized by the two angles θ and ϕ as shown in figure 12. From simple geometrical considerations in the right picture of figure 12 we get that $p' = (\theta, \phi)$ corresponds to the point $(\tan(\theta)\cos(\phi), \tan(\theta)\sin(\phi))$ in the $z = 1$ plane.
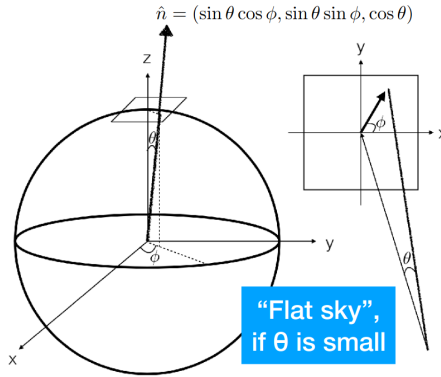
Figure 12: Illustration of the flat-sky approximation, figure from Komatsu [2017]

Thus, the flat-sky approximation can be described by the following mapping:

$$\sigma : \mathbb{S}^2 \to \mathbb{R}^2, \ p' = (\theta, \phi) \mapsto (\tan(\theta)\cos(\phi), \ \tan(\theta)\sin(\phi)). \tag{3.2.12}$$

The angle θ should be small in the flat-sky approximation, which yields in the first order:

$$\psi : \mathbb{S}^2 \to \mathbb{R}^2, \ p' = (\theta, \phi) \mapsto (\theta \cos(\phi), \ \theta \sin(\phi)). \tag{3.2.13}$$

Conversly, for the inverse mapping of σ we obtain

$$\sigma^{-1} : \mathbb{R}^2 \to \mathbb{S}^2, \ (x, y) \mapsto \begin{cases} \left(\arctan(\sqrt{x^2 + y^2}), \ \arctan(y/x)\right) & \text{if } x \neq 0 \\ \left(\arctan(\sqrt{x^2 + y^2}), \ \pi/2\right) & \text{if } x = 0, \ y \neq 0 \ , \\ (0, 0) & \text{if } x = 0, \ y = 0 \end{cases} \tag{3.2.14}$$

and for ψ accordingly:

$$\psi^{-1} : \mathbb{R}^2 \to \mathbb{S}^2, \ (x, y) \mapsto \begin{cases} \left(\sqrt{x^2 + y^2}, \ \arctan(y/x)\right) & \text{if } x \neq 0 \\ \left(\sqrt{x^2 + y^2}, \ \pi/2\right) & \text{if } x = 0, \ y \neq 0 \ . \\ (0, 0) & \text{if } x = 0, \ y = 0 \end{cases} \tag{3.2.15}$$

By using the identities $\cos(\arctan(x)) = \frac{1}{\sqrt{1+x^2}}$ and $\sin(\arctan(x)) = \frac{x}{\sqrt{1+x^2}}$ we can check

$$(\sigma \circ \sigma^{-1})(x, y) = \left(\tan(\arctan(\sqrt{x^2 + y^2}))\cos(\arctan(y/x)), \ \tan(\arctan(\sqrt{x^2 + y^2}))\sin(\arctan(y/x))\right)$$

44

$$= \left(\sqrt{x^2 + y^2} \frac{1}{\sqrt{1 + (y/x)^2}}, \quad \sqrt{x^2 + y^2} \frac{y/x}{\sqrt{1 + (y/x)^2}} \right) = (x, y) \tag{3.2.16}$$

for $x \neq 0$ and

$$(\sigma \circ \sigma^{-1})(x, y) = \left(\tan(\arctan(\sqrt{x^2 + y^2}))\cos(\pi/2), \quad \tan(\arctan(\sqrt{x^2 + y^2}))\sin(\pi/2) \right)$$

$$= \left(0, \sqrt{x^2 + y^2} \right) = (x, y) \tag{3.2.17}$$

for $x = 0$ but $y \neq 0$. The case $(x, y) = (0, 0)$ is trivially satisfied. On the other hand:

$$(\sigma^{-1} \circ \sigma)(\theta, \phi) = \left(\arctan(\sqrt{(\tan(\theta)\cos(\phi))^2 + (\tan(\theta)\sin(\phi))^2}), \quad \arctan((\tan(\theta)\sin(\phi))/(\tan(\theta)\cos(\phi))) \right)$$

$$= (\theta, \phi) \tag{3.2.18}$$

for $\theta \neq 0$. Analogously one obtains for $\theta = 0$ the point $(0, 0)$. The same applies to ψ, which we do not want to show explicitly here.

Complex Atlas on S: We now want to construct an atlas $\mathcal{A}_S$ on S using 3.2.13 as chart mapping. Let us start with the construction of the chart domains: Let $\mathcal{M}$ be an empty set and $\epsilon \ll 1$ be a small angle. We choose an arbitrary point $p = (\theta, \psi) \in S$, add p to $\mathcal{M}$, and from p consider the four points $(\theta - \epsilon, \phi)$, $(\theta + \epsilon, \phi)$, $(\theta, \phi - \epsilon)$ and $(\theta, \phi + \epsilon) \in \mathbb{S}^2$. We add each of these four points to $\mathcal{M}$ if it is contained in S. In this way we get a grid on S, which is shown in figure 13.
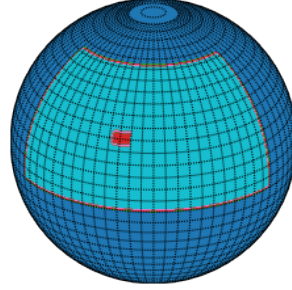
Figure 13: Illustration of the area S. Two adjacent lines of longitude and latitude have an angular distance of ϵ. The set of all intersections of longitude and latitude within the olive-colored area corresponds to the set $\mathcal{M}$. The red-colored square represents one coordinate domain on S.

As chart domains for $\mathcal{A}_S$ we choose the following open neighborhoods U_p for all $p = (\theta_p, \phi_p) \in \mathcal{M}$:

$$U_p := \{ p' = (\theta', \phi') \in S \mid \theta' - \theta_p < \epsilon/2 + \delta \text{ and } \phi' - \phi_p < \epsilon/2 + \delta \}. \tag{3.2.19}$$

δ is a positive constant, which in principle can be chosen freely. However, we assume δ to be small enough ($\delta \ll \epsilon/2$). It ensures that two adjacent chart domains overlap. As complex chart we then pick

$$\psi_p : U_p \rightarrow \psi_p(U_p) \subset \mathbb{C}, \quad p' = (\theta', \phi') \mapsto (\theta' - \theta_p)\cos(\phi' - \phi_p) + i(\theta' - \theta_p)\sin(\phi' - \phi_p). \tag{3.2.20}$$

We used the above approximation for small angles θ. We need the subtraction with θ_p or ϕ_p because we consider the tangent plane at p and the point $p' = p$ should correspond to the point $z = 0$ in $\mathbb{C}$. As inverse map we obtain

$$\psi_p^{-1} : \psi_p(U_p) \subset \mathbb{C} \rightarrow U_p, \quad z = x + iy \mapsto \begin{cases} \left(\sqrt{x^2 + y^2} + \theta_p, \ \arctan(y/x) + \phi_p \right) & \text{if } x \neq 0 \\ \left(\sqrt{x^2 + y^2} + \theta_p, \ \pi/2 + \phi_p \right) & \text{if } x = 0, \ y \neq 0 \ . \\ (\theta_p, \phi_p) & \text{if } x = 0, \ y = 0 \end{cases} \tag{3.2.21}$$

Analogously to above, one calculates that $\psi_p \circ \psi_p^{-1} = \mathrm{id}_{\psi_p(U_p)}$ and $\psi_p^{-1} \circ \psi_p = \mathrm{id}_{U_p}$. Thus, ϕ_p is a complex chart and the set $\mathcal{A}_S = \{\psi_p \mid p \in \mathcal{M}\}$ defines a complex atlas on S.

Conformal Structure on S: We want to check whether $\mathcal{A}_S$ is conformal. Let therefore $\psi_p : U_p \to \psi_p(U_p)$ and $\psi_q : U_q \to \psi_q(U_q)$ be two complex charts. Without loss of generality we only need to investigate the case $q = (\theta_p - \epsilon, \phi_p - \epsilon)$. The transition function $\psi_q \circ \psi_p^{-1}$

$$\psi_q \circ \psi_p^{-1} : \ \psi_p(U_p \cap U_q) \to \psi_q(U_p \cap U_q),$$

$$z = x + iy \mapsto \begin{cases} (\sqrt{x^2+y^2} + \epsilon)\cos(\arctan(y/x) + \epsilon) + i(\sqrt{x^2+y^2} + \epsilon)\sin(\arctan(y/x) + \epsilon) & \text{if } x \neq 0 \\ (\sqrt{x^2+y^2} + \epsilon)\cos(\pi/2 + \epsilon) + i(\sqrt{x^2+y^2} + \epsilon)\sin(\pi/2 + \epsilon) & \text{if } x = 0,\ y \neq 0 \ , \\ \epsilon(\cos(\epsilon) + i\sin(\epsilon)) & \text{if } x = 0,\ y = 0 \end{cases}$$

$$(3.2.22)$$

is then bijective with inverse $\psi_p \circ \psi_q^{-1}$ given by

$$\psi_p \circ \psi_q^{-1} : \ \psi_q(U_p \cap U_q) \to \psi_p(U_p \cap U_q),$$

$$z = x + iy \mapsto \begin{cases} (\sqrt{x^2+y^2} - \epsilon)\cos(\arctan(y/x) - \epsilon) + i(\sqrt{x^2+y^2} - \epsilon)\sin(\arctan(y/x) - \epsilon) & \text{if } x \neq 0 \\ (\sqrt{x^2+y^2} - \epsilon)\cos(\pi/2 - \epsilon) + i(\sqrt{x^2+y^2} - \epsilon)\sin(\pi/2 - \epsilon) & \text{if } x = 0,\ y \neq 0 \ . \\ -\epsilon(\cos(\epsilon) - i\sin(\epsilon)) & \text{if } x = 0,\ y = 0 \end{cases}$$

$$(3.2.23)$$

Since $\psi_p \circ \psi_q^{-1}$ and $\psi_q \circ \psi_p^{-1}$ are smooth when regarded as functions on $\mathbb{R}^2$, for holomorphy we only need to check whether the Cauchy-Riemann equations are fullfilled:

$$\frac{\partial \mathrm{Re}(\psi_p \circ \psi_q^{-1})}{\partial x} - \frac{\partial \mathrm{Im}(\psi_p \circ \psi_q^{-1})}{\partial y} = \epsilon \ \frac{-x\cos(\epsilon + \arctan(y/x)) + y\sin(\epsilon + \arctan(y/x))}{x^2 + y^2} \neq 0, \quad (3.2.24)$$

$$\frac{\partial \mathrm{Re}(\psi_p \circ \psi_q^{-1})}{\partial y} + \frac{\partial \mathrm{Im}(\psi_p \circ \psi_q^{-1})}{\partial x} = -\epsilon \ \frac{x\sin(\epsilon + \arctan(y/x)) + y\cos(\epsilon + \arctan(y/x))}{x^2 + y^2} \neq 0, \quad (3.2.25)$$

and accordingly:

$$\frac{\partial \mathrm{Re}(\psi_q \circ \psi_p^{-1})}{\partial x} - \frac{\partial \mathrm{Im}(\psi_q \circ \psi_p^{-1})}{\partial y} = \epsilon \ \frac{x\cos(\epsilon - \arctan(y/x)) + y\sin(\epsilon - \arctan(y/x))}{x^2 + y^2} \neq 0, \quad (3.2.26)$$

$$\frac{\partial \mathrm{Re}(\psi_q \circ \psi_p^{-1})}{\partial x} - \frac{\partial \mathrm{Im}(\psi_q \circ \psi_p^{-1})}{\partial y} = \epsilon \ \frac{-x\sin(\epsilon - \arctan(y/x)) + y\cos(\epsilon - \arctan(y/x))}{x^2 + y^2} \neq 0. \quad (3.2.27)$$

So in general the transition functions are not holomorphic. However, the denominator is bounded below as U_p overlaps with U_q only in the area $\{(\theta, \phi) \mid \theta_p - \epsilon/2 - \delta < \theta < \theta_p + \epsilon/2 + \delta, \ \phi_p - \epsilon/2 - \delta < \phi < \phi_p - \epsilon/2 + \delta\}$. Thus, the quality of our conformal structure is determined how large we chose our domains U_p, which depend on ϵ and δ. Unfortunately, we were not able to make a concrete estimate of the difference upwards, since x and y both depend on ϵ.

For $q = (\theta_p, \phi_p - \epsilon)$ and $q = (\theta_p, \phi_p + \epsilon)$ the Cauchy-Riemann equations are fullfilled for both $\psi_q \circ \psi_p^{-1}$ and $\psi_p \circ \psi_q^{-1}$. If our area on the celestial sphere therefore corresponds to a narrow long strip with extension along one degree of latitude as illustrated in figure 14, we can model this area as a Riemann surface by means of the flat-sky approximation.
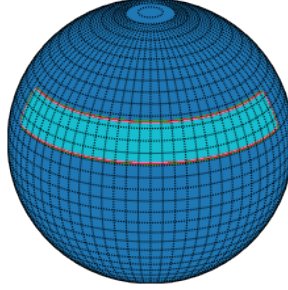
Figure 14: Illustration of a narrow strip with extension along one degree of latitude

Isothermal Coordinates on S: We want to investigate whether the ψ_p are isothermal coordinate charts. To do this, we first calculate the two tangent vectors as in the example of the stereographic mapping. For simplification we consider the mapping ψ^{-1} defined in equation 3.2.15 and the case $x \neq 0$, since the two cases for $x = 0$ follow analogously. A point $(x, y) \in \mathbb{R}^2$ corresponds then to the point

$$
\begin{aligned}
X &= \left(\sin(\sqrt{x^2 + y^2})\cos(\arctan(y/x)), \ \sin(\sqrt{x^2 + y^2})\sin(\arctan(y/x)), \ \cos(\sqrt{x^2 + y^2}) \right) \\
&= \left(\sin(\sqrt{x^2 + y^2})\frac{x}{\sqrt{x^2 + y^2}}, \ \sin(\sqrt{x^2 + y^2})\frac{y}{\sqrt{x^2 + y^2}}, \ \cos(\sqrt{x^2 + y^2}) \right) \in \mathbb{S}^2 \subset \mathbb{R}^3.
\end{aligned}
\tag{3.2.28}
$$

If we compute the scalar product of the tangent vectors $X_1 = \frac{\partial X}{\partial x}$ and $X_2 = \frac{\partial X}{\partial y}$ we obtain

$$
X_1 \cdot X_2 = \frac{xy \left(x^2 + y^2 - \sin^2\left(\sqrt{x^2 + y^2} \right) \right)}{x^4 + 2x^2 y^2 + y^4} \neq 0.
\tag{3.2.29}
$$

Thus, the flat-sky approximation provides no isothermal coordinates in contrast to the stereographic mapping. This can also be intuitively justified: The two coordinate mappings of the stereographic projection are biholomorphic, in particular conformal, i.e. angle-preserving. Infinitesimal squares are therefore mapped to infinitesimal squares again. As we have seen, for the flat-sky approximation this biholomorphism is not given.

Beltrami Differential on S: For the description of the lens mapping f as q.c. mapping we need to define a suitable Beltrami differential $\mu \frac{d\bar{z}}{dz}$ on S. Therefore, we work with definition 2 of the Beltrami differential from chapter 2.4.2. Each chart (U_p, ψ_p) is assigned a function $\mu_p : \psi_p(U_p) \to \mathbb{C}$, $z_p \mapsto \mu_p(z_p)$, such that the transformation rule

$$
\mu_p \frac{d\bar{z}_p}{d\bar{z}_q} = \mu_q \frac{dz_p}{dz_q}
\tag{3.2.30}
$$

holds on the part of the domain U_p, which is also covered by the chart (U_q, ψ_q). μ_p must be related to the reduced shear field $g : S|_{U_p} \to \mathbb{C}$ on U_p, since $\psi_p \circ f \circ \psi_p^{-1}$ should satisfies the Beltrami equation with Beltrami coefficient $\mu_p = -g(\psi_p^{-1}(z_p))$ in the coordinates z_p. As ansatz for μ_p we therefore choose

$$
\mu_p(z_p) := -g(\psi_p^{-1}(z_p)).
\tag{3.2.31}
$$

We first try to show the transformation rule for the special case that S is the narrow long strip shown in figure 14. It holds

$$
\mu_p(z_p) = -g(\psi_p^{-1}(z_p)) = -g((\psi_q^{-1} \circ \psi_q \circ \psi_p^{-1})(z_p)) = -g(\psi_q^{-1}(z_q)) = \mu_q(z_q),
\tag{3.2.32}
$$

since the transition function $\psi_q \circ \psi_p^{-1}$ transforms the coordinate z_p to the coordinate z_q. For the derivatives of $\psi_q \circ \psi_p^{-1}$ we obtain

$$
\frac{\overline{(\psi_q \circ \psi_p^{-1})'(z_p)}}{(\psi_q \circ \psi_p^{-1})'(z_p)} = e^{-2i\epsilon}.
\tag{3.2.33}
$$

47

In summary:

$$\mu_p(z_p) = \mu_q(z_q)e^{-2i\epsilon} \simeq \mu_q(z_q)(1 - 2i\epsilon + \dots). \tag{3.2.34}$$

Thus, for ϵ small enough, we can assume in first approximation that μ defined in this way represents a Beltrami differential. As mentioned in chapter 2.4.2, this example shows that due to $|e^{-2i\epsilon}| = 1$ $z \mapsto |\mu(z)|$ is a well-defined function on S.

In the general case equation 3.2.33 is not true and can also not be approximated by a Taylor series expansion to 1 for small ϵ:

$$\frac{\overline{(\psi_q \circ \psi_p^{-1})'(z_p)}}{(\psi_q \circ \psi_p^{-1})'(z_p)} = \frac{\epsilon y \sin\left(\epsilon + \operatorname{atan}\left(\frac{y}{x}\right)\right) + i\epsilon y \cos\left(\epsilon + \operatorname{atan}\left(\frac{y}{x}\right)\right) - ix\sqrt{x^2+y^2}\sin\left(\epsilon + \operatorname{atan}\left(\frac{y}{x}\right)\right) + x\sqrt{x^2+y^2}\cos\left(\epsilon + \operatorname{atan}\left(\frac{y}{x}\right)\right) + y\sqrt{x^2+y^2}\sin\left(\epsilon + \operatorname{atan}\left(\frac{y}{x}\right)\right) + iy\sqrt{x^2+y^2}\cos\left(\epsilon + \operatorname{atan}\left(\frac{y}{x}\right)\right)}{\epsilon y \sin\left(\epsilon + \operatorname{atan}\left(\frac{y}{x}\right)\right) - i\epsilon y \cos\left(\epsilon + \operatorname{atan}\left(\frac{y}{x}\right)\right) + ix\sqrt{x^2+y^2}\sin\left(\epsilon + \operatorname{atan}\left(\frac{y}{x}\right)\right) + x\sqrt{x^2+y^2}\cos\left(\epsilon + \operatorname{atan}\left(\frac{y}{x}\right)\right) + y\sqrt{x^2+y^2}\sin\left(\epsilon + \operatorname{atan}\left(\frac{y}{x}\right)\right) - iy\sqrt{x^2+y^2}\cos\left(\epsilon + \operatorname{atan}\left(\frac{y}{x}\right)\right)}. \tag{3.2.35}$$

However, $\epsilon \to 0$ yields $\frac{\overline{(\psi_q \circ \psi_p^{-1})'(z_p)}}{(\psi_q \circ \psi_p^{-1})'(z_p)} \to 1$ and thus the transformation rule is fullfilled in the limit of $\epsilon \to 0$.

Quasi-Conformal Mapping on S: We now come to the actual goal of our previous considerations: As mentioned in the introduction, we want to regard f as q.c. mapping on S. For this we first consider only one chart (U_p, ψ_p). Since by construction we have chosen U_p to be small, $\psi_p \circ f \circ \psi_p^{-1}$ just satisfies the Beltrami equation with Beltrami coefficient given by equation 3.2.31:

$$\frac{\partial(\psi_p \circ f \circ \psi_p^{-1})}{\partial\bar{z}} = -g(\psi_p^{-1}(z_p))\frac{\partial(\psi_p \circ f \circ \psi_p^{-1})}{\partial z}. \tag{3.2.36}$$

This applies to all $p \in \mathcal{M}$ and independent of the concrete form of S. We have therefore chosen the flat-sky approximation as chart mapping such that f locally satisfies the Beltrami equation, i.e. $\psi_p \circ f \circ \psi_p^{-1}$ fullfills the Beltrami equation on U_p for all $p \in \mathcal{M}$.

However, in order to understand f as a q.c. mapping on S, this is still not sufficient, as the definition in section 2.4.3 shows: We must additionally require that $f_{pq} := \psi_q \circ f \circ \psi_p^{-1}$ is q.c. associated with $\mu_p \frac{d\bar{z}_p}{dz_p}$ (assuming that U_p and U_q overlap). As above, we first consider the case where S is the narrow long strip from figure 14. In this case S can be modeled by the flat-sky approximation as a Riemann surface with a well-defined Beltrami differential in first approximation. By means of the chain rule we obtain:

$$\frac{\partial(\psi_q \circ f \circ \psi_p^{-1})}{\partial\bar{z}} = \frac{\partial(\psi_q \circ f \circ \psi_q^{-1} \circ \psi_q \circ \psi_p^{-1})}{\partial\bar{z}}$$

$$= \frac{\partial(\psi_q \circ \psi_p^{-1})}{\partial\bar{z}}\frac{\partial(\psi_q \circ f \circ \psi_q^{-1})}{\partial\bar{z}}$$

$$= \frac{\partial(\psi_q \circ \psi_p^{-1})}{\partial\bar{z}}\mu_q(z_q)\frac{\partial(\psi_q \circ f \circ \psi_q^{-1})}{\partial z}$$

$$= \mu_q(z_q)\frac{\partial(\psi_q \circ \psi_p^{-1})}{\partial\bar{z}}\frac{\partial(\psi_q \circ f \circ \psi_p^{-1} \circ \psi_p \circ \psi_q^{-1})}{\partial z}$$

$$= \mu_q(z_q)\frac{\partial(\psi_q \circ \psi_p^{-1})}{\partial\bar{z}}\frac{\partial(\psi_p \circ \psi_q^{-1})}{\partial z}\frac{\partial(\psi_q \circ f \circ \psi_p^{-1})}{\partial z}$$

$$= \mu_q(z_q)\frac{\overline{(\psi_q \circ \psi_p^{-1})'}}{(\psi_q \circ \psi_p^{-1})'}\frac{\partial(\psi_q \circ f \circ \psi_p^{-1})}{\partial z}$$

$$= \mu_p(z_p)e^{-2i\epsilon}\frac{\partial(\psi_q \circ f \circ \psi_p^{-1})}{\partial z} \tag{3.2.37}$$

$$\simeq \mu_p(z_p)\frac{\partial(\psi_q \circ f \circ \psi_p^{-1})}{\partial z}. \tag{3.2.38}$$

Here, we have used the fact that f_{qq} just satisfies the Beltrami equation and made use of the transformation rule for the Beltrami differential in the second last step. The equality in the last step is finally

obtained by the above Taylor approximation for small ϵ.

If we consider general areas S, the above transformations are valid up to equation 3.2.37, where we need to replace the factor $e^{2i\epsilon}$ by the more general expression 3.2.35. Since this expression cannot (probably) be Taylor approximated for small ϵ, however, the last equality does not hold. Only in the limit $\epsilon \to 0$ one obtains equality as described above.

Computation of the Lens Mapping f: We restrict ourselves to the case where S is the narrow strip from figure 14. Otherwise, it is difficult to estimate to what extent the compatibility equations are satisfied and f can then be modeled as a well-defined q.c. mapping. For the case of a narrow strip, however, this is satisfied to first approximation and we can assume a well-posed problem: Compute the q.c. mapping f associated to the Beltrami differential defined by equation 3.2.31 from g. This can be done with methods from computational quasi-conformal geometry (cf. section 2.5). The choice of the concrete algorithm for computing f depends on the concrete topology of S. The implementation of such an algorithm for narrow strips will be the topic of future work.

Summary: For general areas $S \subset \mathbb{S}^2$ of the celestical sphere the lens mapping cannot be descriped as a well-defined q.c. mapping on S with Beltrami differential given by the reduced shear map g on S. Only in the limit $\epsilon \to 0$ the corresponding compatibility equations are fullfilled. However, if S is a narrow strip with extension along one degree of latitude, it can be modelled using the flat-sky approximation as Riemann surface and to first approximation we obtain a well-defined Beltrami differential and q.c. mapping f on S. f is in principle computable by methods from computational quasi-conformal geometry. So in the case of a narrow strip we have an analogous situation to the planar case and can calculate the lens mapping f directly from the reduced shear map g.

Outlook: At first glance, it is surprising that a narrow strip with extension along one degree of longitude instead of latitude cannot be modeled in this way. Actually, we have proven this algebraically above and forced by the choice of coordinates on the celestical sphere, but differential geometry is independent of the choice of coordinates. So what distinguishes the east-west direction from the north-south direction? We think it is the concrete choice of the prime meridian, which breaks the spherical symmetry and selects a preferred direction. If one measures the reduced shear field on a "tilted" strip in north-south direction, one simply has to tilt the north pole or the zero meridian by $90°$. This allows us to consider the strip as one in east-west direction and model it accordingly.

As the above modeling of the lens mapping f as q.c. mapping is applicable for arbitrary narrow strips on the celestical sphere, a further question arises: Is it possible to compute f on a general area S of the celestical sphere by reducing it to the computation of f on narrow strips, which overlap S? On each narrow strip the restriction of f can then be modelled as a q.c. mapping. On regions, where two strips overlap, the two restrictions of f should then coincide. However, the main problem here are the boundary values that one must assume when calculating f on each strip, and which one generally does not know.

4 Results and Discussion

We first show the validity of algorithm 1 and the implementation described in section 3.1 by considering two lenses for which one can give analytical expressions for the lens mapping and the reduced shear. We then consider actual shear fields and apply our algorithm to them.

4.1 Schwarzschild Lens

As already mentioned in chapter 2 for the case of the Schwarzschild lens we obtain for the lens mapping

$$f(z) = z - \frac{1}{\bar{z}} = x + \mathrm{i}y - \frac{1}{x - \mathrm{i}y} = x\left(1 - \frac{1}{x^2 + y^2}\right) + \mathrm{i}y\left(1 - \frac{1}{x^2 + y^2}\right) = u(x, y) + \mathrm{i}v(x, y), \qquad (4.1.1)$$

and for the Beltrami coefficient

$$-g(z) = \mu(z) = \frac{1}{\bar{z}^2} = \frac{1}{(x - \mathrm{i}y)^2} = \frac{x^2 - y^2}{(x^2 + y^2)^2} + \mathrm{i}\frac{2xy}{(x^2 + y^2)^2} = \rho(x, y) + \mathrm{i}\tau(x, y). \qquad (4.1.2)$$

4.1.1 Dirichlet Boundary Conditions

For both real and imaginary part, we first assume Dirichlet boundary conditions, which follow directly from equation 4.1.1. We compute u^n and v^n using algorithm 1 for different resolutions n from $n = 3$ to $n = 8$. As shown in figure 15, for $n = 7$, i.e. $2^7 = 128$ cells per coordinate direction, we obtain an almost complete agreement between actual and calculated lens mapping.
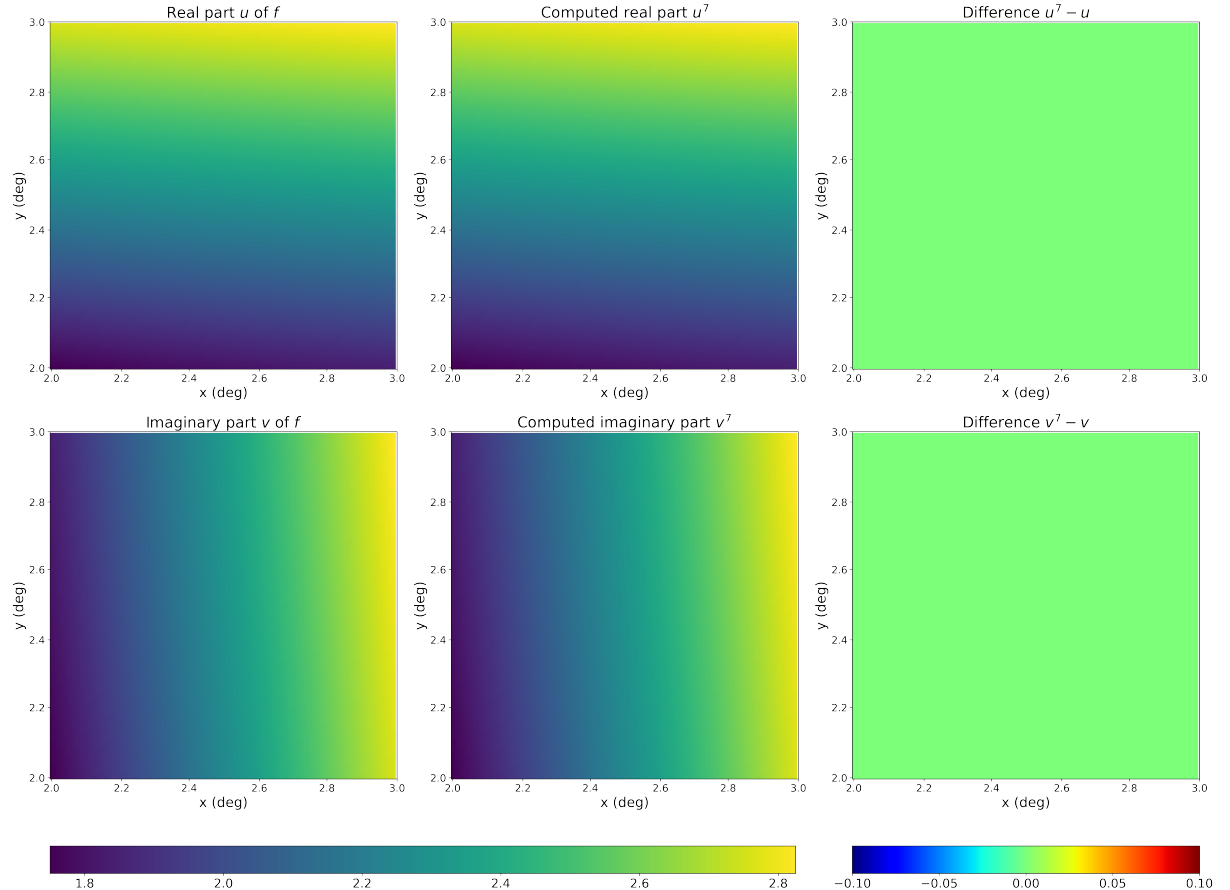

Figure 15: Schwarzschild lens: Comparison between actual lens mapping $f = u + \mathrm{i}v$ and calculated lens mapping $f^7 = u^7 + \mathrm{i}v^7$ with algorithm 1 for a resolution of $n = 7$ and Dirichlet boundary conditions.

Here, the coordinate system was chosen such that the point $(0,0)$ coincides with the position of the point mass in the lens plane. Additionally, we assumed our field of view Ω to be the square $\{z = x + iy \mid 2° \leq x, y \leq 3°\}$, such that we are in the weak lensing regime and cross no critical curve. As shown in figure 16, the deviation between real and calculated lens mapping can also be quantified by plotting the L_2 and H_1 error against each refinement order n, where

$$e^n_{L_2,w} = \|w - w^n\|_{L_2} = \left(\int_\Omega (w(z) - w^n(z))^2 \, dz\right)^{\frac{1}{2}} = \left(\sum_{K \in \mathcal{T}_{n(h)}} \sum_q w_q \left(w(z_q) - w^n(z_q)\right)^2 |\det(A_K)| d\hat{z}\right)^{\frac{1}{2}}, \quad (4.1.3)$$

$$e^n_{H_1,w} = \|\nabla(w - w^n)\|_{L_2} = \left(\int_\Omega |\nabla w(z) - \nabla w^n(z)|^2 dz\right)^{\frac{1}{2}} = \left(\sum_{K \in \mathcal{T}_{n(h)}} \sum_q w_q \left(\nabla w(z_q) - \nabla w^n(z_q)\right)^2 |\det(A_K)| d\hat{z}\right)^{\frac{1}{2}},$$
$$(4.1.4)$$

with $w \in \{u, v\}$. The errors $e^n_{L_2,w}$ and $e^n_{H_1,w}$ are independent of whether u or v is chosen for w.
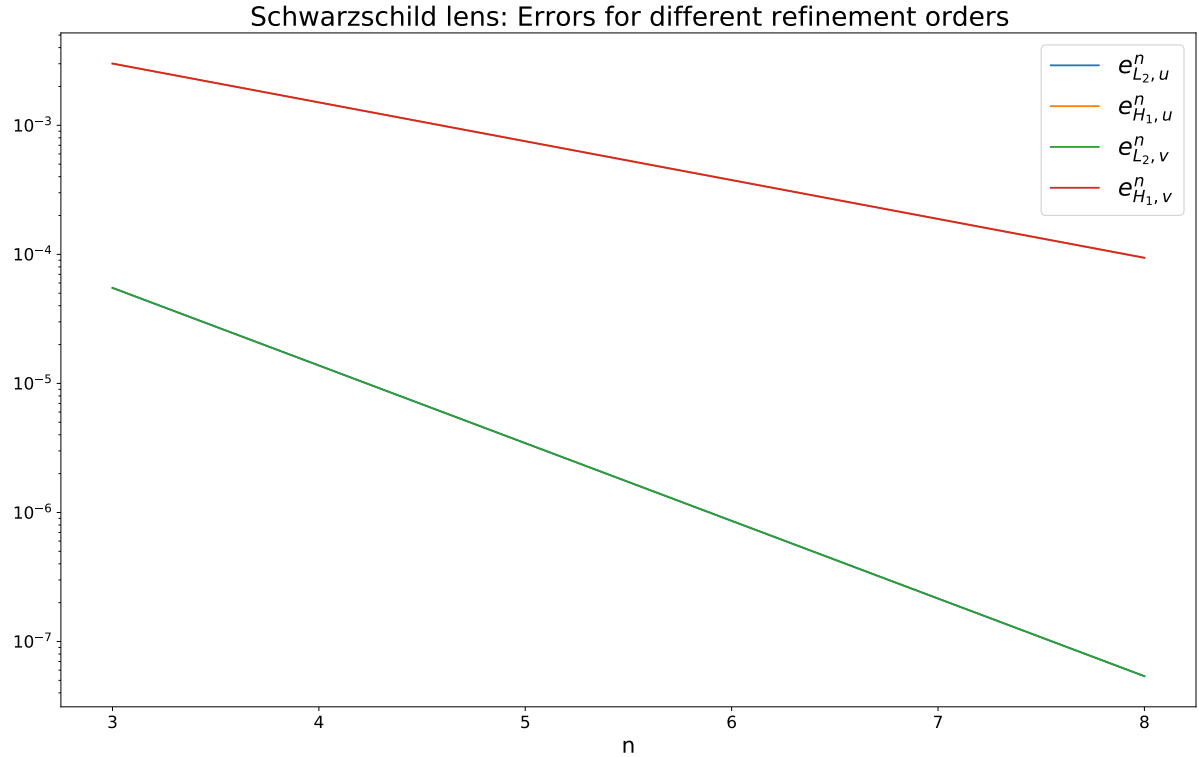
Figure 16: Schwarzschild lens error: L_2 and H_1 errors for different refinement orders with Dirichlet boundary conditions. The orange and red lines overlap, as well as the green and blue line.

As can be seen, the error $e^n_{L_2,w}$ decreases quadratically with increasing refinement order n, while the error $e^n_{H_1,w}$ decreases linearly with n. This behavior holds equally for u and v. This is just the statement of our a priori error estimation in chapter 3 (cf. equation 3.1.49)!

4.1.2 Neumann Boundary Conditions

We now want to do the same with Neumann boundary conditions. As directional derivatives we obtain

$$\frac{\partial u}{\partial \boldsymbol{n}} = \frac{\partial u}{\partial x} n_1 + \frac{\partial u}{\partial y} n_2 = \left(1 + \frac{x^2 - y^2}{(x^2 + y^2)^2}\right) n_1 + \frac{2xy}{(x^2 + y^2)^2} n_2 \simeq n_1, \quad (4.1.5)$$

and

$$\frac{\partial v}{\partial \boldsymbol{n}} = \frac{\partial v}{\partial x}n_1 + \frac{\partial v}{\partial y}n_2 = \frac{2xy}{(x^2+y^2)^2}n_1 + \left(1 - \frac{x^2-y^2}{(x^2+y^2)^2}\right)n_2 \simeq n_2. \qquad (4.1.6)$$

The normal vector $\boldsymbol{n} = (n_1, n_2)$ is given by $(0, -1)$, $(0, 1)$, $(-1, 0)$ or $(1, 0)$ depending on the part of $\partial\Omega$. Since we do not know the normal derivatives for actual data, we have made appropriate approximations for u and v right above to validate our implementation for actual data using an example whose solution we know. When only Neumann boundary conditions are applied, $w \in \{u, v\}$ is only determined up to a constant c by the above equations. An additional constraint is thus required, e.g.:

$$\int_\Omega w \mathrm{d}z = 0. \qquad (4.1.7)$$

Unfortunately we could not physically motivate such an assumption. Therefore, for the real part we assume Dirichlet boundary conditions on the left side of $\partial\Omega$ and on the rest of $\partial\Omega$ Neumann boundary conditions. Conversely, for the imaginary part Dirichlet boundary conditions were assumed on the bottom part of $\partial\Omega$. In this way one obtains the following results:
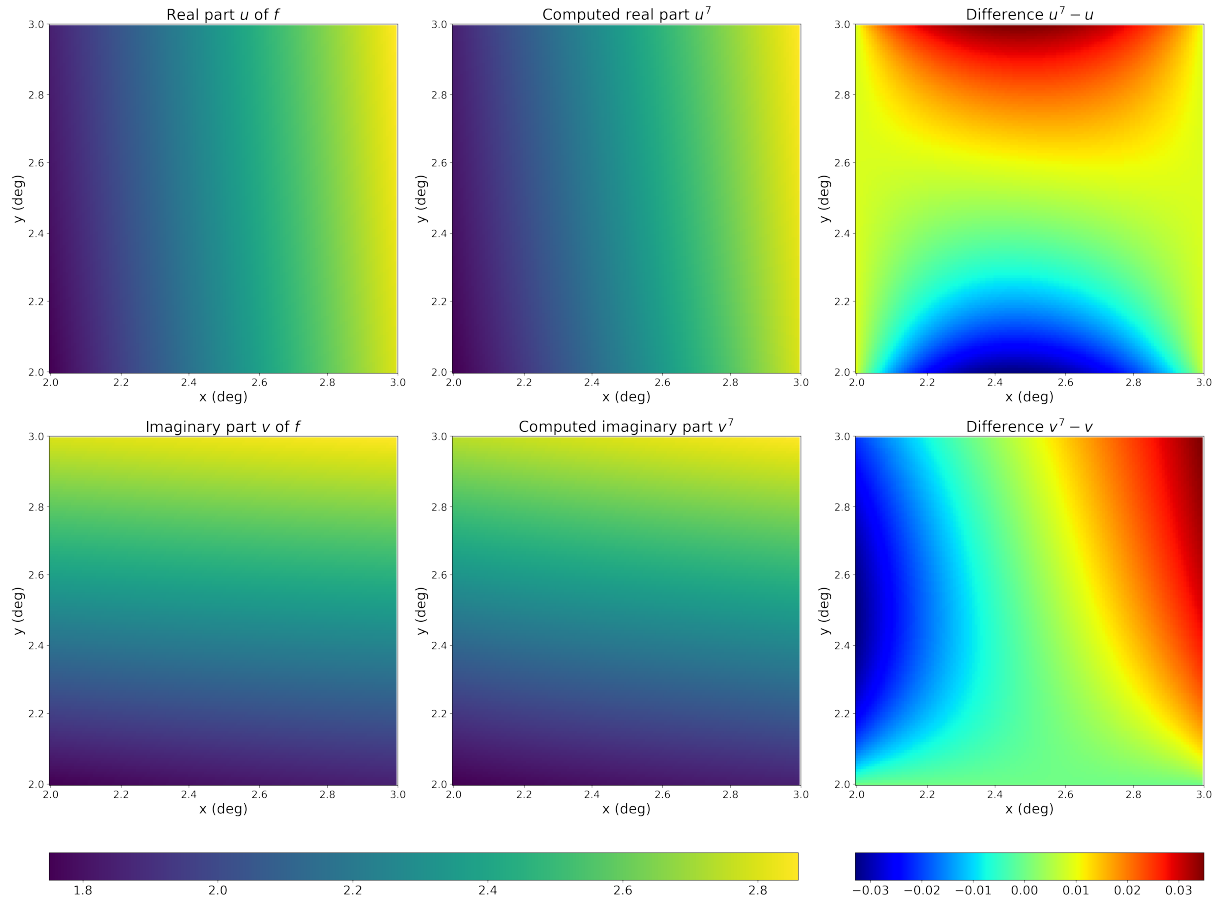
Figure 17: Schwarzschild lens: Comparison between actual lens mapping $f = u + \mathrm{i}v$ and calculated lens mapping $f^7 = u^7 + \mathrm{i}v^7$ with algorithm 1 for a resolution of $n = 7$ and Neumann boundary conditions on three boundary parts.

As expected, actual and calculated lens mapping agree at the edges for which Dirichlet boundary conditions have been assumed. Perfect agreement is also obtained in the middle of Ω. The deviation increases the closer one gets to the edges for which one has assumed Neumann boundary conditions and which are adjacent to the left and right side of $\partial\Omega$, respectively. In general, however, the deviations are small compared to the actual values of f (order of magnitude $O(10^{-2})$ versus $O(10^1)$). Thus, our above approx-

imation seems to give a valid result that deviates only slightly from the actual lens mapping!

However, since we are now computing the solution to a slightly perturbed problem, our a priori estimation, which was satisfied for the case of Dirichlet boundary conditions, no longer holds. That is the reason why the errors $e^n_{L_2,w}$ and $e^n_{H_1,w}$ change only slightly for different refinement orders n (cf. figure 18). Refining the mesh width does not reduce the difference between f^n and f. However, the larger n, the better the results for quantities derived from f^n are, such as γ^n or κ^n: The errors arising from the discretization of the first derivatives of f^n become smaller as n increases.

Figure 18: Schwarzschild lens error: L_2 and H_1 errors for different refinement orders with approximated Neumann boundary conditions on three boundary parts.

4.2 Singular Isothermal Lens

For the singular isothermal lens we obtain for the lens mapping

$$f(z) = z - \frac{z}{|z|} = x + \mathrm{i}y - \frac{x + \mathrm{i}y}{\sqrt{x^2 + y^2}} = x\left(1 - \frac{1}{\sqrt{x^2 + y^2}}\right) + \mathrm{i}y\left(1 - \frac{1}{\sqrt{x^2 + y^2}}\right) = u(x,y) + \mathrm{i}v(x,y),$$

(4.2.1)

and for the Beltrami coefficient

$$-g(z) = \mu(z) = \frac{z^2}{2|\bar{z}|^3 - |\bar{z}|^2} = \frac{\left(x^2 - y^2\right)}{2\left(x^2 + y^2\right)^{\frac{3}{2}} - \left(x^2 + y^2\right)} + \mathrm{i}\frac{2xy}{2\left(x^2 + y^2\right)^{\frac{3}{2}} - \left(x^2 + y^2\right)} = \rho(x,y) + \mathrm{i}\tau(x,y).$$

(4.2.2)

As for the Schwarzschild lens, the coordinate system was chosen such that the point $(0,0)$ coincides with the position of the point mass in the lens plane. Also, we assume our field of view Ω to be the square $\{z = x + \mathrm{i}y \mid 2 \leq x, y \leq 3\}$, such that we are in the weak lensing regime and cross no critical curve. Under the assumption of Dirichlet boundary conditions on all parts of $\partial\Omega$ we obtain similiar results as for the Schwarzschild lens:
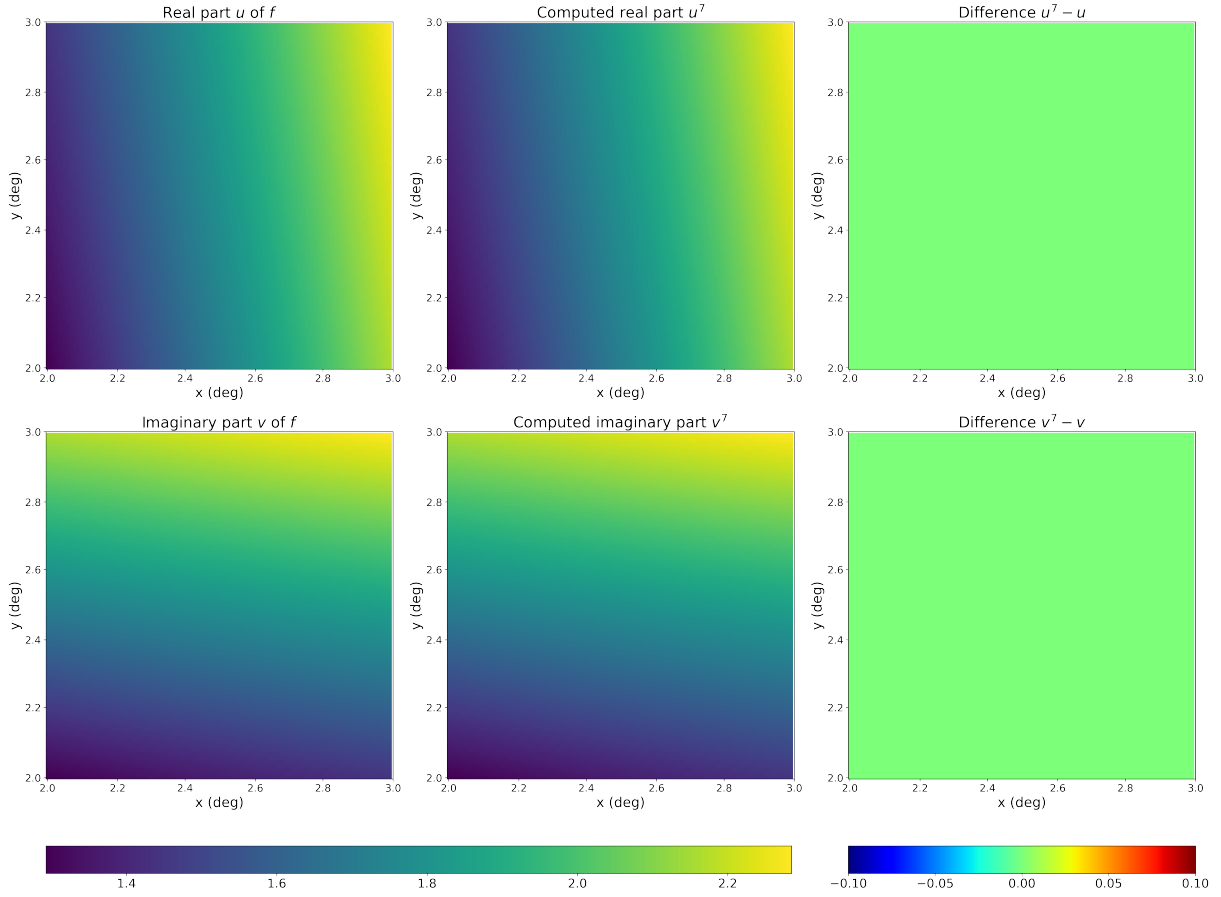
Figure 19: Singular isothermal lens: Comparison between actual lens mapping $f = u + \mathrm{i}v$ and calculated lens mapping $f^7 = u^7 + \mathrm{i}v^7$ with algorithm 1 for a resolution of $n = 7$ and Dirichlet boundary conditions.
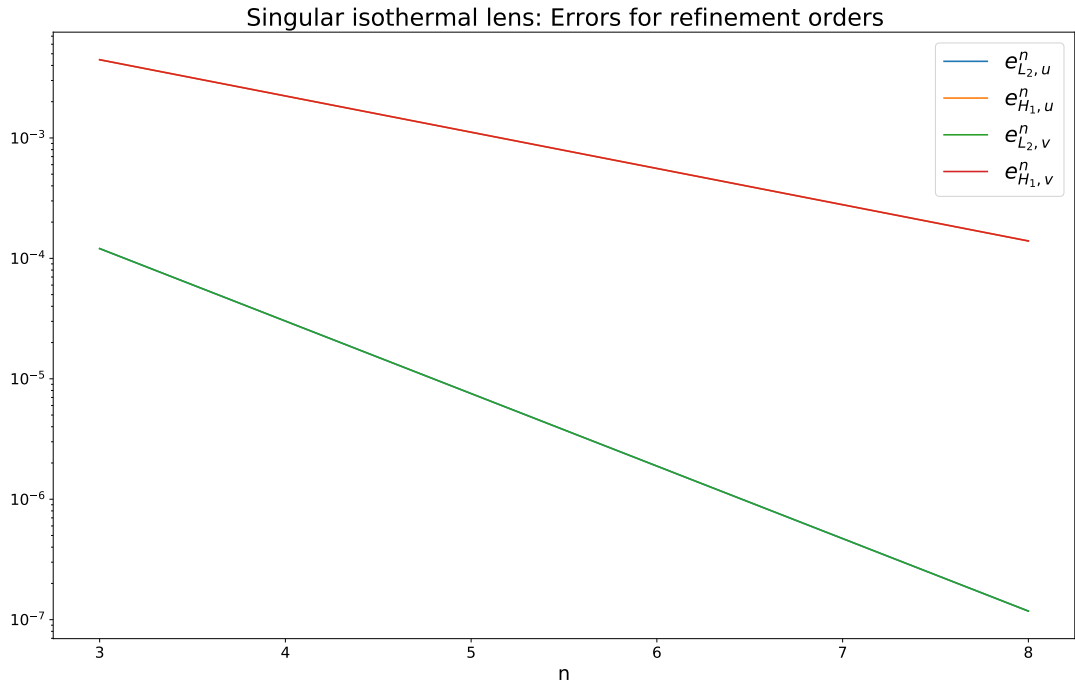

Figure 20: Singular isothermal lens error: L_2 and H_1 errors for different refinement orders with Dirichlet boundary conditions. The orange and red lines overlap, as well as the green and blue line.

4.3 Actual Data

We now want to apply algorithm 1 to situations that are closer to actual applications. Constructing a convergence map of a particular subfield from a shear catalog is an operation that occurs frequently in weak lensing analysis: If the field of view is unmasked, the reconstruction operation is equivalent to the calculation of the E mode of the shear field γ [3]. Suppose that the shear information is contained in the two files 'shear1.fits' and 'shear2.fits'. Using the Python library LensTools [4] we compute the convergence out of the shear information. This allows us to reconstruct the reduced shear field g, apply algorithm 1 to it and compare the obtained results for γ and κ with the actual fields.

4.3.1 Comparison with Actual Data

For a fixed refinement order of $n = 7$ we compute the lens mapping f^7 out of the reduced shear field g shown in figure 21. This is done assuming first Dirichlet and then Neumann boundary conditions. The field of view Ω is the square $\{z = x + iy \mid 0° \leq x, y \leq 3.4641°\}$.
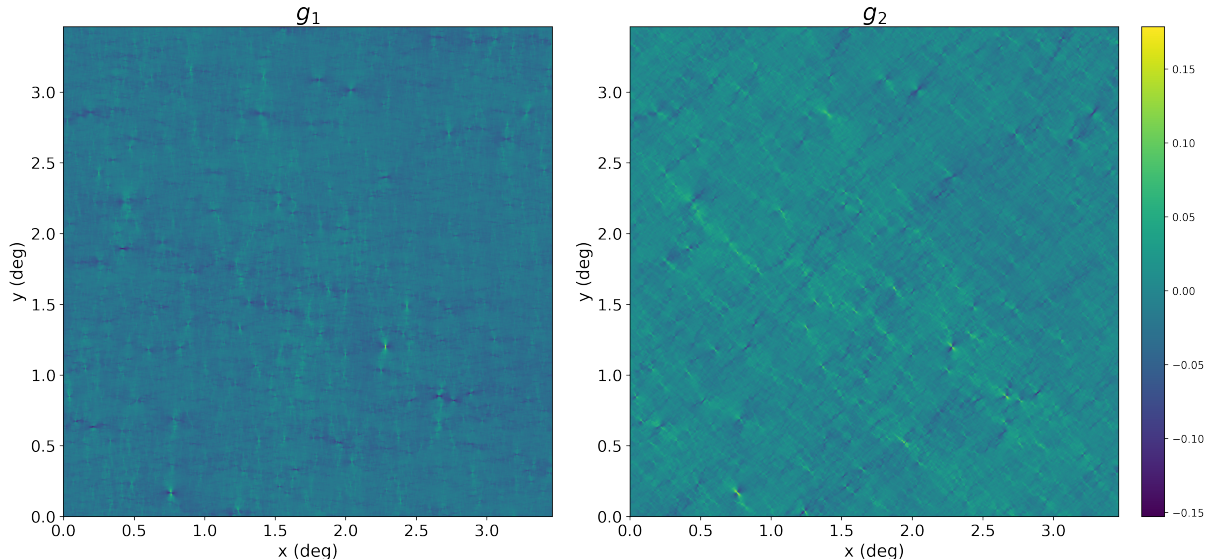
Figure 21: Reduced shear $g = g_1 + ig_2 = -\mu$ as input for algorithm 1

Dirichlet Boundary Conditions: In the calculation of f^7 using *HiFlow³* we first assume Dirichlet boundary conditions from equation 3.1.66 on all four parts of $\partial\Omega$. Therefore, we made the assumption that the deflection field α vanishes on all boundary parts. After calculation, we export the lens mapping f^7 as CSV file and read it into a 2d array in Python for further evaluation. The deflection field α^7 can then be calculated point by point from the lens mapping using the relation

$$\alpha^7(z) = z - f^7(z). \tag{4.3.1}$$

The computed lens mapping f^7 is shown in figure 22 and the deflection field α^7 derived from f^7 in figure 23 on the next page. As expected, the values for α_1 and α_2 are distributed around 0. The deflection is small and in the arcsecond range.

---

[3]More on that topic can be found under https://lenstools.readthedocs.io.
[4]The source code can be found under https://github.com/apetri/LensTools.
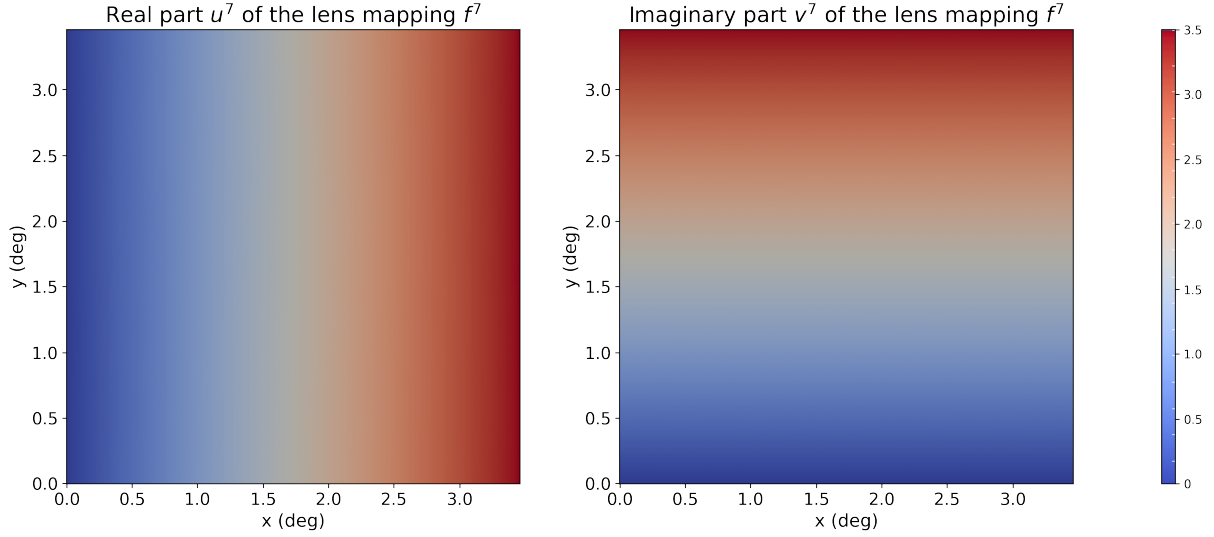
Figure 22: Computed lens mapping $f^7 = u^7 + iv^7$ with algorithm 1 for a resolution of $n = 7$ and Dirichlet boundary conditions on all four boundary parts. Figures created with ParaView.
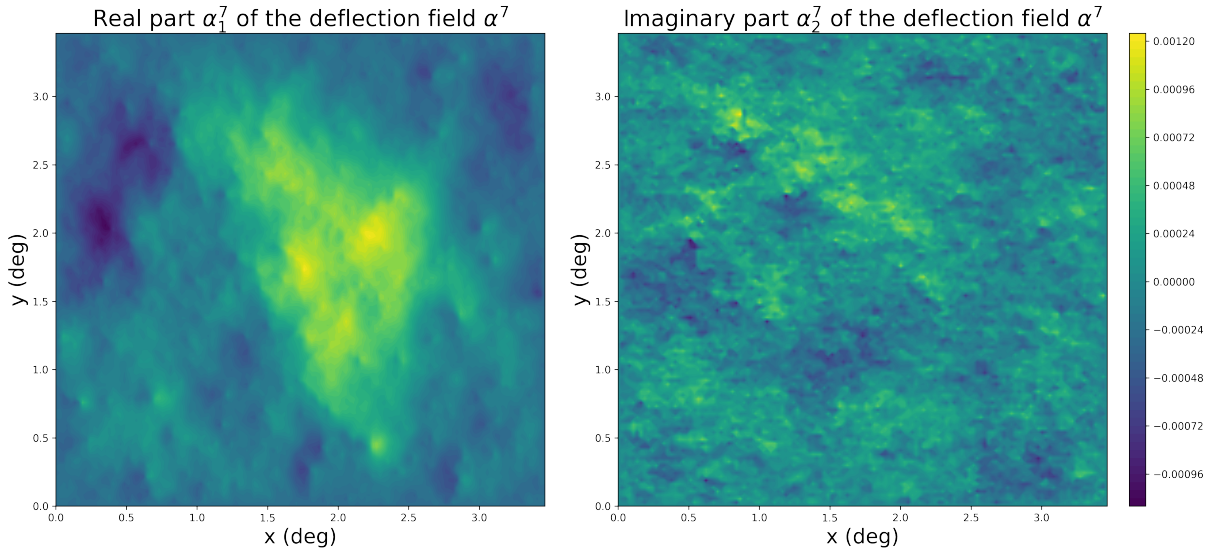

Figure 23: Computed deflection field $\alpha^7 = \alpha_1^7 + i\alpha_2^7$ with algorithm 1 for a resolution of $n = 7$ and Dirichlet boundary conditions on all four boundary parts.

With α^7 we can (re-)calculate the reduced shear field g^7 and compare it to our actual one. This is done using the central difference operators δ_{2x}^n and δ_{2y}^n introduced in chapter 3.1.3:

$$g^n = g_1^n + ig_2^n = \frac{\delta_{2x}^n \alpha_1 - \delta_{2y}^n \alpha_2}{2 - (\delta_{2x}^n \alpha_1 + \delta_{2y}^n \alpha_2)} + i\frac{\delta_{2y}^n \alpha_1 + \delta_{2x}^n \alpha_2}{2 - (\delta_{2x}^n \alpha_1 + \delta_{2y}^n \alpha_2)}. \tag{4.3.2}$$

As we compute our solution for a refinement order of $n = 7$, the corresponding mesh width $h(n)$ is equal to $h(n) = 3.4641/2^7 \approx 0.027$. The resulting g^7 together with a comparison to the actual reduced shear field g is shown in figure 24 on the next page.
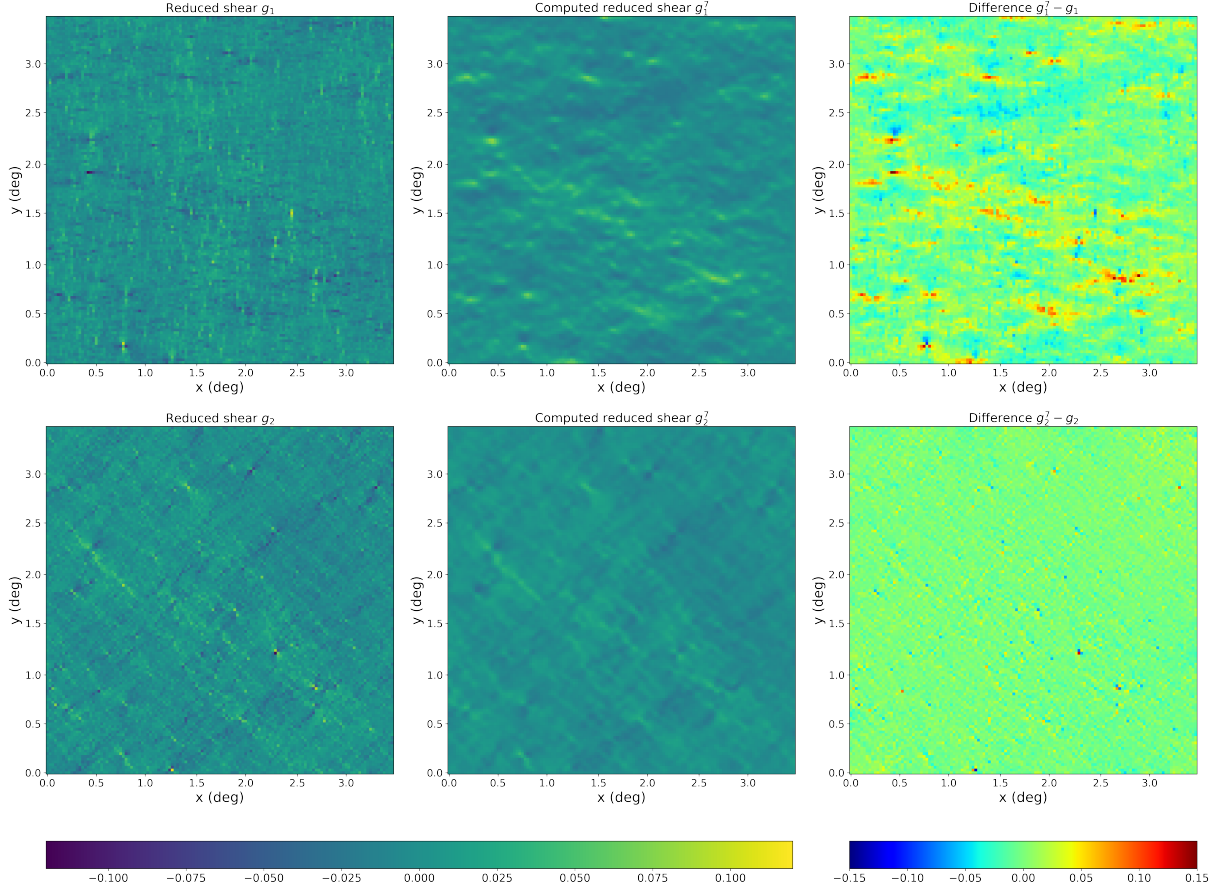
Figure 24: Actual data: Comparison between actual reduced shear field $g = g_1 + ig_2$ and calculated reduced shear field $g^7 = g_1^7 + ig_2^7$ with algorithm 1 for a resolution of $n = 7$ and Dirichlet boundary conditions on all four boundary parts.

With a few exceptions, the deviation between g_2^7 and g_2 is of the order $O(10^{-4})$ to $O(10^{-3})$ resulting mainly from the lower resolution used in the computation of g_2^7 compared to g_2: The reduced shear field g has $2^{11} = 2048$ cells per coordinate direction, while f^7 respecively g^7 is computed on a grid having only $2^7 = 128$ cells per direction! This occasionally leads to high deviations, whenever g changes significantly on small scales. The effect is especially important for the calculation of g_1. The deviations between g_1^7 and g_1 are considerable here and up to the order $O(10^{-1})$. There is a second reason why g_1^7 and g_1 coincide so badly: Obviously the assumption that the deflection field vanishes at the boundaries is not or not sufficiently justified. For instance, as we will see below, we get much better results for g_1 under the assumption of Neumann boundary conditions. Before we get to that, let us compare the calculated quantities γ^7 and κ^7 with the actual fields γ and κ. For this we use the central difference operator again:

$$\gamma^7 = \gamma^1 + i\gamma^2 = \frac{1}{2}\left(\delta_{2x}^n \alpha_1 - \delta_{2y}^n \alpha_2\right) + \frac{i}{2}\left(\delta_{2y}^n \alpha_1 + \delta_{2x}^n \alpha_2\right), \tag{4.3.3}$$

$$\kappa^7 = \frac{1}{2}\left(\delta_{2x}^n \alpha_1 + \delta_{2y}^n \alpha_2\right). \tag{4.3.4}$$

Figure 25 shows the calculated γ^7 together with a comparison to the acutal shear field γ, and figure 26 accordingly for κ.
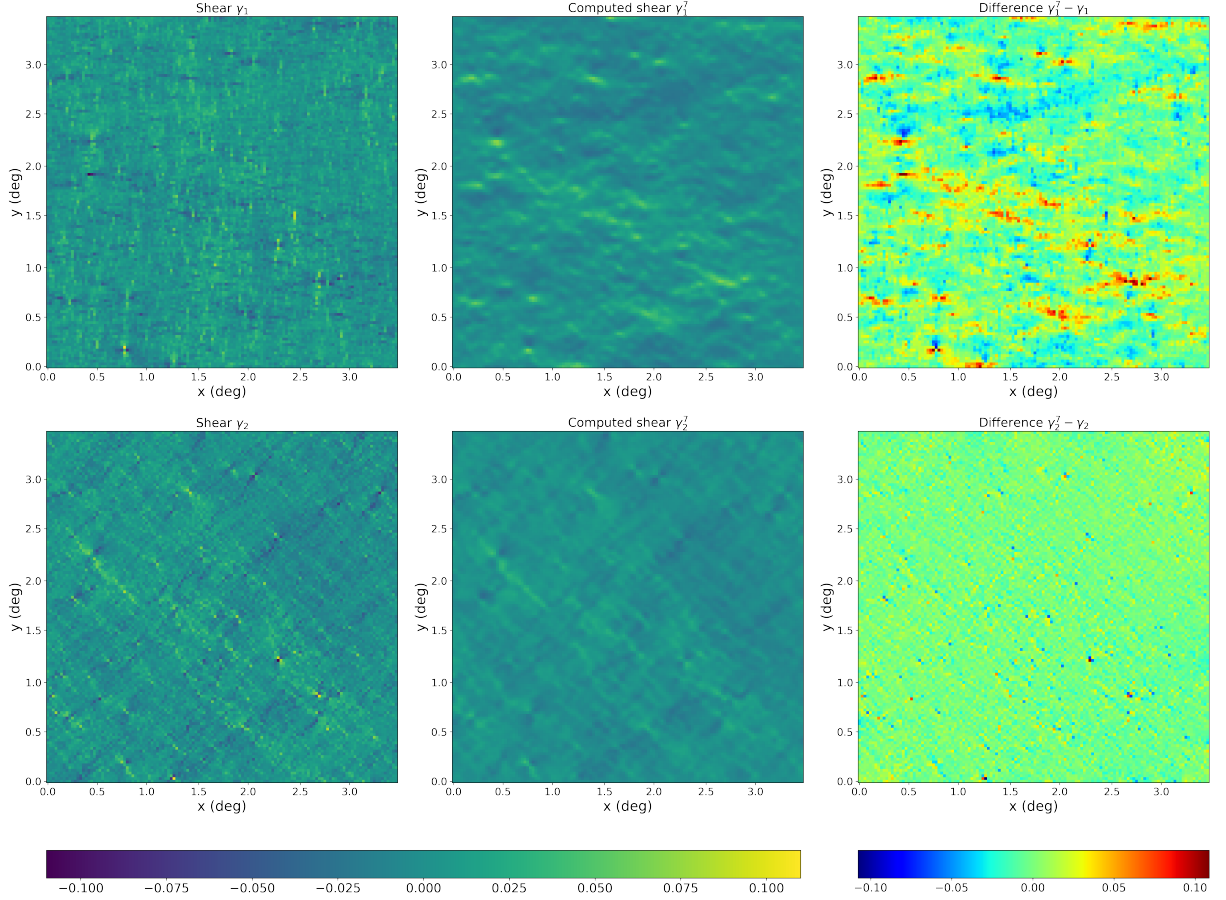
Figure 25: Actual data: Comparison between actual shear field $\gamma = \gamma_1 + i\gamma_2$ and calculated reduced shear field $\gamma^7 = \gamma_1^7 + i\gamma_2^7$ with algorithm 1 for a resolution of $n = 7$ and Dirichlet boundary conditions on all four boundary parts.
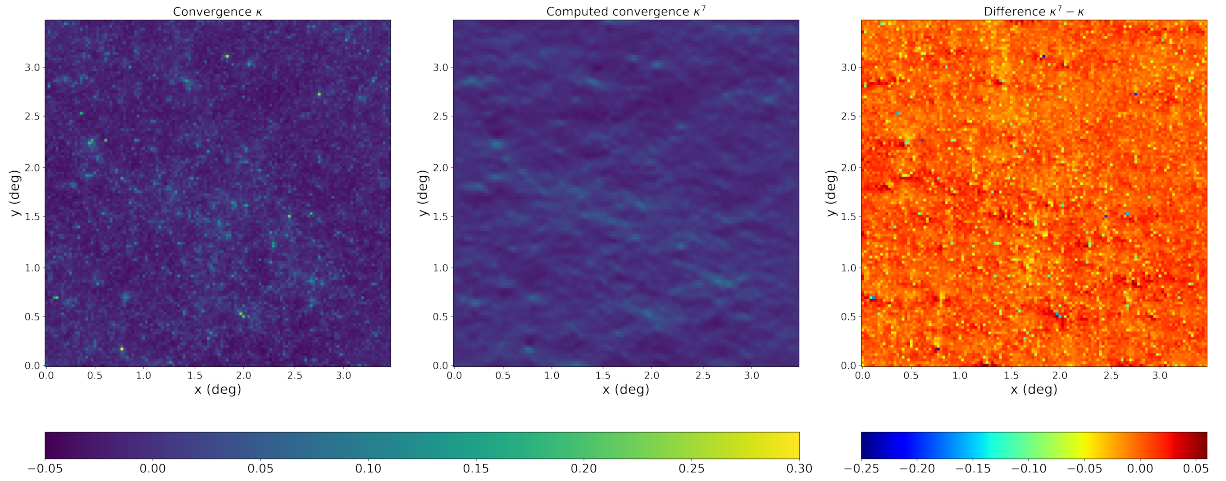

Figure 26: Actual data: Comparison between actual convergence field κ and calculated convergence field κ^7 with algorithm 1 for a resolution of $n = 7$ and Dirichlet boundary conditions on all four boundary parts.

Like g_1^7, γ_1^7 deviates significantly from the actual shear field γ_1 in many regions. Regions with high shear values are significantly more extensive than is actually the case. In contrast, one obtains for γ_2 analogously to g_2 an agreement between γ^7 and γ of the order $O(10^{-3})$ to $O(10^{-2})$ apart from a few

exceptions. The same also holds for κ. However, the strong deviations at those points where γ_2 and κ have high positive values are striking. This is particularly well apparent from the blue spots in the right image of figure 26. The reason for the high deviation at these points was already explained above in the discussion of the computed reduced shear. It results from the significantly lower resolution used for the computation of f^7 compared to the resolution of the actual shear and convergence fields.

Neumann Boundary Conditions: We want to investigate whether other boundary conditions are more suitable to obtain better results for γ and κ. Therefore, we assume (approximated) Neumann boundary conditions on all four parts of $\partial\Omega$. As mentioned in chapter 4.1.2 the calculated lens mapping f^7 is then undetermined up to a constant c. Since we are mainly interested in the derived quantities from f^7 as κ^7 and γ^7, we ignore this circumstance. In our calculation we assume $\frac{\partial f}{\partial \boldsymbol{n}} = 0$ on the left and right part of the boundary and $\frac{\partial f}{\partial \boldsymbol{n}} = 1$ on the top and bottom part. The lens mapping f^7 computed in this way is shown in figure 27 and the corresponding deflection field α^7 in figure 28.
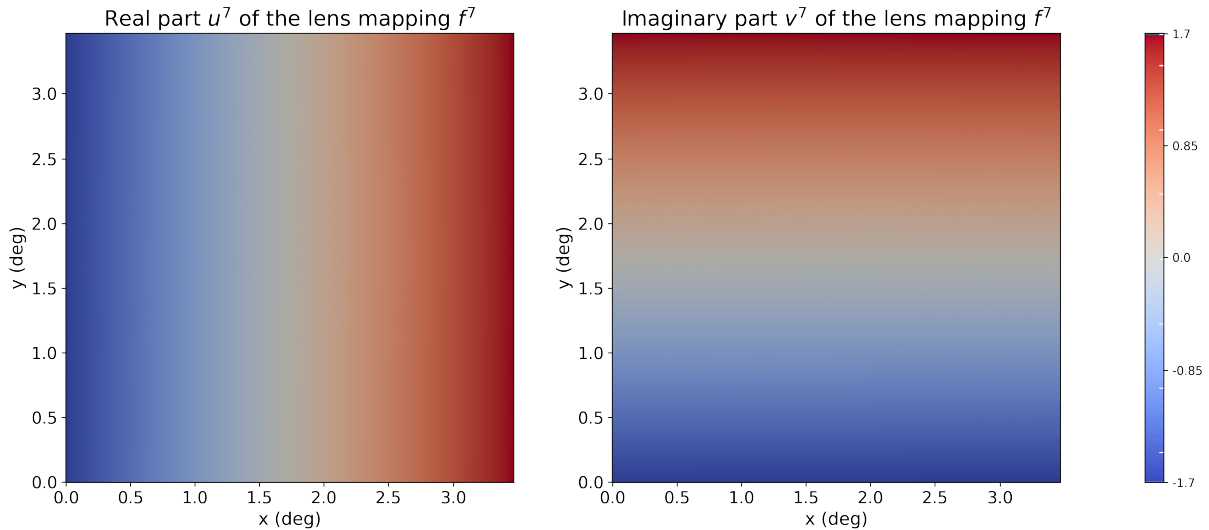
Figure 27: Computed lens mapping $f^7 = u^7 + \mathrm{i}v^7$ with algorithm 1 for a resolution of $n = 7$ and (approximated) Neumann boundary conditions on all four boundary parts. Figures created with ParaView.
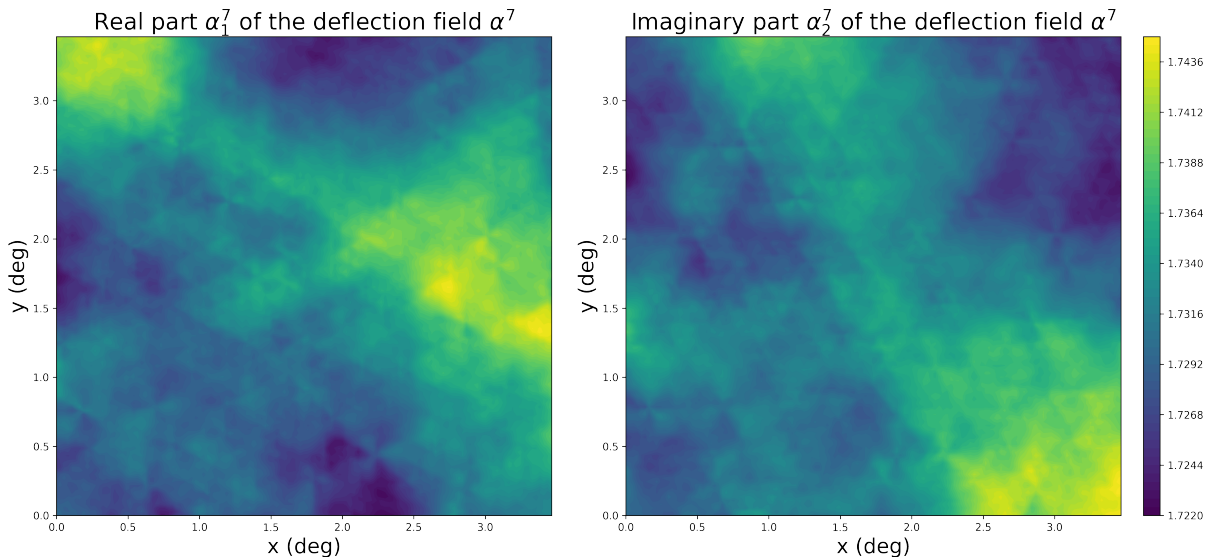

Figure 28: Computed deflection field $\alpha^7 = \alpha_1^7 + \mathrm{i}\alpha_2^7$ with algorithm 1 for a resolution of $n = 7$ and (approximated) Neumann boundary conditions on all four boundary parts.

As one can see, the values for α_1 and α_2 are distributed around 1.73. They are too large and all strictly positive! Instead, one would assume that they are distributed around 0 as in the case of Dirichlet boundary conditions. This is just the indefiniteness of the approximated solution f^7 up to a constant, which comes from the Neumann boundary conditions. Analogous to the case of Dirichlet boundary conditions we (re-)construct the reduced shear field g^7 and compare it to g as shown in figure 29.
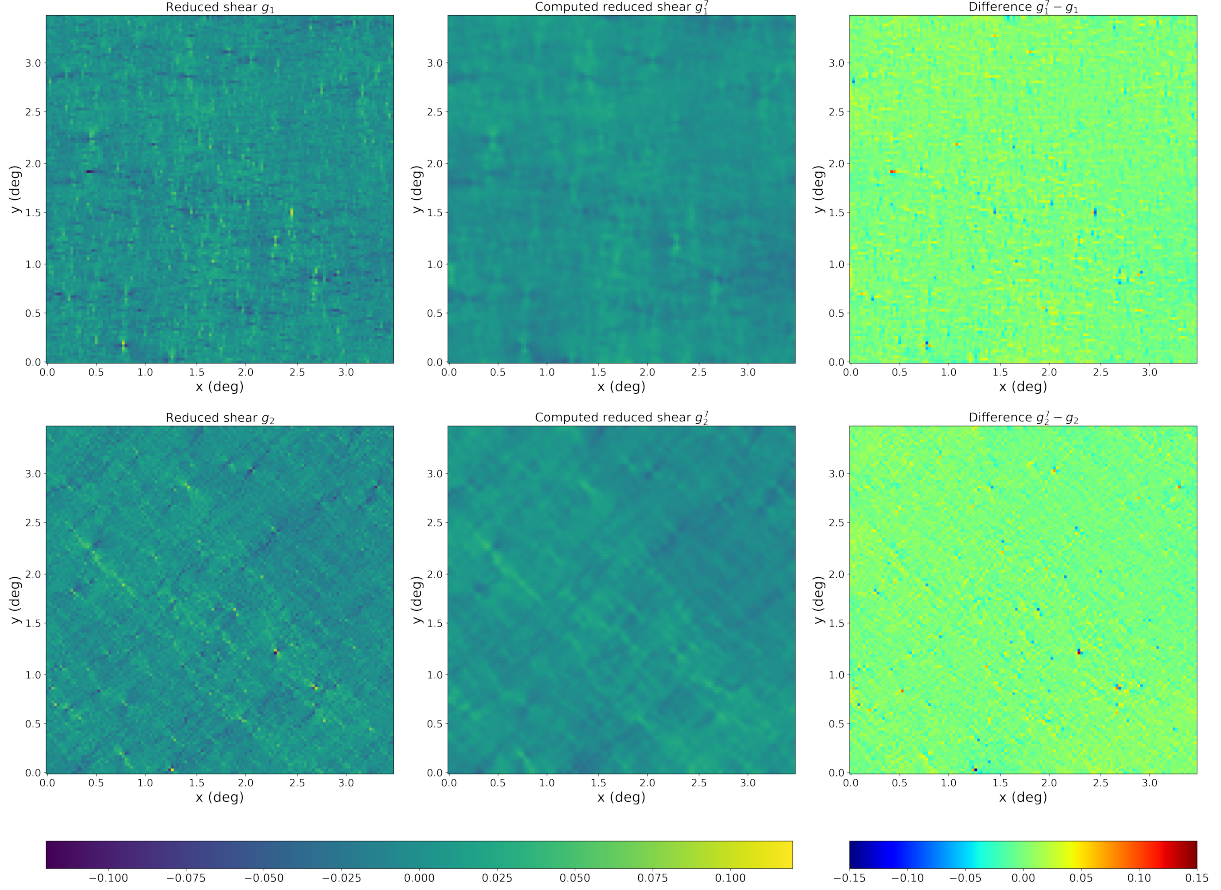
Figure 29: Actual data: Comparison between actual reduced shear field $g = g_1 + ig_2$ and calculated reduced shear field $g^7 = g_1^7 + ig_2^7$ with algorithm 1 for a resolution of $n = 7$ and (approximated) Neumann boundary conditions on all four boundary parts.

In contrast to Dirichlet boundary conditions one obtains now not only for g_2 but also for g_1 an agreement between g_1^7 and g_1 of the order $O(10^{-4})$ to $O(10^{-3})$. If larger deviations occur, they are isolated and can be explained as before by the resolution of $n = 7$ used in the calculation.

Accordingly, a much better agreement between γ_1^7 and γ_1 is also obtained for γ_1, as can be seen in figure 30 on the next page. The deviation between the calculated γ_1^7 and actual γ_1 here are broadly of the order $O(10^{-4})$ to $O(10^{-3})$. The same applies for γ_2. For κ, the deviation is of the order $O(10^{-2})$ in regions with high κ values, as already for the case of Neumann boundary conditions. Thus, the assumption of (approximated) Neumann boundary conditions leads to significantly better results especially for γ_1, while no significant improvements are obtained for γ_2 and κ.
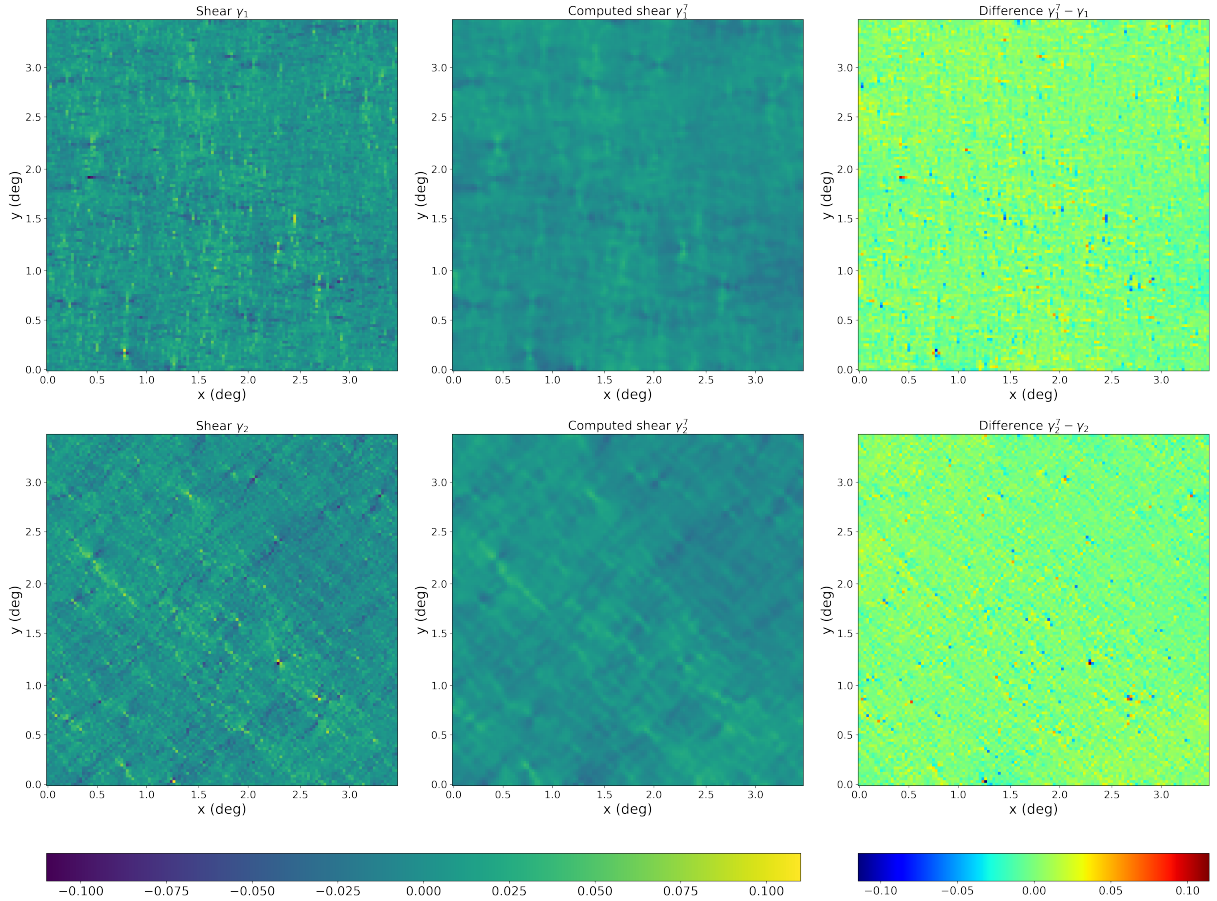
Figure 30: Actual data: Comparison between actual shear field $\gamma = \gamma_1 + i\gamma_2$ and calculated reduced shear field $\gamma^7 = \gamma_1^7 + i\gamma_2^7$ with algorithm 1 for a resolution of $n = 7$ and Neumann boundary conditions on all four boundary parts.
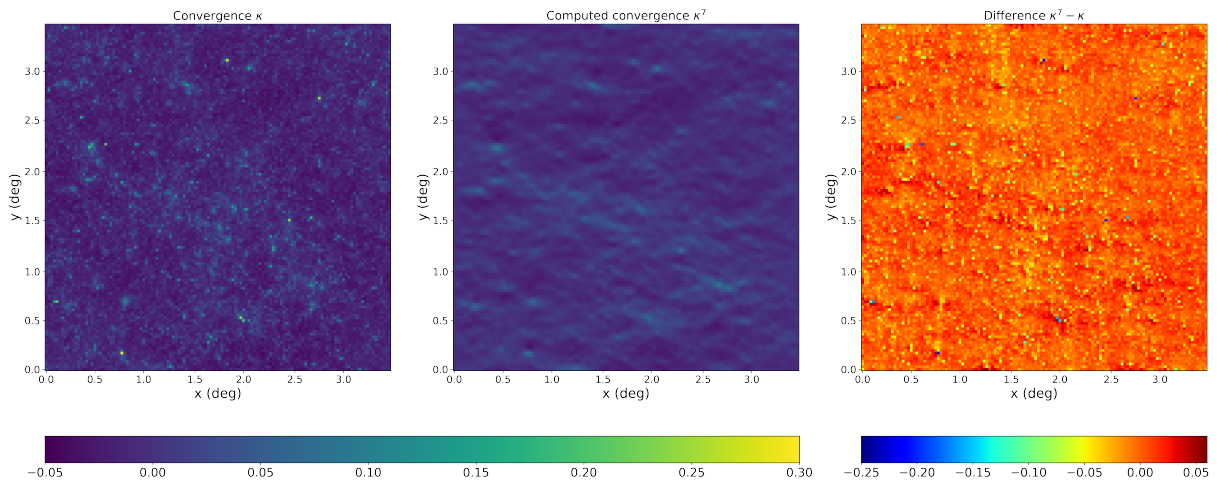

Figure 31: Actual data: Comparison between actual convergence field κ and calculated convergence field κ^7 with algorithm 1 for a resolution of $n = 7$ and Neumann boundary conditions on all four boundary parts.

4.4 Comparison with the KS 93 Algorithm

Finally, we want to compare our proposed algorithm with algorithm 2 and 3. As input data we choose the reduced shear field g shown in figure 32. First we compute the convergence κ out of g using algorithm 1. Then we assume $\gamma \approx g$, and compute κ by means of algorithm 2. The result is shown in figure 33. We also compute κ from g directly using the extension of the KS 93 algorithm to the non-linear regime (algorithm 3). The result of this computation can be found in figure 34 and a comparison between the computation with algorithm 2 and 3 in figure 35.
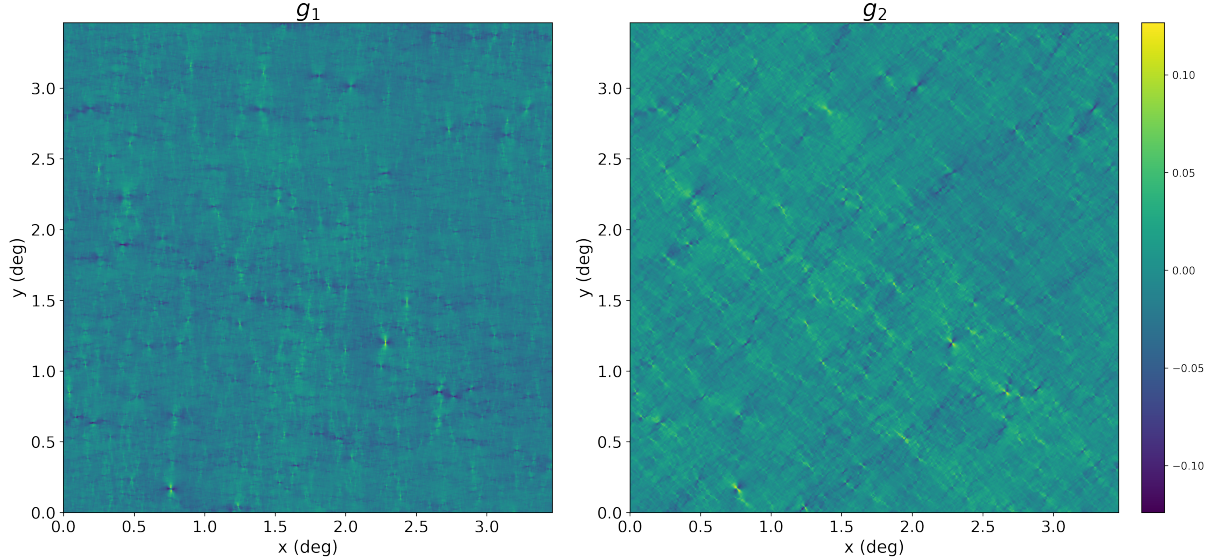
Figure 32: Reduced shear $g = g_1 + \mathrm{i}g_2 = -\mu$ as input for algorithm 1
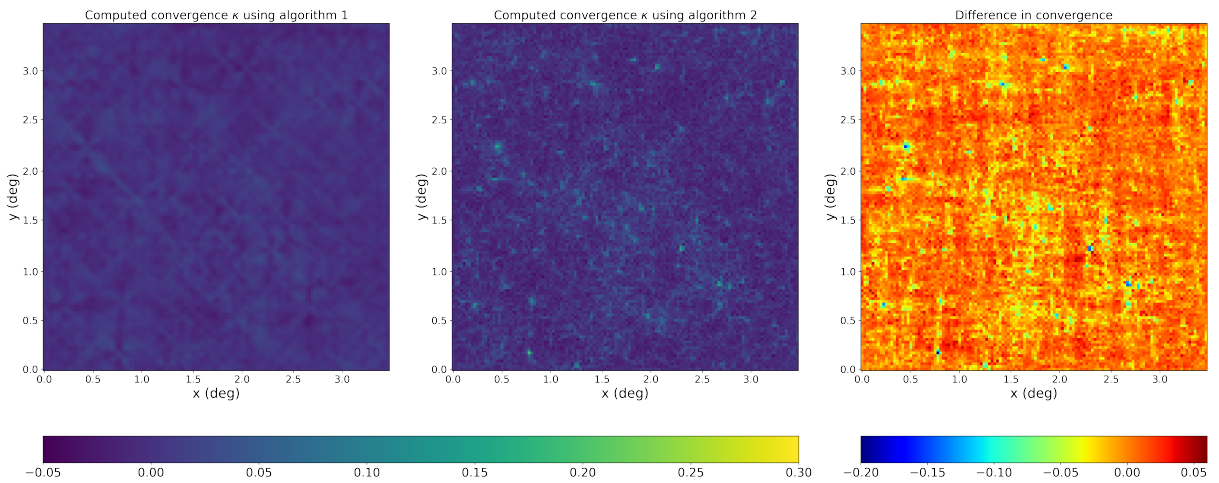
Figure 33: Comparison between the convergence fields computed with algorithm 1 assuming Neumann boundary conditions on all four boundary parts and algorithm 2.
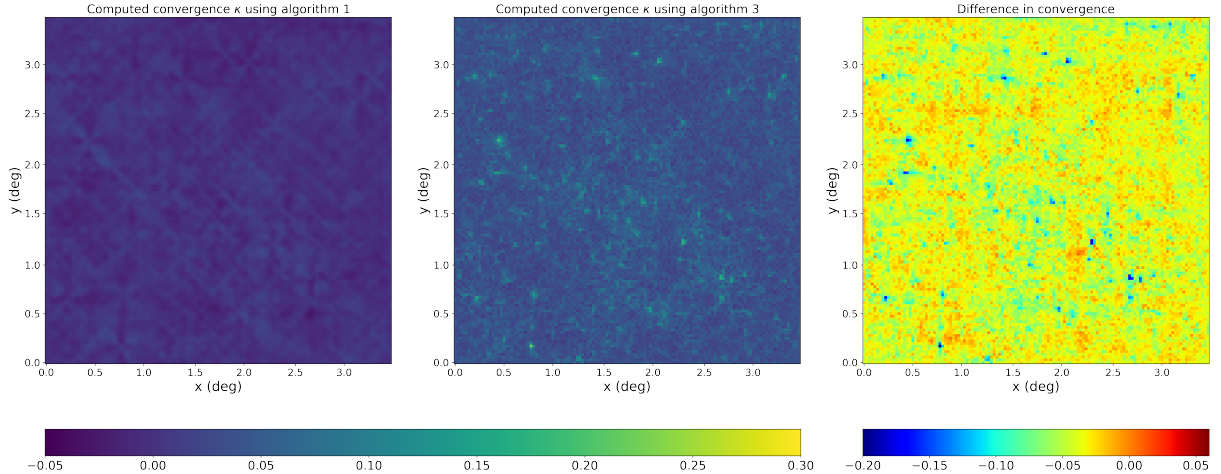
Figure 34: Comparison between the convergence fields computed with algorithm 1 assuming Neumann boundary conditions on all four boundary parts and algorithm 3.
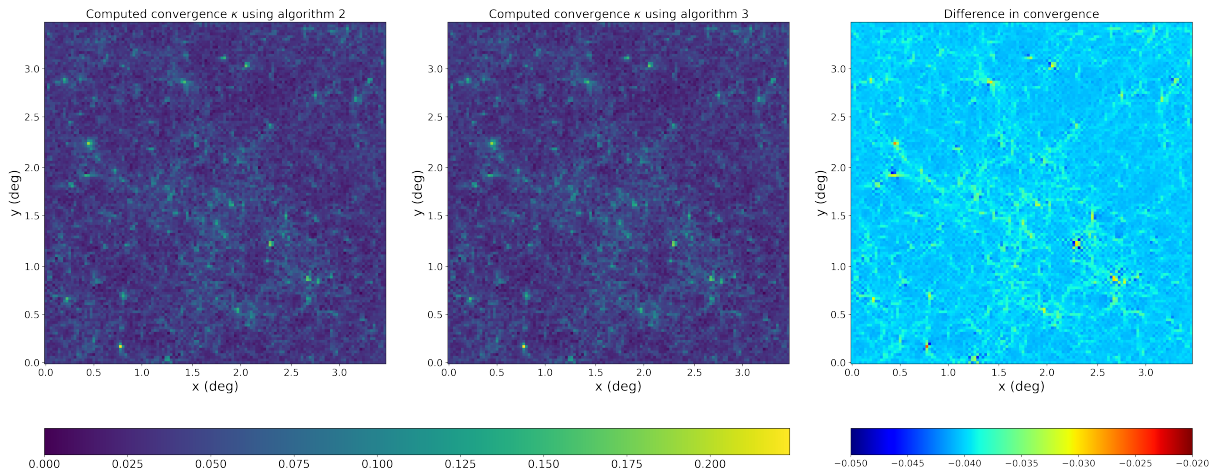

Figure 35: Comparison between the convergence fields computed with algorithm 2 and 3.

As can be seen, the deviations between the convergence calculated with algorithm 1 and algorithm 2 are broadly of the order $O(10^{-3})$ to $O(10^{-2})$. In comparison, the differences between the result obtained with algorithm 1 and 3 are much larger and almost uniformly of the order $O(10^{-2})$. Furthermore, in regions with large κ-values, deviations of the order $O(10^{-1})$ are partially obtained. The plots also show well that the convergence fields calculated by the algorithms 2 and 3 provide much finer structures. At the same resolution, the KS 93 algorithm or its non-linear variant can calculate the convergence much more accurately and resolve finer structures than algorithm 1. The advantages of algorithm 1 mentioned in chapter 3.1.5 only come into effect at a high resolution orders, which, however, require a lot of computing time!

5 Conclusion and Outlook

In this thesis we followed the idea to combine weak gravitational lensing with quasi-conformal geometry, mainly to derive a new inversion algorithm for weak lensing measurements. Therefore, we considered the lens mapping in the flat-sky approximation as quasi-conformal mapping with Beltrami coefficient given by the negative of the reduced shear.

After reproducing some advantages of translating the weak lensing formalism into a complex one, we obtained the first result of this thesis: Using analytical properties of quasi-conformal mappings we were able to derive some analytical statements about weak lensing quantities, e.g. a lower bound for the convergence and an upper bound for the absolute value of the complex shear. Both bounds depend only on the two observable quantities magnification and maximum reduced shear.

Considering the lens mapping as a quasi-conformal mapping gave us the second result: A new inversion algorithm in the flat-sky limit to reconstruct the deflection field and thus shear und convergence out of the reduced shear field by solving the Beltrami equation. Therefore, we reduced the Beltrami equation into two elliptic PDEs, one for the real and one for the imaginary part of the lens mapping. Each PDE was then solved using a finite element approach. To ensure well-posedness, we had to assume appropriate boundary conditions. We tested our implementation for the Schwarzschild and singular isothermal lens for both Dirichlet and Neumann boundary conditions and applied it afterwards to actual data. Since for actual data we do not know how the deflection field behaves on the boundary we assumed first approximated Dirichlet and afterwards Neumann boundary conditions. Depending on what assumptions can be made about convergence, shear and the deflection field, some boundary conditions are more suitable than others. As we have seen, for the actual data considered in chapter 4 approximated Neumann boudary conditions provided a much better approximation for convergence and shear than Dirichlet boundary conditions.

Finally, we investigated whether our algorithm for the planar case can be generalized to areas of the celestial sphere for which the flat-sky approximation provides no longer suitable results. Unfortunately, for general areas the atlas construced by means of the flat-sky approximation is not conformal and admits no well-defined Beltrami differential on it, which is constructed out of the reduced shear. Only in the case of a narrow strip we can model the area as Riemann surface with in first order well-defined Beltrami differential on it. In this case, the lens mapping can be considered as a q.c. mapping on the strip. Using methods from computational quasi-conformal geometry, it is also possible to compute it numerically. The concrete implementation of the proposed algorithm for narrow strips will be the topic of future work.

As this is the first work considering the intersection between weak gravitational lensing and quasi-conformal geometry, there are many aspects which can be investigated in future work. Since many of these possible topics have already been raised in the course of this paper, we will conclude here by addressing those not mentioned yet: The first idea is to go the opposite way, which we followed in this paper. Namely to apply concepts from weak lensing to (computational) quasi-conformal geometry. For example, is it possible to construct an algorithm for q.c. mappings using the KS 93 algorithm and its extensions, e.g. if the Beltrami coefficient is error-prone? Furthermore, one can try to use different algorithms for solving the Beltrami equation in algorithm 1. One of the main demerits of our implementation was the exponentially increasing computing time with increasing refinement level. Other algorithms from computational quasi-conformal geometry may not suffer from such behavior. In addition, our proposed algorithm depends strongly on the boundary conditions assumed. Thus, a systematic investigation of the influence of the used boundary conditions on the result of the calculation would be helpful. For instance, one could examine whether for certain domains fewer boundary conditions are sufficient to recieve an unique solution of the lens mapping. Lastly, it is also an open question whether one can develop an algorithm for general curved fields as a superposition of several narrow strips.

References

Lars Ahlfors. Conformality with respect to riemannian matrices. *Ann. Acad. Sci. Fenn. Ser.*, 206:1–22, 1955.

Lars Ahlfors. *Lectures on Quasiconformal Mappings -*. American Mathematical Soc., Heidelberg, 2006. ISBN 978-0-821-83644-6.

K. Astala, T. Iwaniec, and G. Martin. *Elliptic Partial Differential Equations and Quasiconformal Mappings in the Plane (PMS-48)*. Princeton University Press, 2009. URL http://www.jstor.org/stable/j.ctt7sjhd.

M. Bartelmann and P. Schneider. Weak gravitational lensing. 340(4-5):291–472, January 2001. doi: 10.1016/S0370-1573(00)00082-X.

M. Bartelmann, R. Narayan, S. Seitz, and P. Schneider. Maximum likelihood cluster reconstruction. *The Astrophysical Journal*, 464(2):L115–L118, jun 1996. doi: 10.1086/310114. URL https://doi.org/10.1086%2F310114.

Matthias Bartelmann. Gravitational lensing. *Classical and Quantum Gravity*, 27(23):233001, nov 2010. doi: 10.1088/0264-9381/27/23/233001. URL https://doi.org/10.1088%2F0264-9381%2F27%2F23%2F233001.

Marc Bourdon and Hervé Pajot. *Quasi-Conformal Geometry and Hyperbolic Geometry*, pages 1–17. Springer Berlin Heidelberg, Berlin, Heidelberg, 2002. ISBN 978-3-662-04743-9. doi: 10.1007/978-3-662-04743-9_1. URL https://doi.org/10.1007/978-3-662-04743-9_1.

M. Bradač, D. Clowe, and A. Gonzalez et al. Strong and Weak Lensing United. III. Measuring the Mass Distribution of the Merging Galaxy Cluster 1ES 0657 558. *The Astrophysical Journal*, 652(2): 937–947, December 2006. ISSN 1538-4357. URL http://dx.doi.org/10.1086/508601.

Dietrich Braess. *Finite Elemente - Theorie, schnelle Löser und Anwendungen in der Elastizitätstheorie*. Springer-Verlag, Berlin Heidelberg New York, 2013. ISBN 978-3-662-07234-9.

T. J. Broadhurst, A. N. Taylor, and J. A. Peacock. Mapping Cluster Mass Distributions via Gravitational Lensing of Background Galaxies. 438:49, January 1995. doi: 10.1086/175053.

P. G. Castro, A. F. Heavens, and T. D. Kitching. Weak lensing analysis in three dimensions. *Physical Review D*, 72(2), jul 2005. doi: 10.1103/physrevd.72.023516. URL https://doi.org/10.1103%2Fphysrevd.72.023516.

Jean Cea. Approximation variationnelle des problèmes aux limites. *Annales de l'Institut Fourier*, 14(2): 345–444, 1964. doi: 10.5802/aif.181. URL http://www.numdam.org/articles/10.5802/aif.181/.

CFHTLenS Collaboration, L. Van Waerbeke, J. Benjamin, and T. Erben et al. Cfhtlens: mapping the large-scale structure with gravitational lensing. *Mon Not R Astron Soc*, 433(4):3373–3388, August 2013. ISSN 0035-8711. URL https://doi.org/10.1093/mnras/stt971.

C. Chang, V. Vikram, and B. Jain et al. Wide-field lensing mass maps from dark energy survey science verification data. *Phys. Rev. Lett.*, 115(5):051301, July 2015. URL https://link.aps.org/doi/10.1103/PhysRevLett.115.051301.

Shing-Shen Chern. An elementary proof of the existence of isothermal parameters on a surface. *Proceedings of the American Mathematical Society*, 6(5):771–782, 1955. ISSN 00029939, 10886826. URL http://www.jstor.org/stable/2032933.

Lam Ka Chun and Lok Ming Lui. Landmark and intensity based registration with large deformations via quasi-conformal maps, 2013. URL https://arxiv.org/abs/1310.1710.

Philippe G. Ciarlet. *The Finite Element Method for Elliptic Problems -*. SIAM, Philadelphia, 2002. ISBN 978-0-898-71514-9.

R. Crittenden, P. Natarajan, U.-L. Pen, and T. Theuns. Discriminating weak lensing from intrinsic spin correlations using the curl-gradient decomposition. *The Astrophysical Journal*, 568(1):20–27, March 2002. ISSN 1538-4357. URL http://dx.doi.org/10.1086/338838.

Shaozhong Deng. Quadrature formulas in two dimensions. 2017.

DES Collaboration, C. Chang, A. Pujol, and B. Mawdsley. Dark energy survey year 1 results: curved-sky weak lensing mass map. *Mon. Not. R. Astron. Soc.*, 475(3):3165–3190, April 2018.

Otto Forster. *Lectures on Riemann Surfaces -*. Springer Science & Business Media, Berlin Heidelberg, 2012. ISBN 978-1-461-25961-9.

David Gilbarg and Neil S. Trudinger. *Elliptic Partial Differential Equations of Second Order -*. Springer, Berlin, Heidelberg, 2015. ISBN 978-3-642-61798-0.

Seddik Gmira. Existence theorem on quasiconformal mappings. 2016. URL https://hal.archives-ouvertes.fr/hal-01285906.

Herbert Grötzsch. Über die Verzerrung bei schlichten nichtkonformen Abbildungen und über eine damit zusammenhängende Erweiterung des Picardschen Satzes. *Rec. Math.*, 80:503–507, 1928.

Xianfeng David Gu and Shing-Tung Yau. *Computational Conformal Geometry -*. International Press, Boston, 2008. ISBN 978-1-571-46171-1.

Bernhard Hofmann-Wellenhof. Die konforme Abbildung oder: Muß Komplexes komplex sein? *VGI – Österreichische Zeitschrift für Vermessung und Geoinformation*, 83(1–2):55–62, 1995. URL https://www.ovg.at/de/vgi/files/pdf/4620/.

John H. Hubbard. *Teichmüller Theory and Applications to Geometry, Topology, and Dynamics*, volume 2 of *Surface Homeomorphisms and Rational Functions*. Matrix Editions, April 2016. URL https://hal.archives-ouvertes.fr/hal-01297628.

Jürgen Jost. *Compact Riemann Surfaces - An Introduction to Contemporary Mathematics*. Springer Science & Business Media, Berlin Heidelberg, 2006. ISBN 978-3-540-33067-7.

N. Kaiser, G. Squires, and T. Broadhurst. A method for weak lensing observations. *The Astrophysical Journal*, 449:460, aug 1995. doi: 10.1086/176071. URL https://doi.org/10.1086%2F176071.

Nick Kaiser. Nonlinear cluster lens reconstruction. *The Astrophysical Journal*, 439:L1, jan 1995. doi: 10.1086/187730. URL https://doi.org/10.1086%2F187730.

Hendrik Kasten. Funktionentherie 2 Vorlesungsskript, 2016. URL https://www.mathi.uni-heidelberg.de/~kasten/files/Skripte/ws16funktheo2.pdf.

Eiichiro Komatsu. Lecture 2 in Cargese, 2017. URL https://wwwmpa.mpa-garching.mpg.de/~komatsu/presentation/cargese2017_lecture2.pdf.

Arthur Korn. *Zwei Anwendungen der Methode der sukzessiven Annäherungen*, pages 215–229. Springer Berlin Heidelberg, Berlin, Heidelberg, 1914. ISBN 978-3-642-50735-9. doi: 10.1007/978-3-642-50735-9_16. URL https://doi.org/10.1007/978-3-642-50735-9_16.

Michail Lawrentjew. Sur une classe de representations continues. *Rec. Math.*, 48:407–423, 1935.

Olli Lehto. *Quasiconformal Mappings in the Plane - By O. Lehto and K.I. Virtanen. Translated from the German by K.W. Lucas*. Springer, Berlin, Heidelberg, 1973.

Leon Lichtenstein. Zur Theorie der konformen Abbildung: Konforme Abbildung nichtanalytischer, singularitätenfreier Flächenstücke auf ebene Gebiete. *Bull. Acad. Sci. Cracovie*, January 1916.

L. M. Lui, X. Gu, and S.-T. Yau. Convergence of an iterative algorithm for Teichmüller maps via generalized harmonic maps, 2013a. URL https://arxiv.org/abs/1307.2679.

L. M. Lui, K. C. Lam, T. W. Wong, and X. Gu. Texture map and video compression using Beltrami representation. *SIAM Journal on Imaging Sciences*, 6(4):1880–1902, 2013b. doi: 10.1137/120866129. URL https://doi.org/10.1137/120866129.

Massimo Meneghetti. *Introduction to Gravitational Lensing - With Python Examples*. Springer Nature, Singapore, 2021. ISBN 978-3-030-73582-1.

J. Merten, M. Cacciato, M. Meneghetti, C. Mignone, and M. Bartelmann. Combining weak and strong cluster lensing: applications to simulations and MS 2137. *A&A*, 500(2):681–691, 2009. URL https://doi.org/10.1051/0004-6361/200810372.

Charles Morrey. On the solutions of quasi-linear elliptic differential equations. *Trans. Amer. Math. Soc.*, 43:126–166, 1938.

Karel Rektorys. *Variational Methods in Mathematics, Science and Engineering -*. Springer Science & Business Media, Berlin Heidelberg, 2012. ISBN 978-9-401-16450-4.

Carolin Seitz and Peter Schneider. Steps towards nonlinear cluster inversion through gravitational distortions: Iii. including a redshift distribution of the sources, 1996. URL https://arxiv.org/abs/astro-ph/9601079.

Stella Seitz and Peter Schneider. Cluster lens reconstruction using only observed local data – an improved finite-field inversion technique, 1995. URL https://arxiv.org/abs/astro-ph/9503096.

Norbert Straumann. Complex formulation of lensing theory and applications, 1997. URL https://arxiv.org/abs/astro-ph/9703103.

Andrejs Treibergs. Geometry of surfaces, 2010. URL https://www.math.utah.edu/~treiberg/ERD_1-22-2010.pdf.

K. Umetsu, M. Tada, and T. Futamase. Cluster mass reconstruction by a weak shear field. *Progress of Theoretical Physics Supplement*, 133:53–84, 1999. doi: 10.1143/ptps.133.53. URL https://doi.org/10.1143%2Fptps.133.53.

Keiichi Umetsu. Cluster–galaxy weak lensing. *The Astronomy and Astrophysics Review*, 28 (1), nov 2020. doi: 10.1007/s00159-020-00129-w. URL https://doi.org/10.1007%2Fs00159-020-00129-w.

Keiichi Umetsu and Toshifumi Futamase. Detection of dark matter concentrations in the field of cl 1604+4304 from weak lensing analysis. *The Astrophysical Journal*, 539(1):L5–L8, August 2000. ISSN 0004-637X. URL http://dx.doi.org/10.1086/312833.

V. Vikram, C. Chang, and B. Jain et al. Wide-field lensing mass maps from dark energy survey science verification data: Methodology and detailed analysis. *Phys. Rev. D*, 92(2):022006, July 2015. URL https://link.aps.org/doi/10.1103/PhysRevD.92.022006.

C. Wallis, M. Price, and J. McEwen et al. Mapping dark matter on the celestial sphere with weak gravitational lensing. *Monthly Notices of the Royal Astronomical Society*, 509(3):4480–4497, nov 2021. doi: 10.1093/mnras/stab3235. URL https://doi.org/10.1093%2Fmnras%2Fstab3235.

Saeed Zakeri. Some applications of quasiconformal mappings. URL https://qcpages.qc.cuny.edu/~zakeri/notes/qc.pdf.

W. Zeng, L. M. Lui, and F. Luo et al. Computing quasiconformal maps using an auxiliary metric and discrete curvature flow. *Numerische Mathematik*, 121(4):671–703, August 2012. ISSN 0945-3245. URL https://doi.org/10.1007/s00211-012-0446-z.

Erklärung

Ich versichere, dass ich diese Arbeit selbstständig verfasst und keine anderen als die angegebenen Quellen und Hilfsmittel benutzt habe.

Heidelberg, den 08. Juni 2022